

A Thesis

Entitled

Mitigating the Biomechanical Complications Following Pedicle Subtraction Osteotomy:

A Finite Element Analysis

by

Ardalan Seyed Vosoughi

Submitted to the Graduate Faculty as partial fulfillment of the requirements for the

Master of Science Degree in

Bioengineering

---

Dr. Vijay Goel, Committee Chair

---

Dr. Anand Agarwal, Committee Member

---

Dr. Ronald Fournier, Committee Member

---

Dr. Amanda Bryant-Friedrich, Dean College of  
Graduate Studies

The University of Toledo

August 2017

Copyright 2017, Ardalan Seyed Vosoughi

This document is copyrighted material. Under copyright law, no parts of this document may be reproduced without the expressed permission of the author.

An Abstract of  
Mitigating the Biomechanical Complications Following Pedicle Subtraction Osteotomy:

A Finite Element Analysis

by

Ardalan Seyed Vosoughi

Submitted to the Graduate Faculty as partial fulfillment of the requirements for the  
Master of Science Degree in Bioengineering

The University of Toledo

August 2017

Following advances in spinal instrumentation and techniques, management of the sagittal malalignment has gone through a significant evolution. In this regard, spinal osteotomy surgeries have evolved to achieve balance, inhibit the deformity progression, and mitigate pain in the patients. Among the realignment techniques, pedicle subtraction osteotomy (PSO) has become a common method to correct adult spinal deformity. Despite multiple benefits of the PSO in addressing the sagittal spinal imbalance, it is a technically demanding procedure. A major complication associated with PSO is rod breakage, and the rate of postoperative complication has been reported to be as high as 31.6%. Despite various efforts to study PSO in recent years, the biomechanical reasons for the high rate of rod failure remain unclear.

In this study, the finite element modeling of PSO is used to assess the biomechanical effects of the lumbar disc degeneration and various instrumentation techniques including the use of multi rods, interbody spacers, and cross connectors on the instrumentation. Multi-rod constructs included medially, laterally, and posteriorly affixed

satellite rod configurations and the short-rod technique. Biomechanical studies were conducted to evaluate various parameters such as range of motion, maximum von Mises stress on the rods, and the force acting on the osteotomy site.

The results of the current study showed that larger discs adjacent to the PSO lead to a greater motion and instability and superior maximum von Mises stress on the rods which occurred at the PSO region. In multi-rod constructs, adding satellite rods in various loading directions decreases the maximum von Mises stress at the PSO region which results in lower risk of rod fracture at this site. Furthermore, it was observed that in multi-rod constructs connected with side-by-side connectors the greatest stress concentration occurs adjacent to the connectors. At the PSO region by adding satellite rods medially and laterally the maximum von Mises stress occurs on the medial rods. These observations indicate that at the PSO region in the medially affixed constructs there is a greater risk of rod failure in satellite rods while in the laterally affixed constructs it is on the primary rods. These findings exhibit a significant benefit in supplementing the PSO setting with the medially affixed satellite rods over the laterally affixed satellite rods that in the case of rod failure the surgeon can easily replace the satellite rods instead of the primary rods. The findings demonstrated that placing the satellite rods posteriorly allows for more stress reduction on the instrumentations. The current FE study also signified that except short-rod technique all other multi-rod constructs decrease the magnitude of the load acting on the osteotomy region which may cause in delayed union or non-union of the PSO site.

Interbody spacer placement in the PSO setting decreases the maximum von Mises stress on the rods while it increases the stability and the force acting on the osteotomy region. Finally, adding cross-connectors to a PSO acute setting has a slight stabilizing

potential in axial rotation motion, and the greater number of cross-links may increase the rate of rod fracture.

I would like to dedicate this research to my parents, Farhad Seyed Vosoughi and Erika Ketabchi, my sister, Arghavan Seyed Vosoughi, and all of my friends, without whom none of my success would be possible.

## **Acknowledgments**

First, I would like to express my sincere gratitude to my advisor, Prof. Vijay Goel, who has been a wonderful teacher, guide, and philosopher during the course of this research. Second, I would like to thank Dr. Anand Agarwal for his continued effort to further my professional development. Without their encouragement and guidance this research would have never been possible.

I would also like to thank the University of Toledo faculty and staff, bioengineering department faculty and staff, ECORE faculty and staff, Spinal Balance staff, Dr. Joseph Zavatsky, Dr. Aakash Agarwal, Dr. Ali Kiapour, David Dick, and the Center for Disruptive Musculoskeletal Innovations ([nsfcdmi.org](http://nsfcdmi.org)).

Lastly, I take the opportunity to express my profound gratitude to my parents, sister, and my friends for their unconditional moral support and belief in me.

# Table of Contents

|  |          |
|--|----------|
| Abstract.....                                    | iii      |
| Acknowledgments.....                             | vi       |
| Table of Contents.....                           | vii      |
| List of Tables.....                              | xiv      |
| List of Figures.....                             | xiv      |
| List of Abbreviations.....                       | xxi      |
| <b>1 Introduction.....</b>                       | <b>1</b> |
| 1.1 Rationale for Research.....                  | 1        |
| <b>2 Biomechanical Anatomy of the Spine.....</b> | <b>6</b> |
| 2.1 Overview.....                                | 6        |
| 2.2 Introduction.....                            | 6        |
| 2.3 Cervical Spine.....                          | 8        |
| 2.4 Thoracic Spine.....                          | 8        |
| 2.5 Lumbar Region.....                           | 9        |
| 2.6 Sacral and Coccygeal Regions.....            | 10       |
| 2.7 Facet Joints.....                            | 11       |
| 2.8 Spinal Ligaments.....                        | 13       |
| 2.8.1 Anterior Longitudinal Ligament (ALL).....  | 15       |

|          |   |           |
|----------|---|-----------|
| 2.8.2    | Posterior Longitudinal Ligament (PLL)               | 15        |
| 2.8.3    | Ligamentum Flavum (LF)                              | 15        |
| 2.8.4    | Supraspinous Ligament (SSL)                         | 16        |
| 2.8.5    | Interspinous Ligament (ISL)                         | 16        |
| 2.8.6    | Intertransverse Ligament (ITL)                      | 16        |
| 2.8.7    | Facet Capsular Ligament                             | 17        |
| 2.9      | Intervertebral Disc (IVD)                           | 17        |
| 2.9.1    | Annulus Fibrosus (AF)                               | 18        |
| 2.9.2    | Nucleus Pulposus (NP)                               | 19        |
| 2.9.3    | Cartilaginous End Plate (CEP)                       | 19        |
| 2.10     | Disc Degeneration                                   | 20        |
| <b>3</b> | <b>Literature Review</b>                            | <b>24</b> |
| 3.1      | Overview  | 24        |
| 3.2      | Introduction  | 24        |
| 3.3      | Nomenclature  | 25        |
| 3.4      | Normal Sagittal Balance                             | 28        |
| 3.5      | Sagittal Imbalance Etiology                         | 30        |
| 3.6      | Spinal Osteotomies                                  | 31        |
| 3.6.1    | Smith-Peterson Osteotomy (SPO)                      | 32        |
| 3.6.2    | Pedicle Subtraction Osteotomy (PSO)                 | 33        |
| 3.6.3    | Bone-disc-bone Osteotomy (BDBO)                     | 34        |
| 3.6.4    | Vertebral Column Resection (VCR)                    | 35        |
| 3.7      | Minimally Invasive Surgery (MIS) Approaches for ASD | 36        |

|          |   |           |
|----------|---|-----------|
| 3.8      | Osteotomies and Complications.....                              | 36        |
| 3.9      | Instrumentation Failure Following PSO .....                     | 38        |
| 3.9.1    | Clinical Studies.....   | 39        |
| 3.9.2    | In-Silico and In-Vitro Studies.....                             | 41        |
| <b>4</b> | <b>Material and Methods.....</b>                                | <b>44</b> |
| 4.1      | Overview .....  | 44        |
| 4.2      | Finite Element Model Development .....                          | 44        |
| 4.3      | PSO Finite Element Model Development.....                       | 50        |
| 4.4      | Disc Degenerated PSO Finite Element Models Development.....     | 52        |
| 4.5      | Models Instrumentation.....                                     | 55        |
| 4.6      | FE Modeling of Alternative Instrumentation Techniques.....      | 57        |
| 4.6.1    | Multi-Rod FE Constructs.....                                    | 57        |
| 4.6.2    | Interbody Spacer FE Models .....                                | 64        |
| 4.6.3    | Cross-Connector FE Models .....                                 | 65        |
| 4.7      | Loading and Boundary Conditions .....                           | 67        |
| 4.8      | Models Validation .....   | 67        |
| 4.9      | Data Analysis .....   | 68        |
| <b>5</b> | <b>Results.....</b>   | <b>70</b> |
| 5.1      | Introduction .....  | 70        |
| 5.2      | Validation Results .....  | 70        |
| 5.3      | Results of IVD Geometry Effects on the Rods Following PSO ..... | 75        |
| 5.3.1    | Range of Motion Results .....                                   | 75        |
| 5.3.2    | Von Mises Stress Results .....                                  | 78        |

|          |  |            |
|----------|--|------------|
| 5.3.3    | Force Results .....                                  | 79         |
| 5.4      | Results of Multi-Rod FE Constructs .....             | 79         |
| 5.4.1    | Range of Motion Results .....                        | 79         |
| 5.4.2    | Von Mises Stress Results .....                       | 83         |
| 5.4.3    | Force Results .....                                  | 97         |
| 5.5      | Results of the FE Interbody Spacer Constructs.....   | 98         |
| 5.5.1    | Range of Motion Results .....                        | 98         |
| 5.5.2    | Von Mises Stress Results .....                       | 99         |
| 5.5.3    | Force Results .....                                  | 100        |
| 5.6      | Results of the FE Cross-Connector Constructs .....   | 101        |
| 5.6.1    | Range of Motion Results .....                        | 101        |
| 5.6.2    | Von Mises Stress Results .....                       | 102        |
| 5.6.3    | Force Results .....                                  | 104        |
| <b>6</b> | <b>Discussion .....</b>                              | <b>105</b> |
| 6.1      | Overview .....                                       | 105        |
| 6.2      | FE Models Validation .....                           | 105        |
| 6.3      | IVD Geometry Effects on the Rods Following PSO.....  | 107        |
| 6.4      | FE Analysis of the Multi-rod Constructs .....        | 108        |
| 6.5      | FE Analysis of the Interbody Spacer Constructs ..... | 113        |
| 6.6      | FE Analysis of the Cross-Connector Constructs.....   | 114        |
| 6.7      | Limitations and Future Work .....                    | 116        |
| 6.8      | Conclusions .....                                    | 118        |
| <b>7</b> | <b>References .....</b>                              | <b>120</b> |

|          |                       |            |
|----------|-----------------------|------------|
| <b>8</b> | <b>Appendix .....</b> | <b>135</b> |
|----------|-----------------------|------------|

## List of Tables

|  |    |
|--|----|
| Table 2.1 Summary of in vitro ROM studies on the disc degeneration [120] .....   | 22 |
| Table 4.1 Material properties of bony structure and joints of the spine and pelvis.....  | 45 |
| Table 4.2 Material properties of the spine and pelvis ligaments. ....  | 46 |
| Table 4.3 Height measurements for healthy, mildly degenerated, moderately degenerated, and severely degenerated intervertebral discs of the lumbar segment.....                      | 53 |
| Table 4.4 Material properties of the healthy and degenerated intervertebral discs. ....  | 54 |
| Table 5.1 Maximum von Mises stress values and locations recorded on the rods in different motions and different grades of IVD degeneration.....                                      | 78 |
| Table 5.2 Maximum von Mises stress values and locations recorded on the rods at the PSO region during different loading cases in the two-rod and short-rod constructs. ....          | 85 |
| Table 5.3 Maximum von Mises stress values and locations recorded on the rods at the PSO region in different motions and different medially affixed satellite rod constructs.....     | 85 |
| Table 5.4 Maximum von Mises stress values and locations recorded on the rods at the PSO region in different motions and different laterally affixed satellite rod constructs.....    | 86 |
| Table 5.5 Maximum von Mises stress values and locations recorded on the rods at the PSO region in different motions and different posteriorly affixed satellite rod constructs. .... | 86 |
| Table 5.6 Maximum von Mises stress values and locations recorded on the rods in different motions and different medially affixed satellite rod constructs.....                       | 89 |

|   |     |
|---|-----|
| Table 5.7 Maximum von Mises stress values and locations recorded on the rods in different motions and different laterally affixed satellite rod constructs.....                         | 92  |
| Table 5.8 Maximum von Mises stress values and locations recorded on the rods in different motions and different posteriorly affixed satellite rod constructs. ....                      | 94  |
| Table 5.9 Comparison of the Maximum von Mises stress values and locations recorded on the rods during different loading cases between the 2-rod and short-rod constructs.....           | 96  |
| Table 5.10 Magnitude of the load acting on the PSO region in different constructs and after follower load application. ....   | 98  |
| Table 5.11 Maximum von Mises stress values and locations recorded on the rods in different motions and different interbody spacer constructs.....                                       | 100 |
| Table 5.12 Maximum von Mises stress values and locations recorded on the rods in different motions and different locations of the cross-connector. ....                                 | 103 |
| Table A.1 Maximum von Mises stress values and locations recorded on the rods in different motions after adding interbody spacers and bone grafts at the adjacent levels to the PSO..... | 136 |

## List of Figures

|   |    |
|---|----|
| Figure 2-1 Lateral and posterior views of a normal spine showing different regions of cervical, thoracic, lumbar, sacral, and coccygeal regions [41].   | 11 |
| Figure 2-2 Lateral and posterior views of a functional spinal unit showing facet joint and intervertebral discs. (Source: <a href="http://img.medscapestatic.com/pi/meds/ckb/59/12059.jpg">http://img.medscapestatic.com/pi/meds/ckb/59/12059.jpg</a> ) | 13 |
| Figure 2-3 Anterolateral representation of a lumbar functional spinal unit demonstrating the spinal ligaments. (Source: <a href="http://img.medscapestatic.com/pi/meds/ckb/60/12060.jpg">http://img.medscapestatic.com/pi/meds/ckb/60/12060.jpg</a> )   | 14 |
| Figure 2-4 Posterolateral view of a intervertebral disc showing annulus fibrosus, nucleus pulposus, and vertebral endplate [32].  | 18 |
| Figure 2-5 Lateral view of a spine segment showing healthy and degenerated discs. (Source: <a href="https://healthyspines.org/wp-content/uploads/2015/08/DDD.jpg">https://healthyspines.org/wp-content/uploads/2015/08/DDD.jpg</a> )                    | 21 |
| Figure 3-1 A demonstration of pelvic parameters including Pelvic tilt, sacral slope, and pelvic incidence. (Source: <a href="http://www.eneurosurgery.com/wpimages/wp09866018.png">http://www.eneurosurgery.com/wpimages/wp09866018.png</a> )           | 26 |
| Figure 3-2 Sagittal spinal radiographic parameters. In this figure thoracic kyphosis (TK), lumbar lordosis (LL), T1 and T9 spinopelvic inclination angles and sagittal vertical axis (SVA) were demonstrated [129].                                     | 28 |

Figure 3-3 Cone of balance or economy. Deviation from the zones shown in the figure results in energy expenditure and muscular effort [129]. ..... 29

Figure 3-4 Different types of posterior spinal osteotomies. Smith-Peterson/PCO osteotomy (Left). Pedicle subtraction osteotomy (Middle). Vertebral column resection (Right). (Source: <http://columbiaspine.org/wp-content/uploads/2016/01/Deformity-correction-copy-1.jpg>) ..... 32

Figure 4-1 Lateral (Left) and posterior (Right) views of the spinopelvic model used for this study..... 50

Figure 4-2 Lateral (Left) and Posterior (Right) views of the spinopelvic pelvic model following 30° of PSO at the L3 level. At the PSO level, posterior elements including posterior arch, posterior ligaments, transverse ligaments, interspinous ligaments, and supraspinous ligaments were removed. .... 51

Figure 4-3 Lateral views of the developed spinopelvic FE models integrated with 30° of PSO at the L3 level accompanied with various lumbar intervertebral disc degeneration grades: (a) Healthy discs; (b) Mildly degenerated; (c) Moderately degenerated; (d) Severely degenerated. For the sake of intervertebral discs visualization, the ilium bones were not shown in this figure..... 53

Figure 4-4 Lateral and posterior views of the instrumented spinopelvic healthy discs model treated with PSO at the L3 level. For the sake of instrumentation clarity, the spinopelvic geometry was made transparent. The instrumentations used in the model were shown in dark color. .... 56

Figure 4-5 Posterior view of the instrumented PSO model using medially affixed 3-rod construct (Short). Using side-by-side cross connector, the secondary rod was connected to the right principal rod above L2 and below L4 pedicle screw levels. .... 58

Figure 4-6 Posterior view of the instrumented PSO model using medially affixed 3-rod construct (Long). Using side-by-side cross connector, the secondary rod was connected to the right principal rod above L1 and below L5 pedicle screw levels. .... 58

Figure 4-7 Posterior view of the instrumented PSO model using medially affixed 4-rod construct (Short). Using side-by-side cross connectors, the secondary rods were connected to the principal rods above L2 and below L4 pedicle screw levels. .... 59

Figure 4-8 Posterior view of the instrumented PSO model using medially affixed 4-rod construct (Long). Using side-by-side cross connectors, the secondary rods were connected to the principal rods above L1 and below L5 pedicle screw levels. .... 59

Figure 4-9 Posterior view of the instrumented PSO model using laterally affixed 3-rod construct (Short). Using side-by-side cross connector, the secondary rod was connected to the right principal rod above L2 and below L4 pedicle screw levels. .... 60

Figure 4-10 Posterior view of the instrumented PSO model using laterally affixed 3-rod construct (Long). Using side-by-side cross connector, the secondary rod was connected to the right principal rod above L1 and below L5 pedicle screw levels. .... 61

Figure 4-11 Posterior view of the instrumented PSO model using laterally affixed 4-rod construct (Short). Using side-by-side cross connectors, the secondary rods were connected to the principal rods above L2 and below L4 pedicle screw levels. .... 61

Figure 4-12 Posterior view of the instrumented PSO model using laterally affixed 4-rod construct (Long). Using side-by-side cross connectors, the secondary rods were connected to the principal rods above L1 and below L5 pedicle screw levels. .... 62

Figure 4-13 Posterior view of the instrumented PSO model using “head-to-head” dual rod technique. The secondary rods were connected to the principal rods at L1 and L5 pedicle screw levels. .... 63

Figure 4-14 Posterior view of the instrumented PSO model using “head-to-head” dual rod technique. The secondary rods were connected to the principal rods at L1, L5, and S1 screw levels. .... 63

Figure 4-15 Lateral (right) and posterior (left) views of the instrumented PSO model using “short rod” technique. In this technique, the two primary rods were not connected to the pedicle screws immediately adjacent to the PSO, whereas two additional short rods were attached to the pedicle screws adjacent to the PSO. For the sake of instrumentation visualization, in the lateral view, the ilium bones were not shown. .... 64

Figure 4-16 Lateral view of the instrumented spinopelvic model supplemented with interbody spacers adjacent to the PSO level (L3). On the left side, a top view of the meshed interbody spacer used in the model was demonstrated. For the sake of intervertebral discs visualization, the ilium bones were not shown in this figure. .... 65

Figure 4-17 A posterior representation of four different configurations with the cross connector. (a) Cross connector located above the PSO level. (b) cross-connector located below the PSO level. (c) Cross connectors located above and below the PSO level. (d) Cross connector located at the PSO level. .... 66

|   |    |
|---|----|
| Figure 5-1 L1-S1 global ROM for the intact and PSO (at L3) FE models during during different loading cases. ....  | 71 |
| Figure 5-2 L2-L4 range of motion comparison of the instrumented FE models (before and after PSO performance) with experimental data at 7.5Nm.....   | 72 |
| Figure 5-3 Comparison of ROMs of developed degenerated L1-L2 motion segments models to results from Mimura et al. study in flexion/extension, lateral bending, and axial rotation under 10 Nm moments. .... | 73 |
| Figure 5-4 Comparison of ROMs of developed degenerated L4-L5 motion segments models to results from Mimura et al. study in flexion/extension, lateral bending, and axial rotation under 10 Nm moments. .... | 74 |
| Figure 5-5 Comparison of ROMs of developed degenerated L5-S1 motion segments models to results from Mimura et al. study in flexion/extension, lateral bending, and axial rotation under 10 Nm moments. .... | 75 |
| Figure 5-6 Instrumented L2-L4 Global ROM for different loading cases and different grades of disc degeneration.....   | 76 |
| Figure 5-7 Instrumented T10-S1 Global ROM for different loading cases and different grades of disc degeneration.....  | 77 |
| Figure 5-8 Comparison of the instrumented T10-S1 global ROM for different loading cases and different medially affixed multi-rod constructs. ....   | 80 |
| Figure 5-9 Comparison of the instrumented T10-S1 global ROM for different loading cases and different laterally affixed multi-rod constructs. ....  | 81 |
| Figure 5-10 Comparison of the instrumented T10-S1 global ROM for different loading cases and different posteriorly affixed multi-rod constructs.....  | 82 |

Figure 5-11 Comparison of the instrumented T10-S1 global ROM for different loading cases between the 2-rod and short-rod constructs..... 83

Figure 5-12 The von Mises stress contour on the instrumentation during flexion in 4-rod medially affixed short satellite rod (Left) and 4-rod medially affixed long satellite rod (Right) constructs. The red oval shapes show the location of the maximum von Mises stress on the rods..... 89

Figure 5-13 The von Mises stress contour on the instrumentation during flexion in 4-rod laterally affixed short satellite rod (Left) and 4-rod laterally affixed long satellite rod (Right) constructs. The red oval shapes show the location of the maximum von Mises stress on the rods..... 92

Figure 5-14 The von Mises stress contour on the instrumentation during flexion in 4-rod posteriorly affixed short satellite rod (Left) and 4-rod posteriorly affixed long satellite rod (Right) constructs. The red oval shapes show the location of the maximum von Mises stress on the rods..... 94

Figure 5-15 The von Mises stress contour on the instrumentation during flexion in 2-rod (Left) and short-rod (Right) constructs. The red oval shapes show the location of the maximum von Mises stress on the rods..... 96

Figure 5-16 Comparison of the instrumented T10-S1 global ROM for different loading cases and different configurations of interbody spacers..... 99

Figure 5-17 Comparison of the instrumented T10-S1 global ROM for different loading cases and different locations of the cross-connector..... 102

Figure A-1 Comparison of the instrumented T10-S1 global ROM for different loading cases before and after adding interbody spacers plus bone grafts at above and below the PSO level.....135

## List of Abbreviations

|            |                                    |
|------------|------------------------------------|
| AF.....    | Annulus Fibrosus                   |
| ALL.....   | Anterior Longitudinal Ligament     |
| ASD.....   | Adult Spinal Deformity             |
| BDBO.....  | Bone-disc-bone Osteotomy           |
| CEP.....   | Cartilaginous Endplate             |
| CL.....    | Capsular Ligament                  |
| COCR.....  | Cobalt Chromium                    |
| CT.....    | Computed Tomography                |
| EXT.....   | Physiological Extension Motion     |
| FE.....    | Finite Element                     |
| FEA.....   | Finite Element Analysis            |
| FLEX.....  | Physiological Flexion Motion       |
| HRQOL..... | Health Related Quality of Life     |
| IS.....    | Interspinous Ligament              |
| ITL.....   | Intertransverse Ligament           |
| IVD.....   | Intervertebral Disc                |
| LB.....    | Physiological Left Bending Motion  |
| LF.....    | Ligamentum Flavum                  |
| LL.....    | Lumbar Lordosis                    |
| LLIF.....  | Lumbar Lateral Interbody Fusion    |
| LR.....    | Physiological Left Rotation Motion |
| MIS.....   | Minimally Invasive Surgery         |
| MRI.....   | Magnetic Resonance Imaging         |
| NP.....    | Nucleus Pulposus                   |
| PI.....    | Pelvic Incidence                   |
| PJK.....   | Proximal Junctional Kyphosis       |

PLL..... Posterior Longitudinal Ligament  
PSO..... Pedicle Subtraction Osteotomy  
PT..... Pelvic Tilt

RB..... Physiological Right Bending Motion  
RF..... Rod Fracture  
ROM..... Range of Motion  
RR..... Physiological Right Rotation Motion

SPA..... Sacral-pelvic Angle  
SPO..... Smith-Peterson Osteotomy  
SS..... Sacral Alope  
SSA..... Spino-sacral Angle  
SSL..... Supraspinous Ligament  
SVA..... Sagittal Vertical Axis

TI..... Titanium Alloy  
TK..... Thoracic Kyphosis  
TPA..... T1 Pelvic Angle  
TLIF..... Transforaminal Lumbar Interbody Fusion  
T1SPI..... T1 Spinopelvic Inclination

VCR..... Vertebral Column Resection

XLIF..... Extreme Lateral Interbody Fusion

# **1 Introduction**

## **1.1 Rationale for Research**

Over the last two decades, adult spinal deformity surgeries have broadly increased. The sagittal imbalance is common in adult spinal deformity which has been associated with severe pain, and mental and physical disabilities [1, 2]. Sagittal malalignment can cause inability to stand erect, significant pain in the lumbar spine, and impair ambulation [3, 4]. Iatrogenic flatback syndrome, degenerative lumbar flatback deformity, ankylosing spondylitis, post traumatic kyphosis, and post-laminectomy kyphosis are the leading causes of sagittal imbalance [5-7].

Following advances in spinal instrumentation and techniques, management of the sagittal malalignment has gone through a significant evolution. In this regard, spinal osteotomy surgeries have evolved to achieve balance, inhibit the deformity progression, and mitigate pain in the patients [8]. Among the realignment techniques, pedicle subtraction osteotomy (PSO) has become a dominant method to correct the adult spinal deformity.

PSO is a three-column posterior osteotomy in which the posterior elements, pedicles, and a v-shaped wedge through the pedicles are resected. This procedure does not lengthen the anterior column and provides between 25° to 35° of sagittal correction [9].

PSO provides a wide bone-on-bone contact area which increases the stability and decreases the risk of pseudoarthrosis. The technique uses the anterior cortex of the vertebral body as a hinge to close the wedge resection. The osteotomy is closed using instrumentation, and the rods are acutely contoured at the PSO level. In general, following PSO, at least three levels below and above the osteotomy site are instrumented with pedicle screws [8].

Despite multiple benefits of the PSO in addressing the spinal sagittal imbalance, it is a technically demanding procedure. There is a significant risk of serious complications and revision surgery following this procedure. Overall, reported complication rates following PSO are significantly high, and they range between 37% and 59% [10, 11]. A major complication associated with the PSO is rod breakage, and the rate of postoperative complication has been reported to be as high as 31.6% [12]. Smith et al., in their prospective multicenter study, found 9% of rod fracture following adult spinal deformity surgery. In patients who underwent PSO with a minimum of 1-year follow-up, the rate was increased to 22% [12]. In a multicenter retrospective study of 442 patients, Smith et al. observed 15.8% symptomatic rod fracture in patients who underwent PSO from which 89% experienced it at or adjacent to the PSO site [13].

Generally, rod fracture can cause pseudoarthrosis, severe pain, and loss of deformity correction in patients which may lead to revision surgery. Multiple reported risk factors that influence the rod fracture in patients with sagittal malalignment include age, preoperative sagittal imbalance, body mass, fusion extent, pelvic and sacrum fusion, inadequate anterior column support, inadequate correction, use of side-by-side connectors, rod bending, rod contouring, sharp rod angle, repeated rod contouring, rod material type and rod diameter [13-17]. Aside from these factors, in a recent study conducted by Briski

et al., lumbar disc geometry was indicated as a risk factor affecting rod failure [18]. In their retrospective study, they compared the height of the intervertebral discs in two groups of patients with and without rod fractures. The authors observed that the group consisting of patients with rod fracture had larger non-fused disc heights, diameters and volumes.

To mitigate the mechanical complication and decrease the rod fracture rate following the PSO, various methods such as the use of interbody spacers at the disc spaces adjacent to the PSO, adding of one or two additional satellite rods, and Cobalt Chromium (COCR) rods instrumentation have been shown to be clinically beneficial [12, 13, 19-21]. Deviren et al. investigated the use of interbody cages adjacent to the PSO level [22]. The results of their study suggested that adding interbody cages adjacent to the PSO with bilateral pedicle screw instrumentation enhances the stability of the construct. Additionally, Hyun et al. compared the implant failure in the two groups of standard 2-rod constructs to multiple-rod constructs [21]. The lower rate of primary rod fracture (2-rod: 11 vs. multi-rod: 2) was reported for the multi-rod group. It has been well established that the fatigue life of the COCR rods is greater than the stainless steel and titanium alloy (TI), and that the TI material is highly notch-sensitive [23-25]. Slivka et al. studied the effect of contouring on fatigue strength of TI, COCR, and stainless steel spinal rods [23]. The authors found 25% greater endurance limit for COCR rods compared to the other materials. Among the frequently used implant materials (COCR, TI, and stainless steel), COCR is the stiffest and densest material which has the greatest ultimate stress [24, 26].

Despite various efforts to study the PSO in recent years, the biomechanical reasons for the high rate of complications remain unclear. Only a few computational studies were

accomplished on this complicated topic [16, 17, 27, 28]. In those simulations, either a simplified model were used, or only a few instrumentation configurations were considered.

The overall goals of this project are I) modeling and analyzing the effect of lumbar disc geometry on the rods following PSO and II) modeling and analyzing different alternative instrumentation configurations (multi-rods, interbody spacers, and cross connectors) following PSO. As a first step, to address the hypotheses of this study, a T10-pelvis PSO FE model will be generated. The generated model will establish a basis for extending the analysis on multiple discs degenerated spine models. Besides, various instrumentation techniques will then be simulated on the healthy disc model.

We have two specific goals, each with multiple hypotheses to evaluate:

**Specific Aim 1: Analyze the effect of lumbar disc degeneration on the instrumentation following PSO.**

Hypothesis 1.1: The maximum von Mises stress on the rods occurs at or adjacent to the PSO region.

Hypothesis 1.2: Larger discs allow more motion, particularly adjacent to the PSO site.

Hypothesis 1.3: Larger discs result in increased rod stresses, and ultimately greater rod fracture rate.

**Specific Aim 2: Analyze the effect of alternative instrumentation configurations including multi-rod (medially, laterally, and posteriorly affixed**

**secondary rods and short-rod technique proposed by Gupta et al. [29]), interbody spacer, and cross-connector constructs.**

Hypothesis 2.1: Adding multiple rods to the PSO setting increases the stability and decreases the maximum von Mises stress at the PSO region on the rods.

Hypothesis 2.2: Adding interbody spacers to the PSO setting improves the stability and decreases the rods' maximum von Mises stress.

Hypothesis 2.3: Adding cross-connectors to the PSO setting increases the rotational stability of the construct.

## **2 Biomechanical Anatomy of the Spine**

### **2.1 Overview**

In this chapter, a review of the spine anatomy and its functional biomechanics is provided. The anatomical structures of different regions of the spine including vertebral bodies, intervertebral discs, ligaments, and facets are described in detail. In the end, biomechanics of the disc degeneration and pertaining literature studies are broadly reviewed.

### **2.2 Introduction**

The upper and lower limbs of the human body are linked together by a complex structure called the spine [30]. The spine, which also referred to as the vertebral column, is formed of four principal curvatures. To the anterior part of the body, the cervical and lumbar vertebrae are creating convex curves, while the concave curvatures are made by the thoracic and sacrococcygeal regions. A spring-like response is induced by these four curvatures to provide the overall robustness of the vertebral column [31]. During the daily activities, the S-shaped curvature of the spine provides flexibility and energy absorption.

The vertebral column is divided into five distinct regions of cervical, thoracic, lumbar, sacral, and coccygeal. This column constitutes of 33 vertebrae including seven cervical (C1-C7), 12 thoracic (T1-T12), five lumbar (L1-L5), five fused sacral (S1-S5), and five fused coccygeal (tailbone) vertebrae. Figure shows the lateral and posterior views of the spine consisting of five different regions. The motion in the spine is mainly enabled by the cervical and lumbar segments as compared to the rigid thoracic and pelvic regions.

The spine can be further divided into two subgroups of anterior and posterior segments. The anterior segment of the spine includes vertebral bodies, intervertebral discs, anterior and posterior longitudinal ligaments. Vertebral bodies of the spine are nearly an elliptical cylinder with a proximal concave and distal convex surfaces [32]. This portion of the anterior column is composed of a low-density core of trabecular bone covered by a thin layer of compact bone. Vertebral bodies are the massive anterior portion of the spinal column which supports human weight and are linked together with fibrocartilaginous intervertebral discs. During a day, due to the activities, the water content of the discs decreases that leads to approximately 15 to 25 mm shortening of the column [33].

The posterior portion of the spine consists of intervertebral joints, neural arches, spinous and transverse processes, and ligaments. A neural arch includes two pedicles and two laminae which are formed of hard bone that resists tensile forces. There are two synovial joints on the proximal and distal border of the lamina which protect the discs from extreme rotation and shear [33]. Spinous and transverse processes are the attachment regions of the muscles running through the vertebral column [34].

## 2.3 Cervical Spine

The proximal cervical spine is formed by the base of the skull (C0), and the two cervical vertebrae, the atlas (C1) and the axis (C2), which have dissimilar structures to any other vertebrae. The atlas is a ring-like vertebra with large transverse processes, and without any spinous process or vertebral body [34]. The upper joint between the atlas and the skull is called occipito-atlanto joint (C0-C1) which provides approximately 10° to 15° of motion during flexion and extension with no lateral bending and axial rotation [35, 36]. The axis vertebra has no articulating process and instead is articulating via the atlas using a pillar called the odontoid process or dens. This articulation between the axis and the atlas is called atlantoaxial joint which provides about 10° of motion during flexion and extension, 47° to 50° during axial rotation, and no motion of lateral bending [35].

The remaining cervical vertebrae (C3-C7) are responsible for the weight bearing of head, flexibility, and responding to the muscle forces. These vertebrae are more similar to the typical vertebrae of the spine. They have small bodies, short pedicles and spinous processes, and large articulating processes [34]. The cervical vertebrae can provide approximately 80° to 90° of flexion, 70° through extension, lateral bending of 20° to 45°, and about 90° of axial rotation [34, 36].

## 2.4 Thoracic Spine

Thoracic region is one the most rigid parts of the spine due to the rib-vertebra articulations, the overlapping of long spinous processes, and facets orientation. Moving caudally, the vertebrae are increasing in size and become taller in the vertebral height. Thoracic vertebrae have long transverse processes, and the spinous processes are oriented

caudally rather than posteriorly. The facet joints in this region are angled at  $20^\circ$  to the coronal plane and  $60^\circ$  to the transverse plane [34]. Moving posteriorly, the range of motions of flexion, extension, and lateral bending increase while the axial rotation decreases. The lateral bending and axial rotation motions in this region range from  $2^\circ$  to  $9^\circ$  [35, 37]. At the thoracic region, the intervertebral discs have the greatest disc diameter to the disc height ratio which causes to decrease the tensile stress on the vertebrae [38]. Hence, lower disc injuries are expected in the thoracic spine than other regions of the vertebral column. The ribs are not attached to the T11 and T12 levels which are called “floating ribs” [32].

## **2.5 Lumbar Region**

The lumbar region is formed of 5 large vertebrae which are the most significantly loaded segments of the spine. Lumbar vertebrae have wide bodies with short pedicles, broad spinous processes, and small transverse processes. Similar to the cervical spine, the intervertebral discs in the lumbar region are thicker dorsally and ventrally. It has been shown that the ventral disc height of this region remains nearly constant during the age range of 16 to 57 years [39]. Similar to thoracic region, moving caudally in the lumbar region, the vertebral sizes increase. The range of motion (ROM) of the lumbar region during flexion and extension is relatively large and varies between  $8^\circ$  and  $20^\circ$  at different levels. Lateral bending ( $3^\circ$  to  $6^\circ$ ) and axial rotation ( $3^\circ$  to  $6^\circ$ ) motions are more restricted in this region [35, 37]. The lumbosacral joint is responsible for a large proportion of flexion motion (about 75%) of the lumbar region, followed by the L4-L5 joint (about 20%) [40].

## **2.6 Sacral and Coccygeal Regions**

The sacral spine is formed by five fused vertebrae (S1 to S5). The sacrum is nearly triangular-shaped bone and joins with the pelvis through the sacroiliac joint. The sacroiliac joint transfers the loadings of the upper extremities to the pelvis. The coccygeal region, known as the tailbone, is a small triangular region immediately below the sacrum. It functions as to stabilize the sitting posture of the human body.

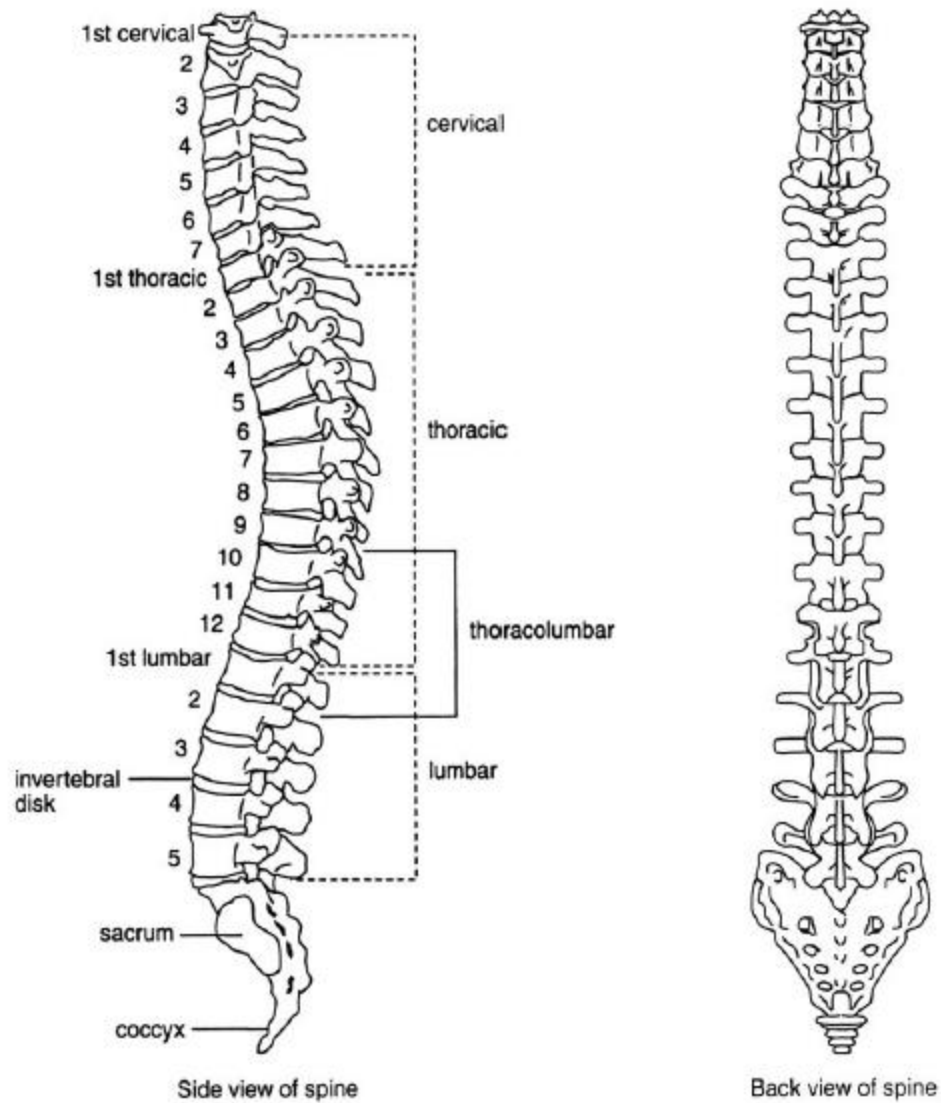


Figure 2-1 Lateral and posterior views of a normal spine showing different regions of cervical, thoracic, lumbar, sacral, and coccygeal regions [41].

## 2.7 Facet Joints

When the inferior articular process of the superior vertebra and the superior articular process of the inferior vertebra come across, the facet joint (zygapophyseal joint) is formed.

These joints are located on the postero-lateral sides of each motion segment in the spine. Main constituents of the facet joints are the bony articular pillars which provide the opposing surfaces, the synovium that sustains lubrication for the articular surfaces, and capsular ligaments that cover the whole joint [42-45]. Across each vertebral segment, loads are transmitted by these joints working conjointly with the discs. Facet joints restrict the relative motion between two adjoining vertebrae, thus deterring the possible overload and detrimental effects on the neighboring parts like the spinal cord, the nerve roots and the intervertebral discs [46]. During joint rotations and translations, the bony pillars resist compression forces while the capsular ligaments support tensile loads [47-49].

Yang and King studied the compressive load applied to the lumbar region and found that 75-97 % of the load is carried by the intervertebral discs, and 3-25% is borne by the facets [50]. In another similar experiment, Adams and Hutton calculated that under 560-1030 N compression force and 2 degrees of extension, 16% of the force is carried by the facet joints [51]. Alignment of these joints is also distinct across the spinal sections and each vertebral level [52, 53]. In the cervical and upper thoracic areas of the spine, articular surfaces of the bony articular pillars are horizontally aligned, which facilitates a greater amount of axial rotation and lateral bending motion coupling [54-57]. Due to more vertical alignment in the lower thoracic and lumbar segments, lateral bending and rotational motions are limited [46], while the flexion and extension motions are predominantly occurring in these regions. In the lumbar region, partial and total facetectomies considerably enhance rotation during flexion and axial rotation in motion segments subjected to 200N compressive forces and 8Nm moment [58]. In a cadaveric study conducted by Tender et al, they reported that the unilateral facetectomy considerably increased the ipsilateral (1.4°) and overall (3°) axial

rotations [59]. Figure 2-1 represents the lateral and posterior views of a functional spinal unit showing facet joint and intervertebral discs.

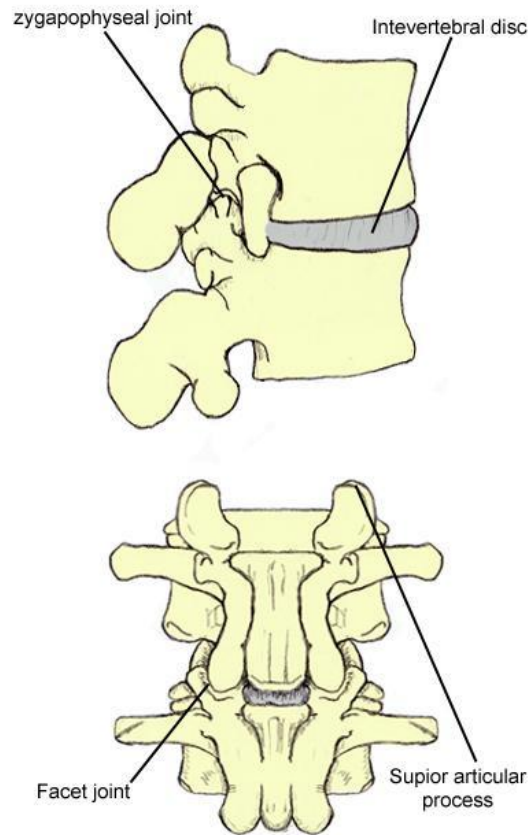


Figure 2-1 Lateral and posterior views of a functional spinal unit showing facet joint and intervertebral discs. (Source: <http://img.medscapestatic.com/pi/meds/ckb/59/12059.jpg>)

## 2.8 Spinal Ligaments

Ligaments of the spine provide safety to the spinal cord and stabilize the spine by carrying tensile forces during physiological motions. Most of these fibers are innervated and, due to this, are a feasible location of pain [60]. Panjabi et al. studied the physical properties of spinal ligaments and observed the highest failure deformation in supraspinous

ligament which is the farthest ligament from the center of rotation of the lumbar vertebrae and the least failure deformation in the two anterior and the posterior longitudinal ligaments (closest to the center of rotation) [61]. In another biomechanical study, Nolte et al. reported that with increasing the distance from the axis of rotation strain capacity of the ligament increases. Based on their observations, with increasing flexion motion, the anterior and posterior longitudinal ligaments play a subordinate role while the ligamentum flavum (LF), facet capsular ligament (CL), interspinous (IS) and supraspinous (SSL) ligaments are rotational stabilizers [60]. The most important spinal ligaments are described in more details below (Figure 2-2).

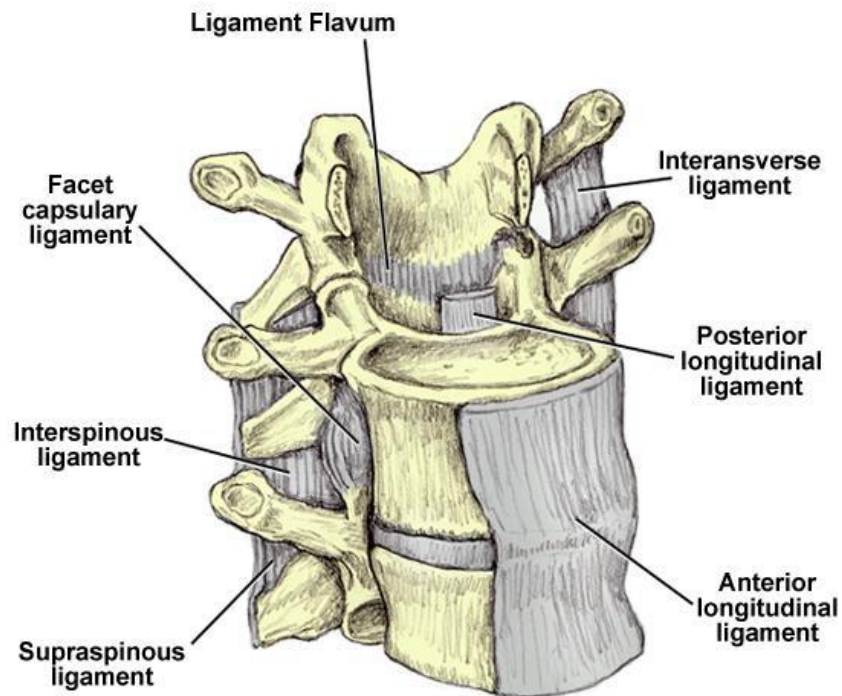


Figure 2-2 Anterolateral representation of a lumbar functional spinal unit demonstrating the spinal ligaments. (Source: <http://img.medscapestatic.com/pi/meds/ckb/60/12060.jpg>)

### **2.8.1 Anterior Longitudinal Ligament (ALL)**

A band of collagenous fibers runs alongside the anterior part of the vertebral column and intervertebral discs which is termed as the anterior longitudinal ligament. Among all other ligaments, ALL is one of the strongest and densest ligaments with relatively great size. ALL restrains the extension motion in the spine [62] and limits the anterior movement of one vertebra over another [34]. This powerful ligament sustains a persistent load on the spine, and in lifting, it supports the anterior portion of the discs [63].

### **2.8.2 Posterior Longitudinal Ligament (PLL)**

These ligaments are extending through the posterior region of the vertebral column and intervertebral discs. In the lumbar region, overall mean stiffness of PLL is lower than the ALL [64]. PLL restrains the flexion motion of the spine whereas it has a limited function in resisting the axial rotation [34, 65]. However, the removal of PLL may cause rotation in motion segment [66]. Compared to the other lumbar spinal ligaments, PLL was reported to have the lowest cross-sectional area with a mean value of 5.2 mm<sup>2</sup> [64]. Similar failure stresses were reported for ALL (8.2-16.1 MPa) and PLL (7.2-28.4 MPa) [64].

### **2.8.3 Ligamentum Flavum (LF)**

Lamina of the adjoining vertebrae is linked together by a chain of ligaments called ligamentum flavum extending through the base of the skull to the pelvis [67]. During flexion of the spine, vertebral laminae detachment is resisted by LF [67]. Flexion and lateral bending are opposed by LF, and it has no significant role in resisting the axial

rotation [65]. By restricting abrupt flexion, LF contributes in maintaining the normal spinal curve and intervertebral discs safety [67-69].

#### **2.8.4 Supraspinous Ligament (SSL)**

In the vertebral column, the supraspinous ligaments link the posterior tips of the spinous processes [67, 68, 70]. As SSL proceeds caudally, it becomes wider in the lumbar area [71]. SSL functions to restrict the flexion as compared to other motions [67, 72]. Gudavalli and Triano modeled the lumbar spinal ligaments and found that during flexion motion the SSL carries the greatest amount of force [73]. The maximum energy to failure values reported for SLL and ALL ranged from 3.18 to 11.64J and from 0.82 to 8.68J, respectively [64]. SSL was reported to show the greatest strain at failure [64].

#### **2.8.5 Interspinous Ligament (ISL)**

The interspinous ligament collaterally extends along the spinous processes [67, 68]. The ISL shows poor resistance to flexion [72]. Hindle et al. found that when the SSL was dissected, the ISL carried 75% of the force [74]. It was reported that ISL is not carrying any load during the lateral bending motion [75]. Among all lumbar ligaments, ISL has shown the lowest stiffness value ( $11.5 \pm 6.6 \text{ Nmm}^{-1}$ ) [64].

#### **2.8.6 Intertransverse Ligament (ITL)**

In the vertebral column, these ligaments exist in the intermediate region of the transverse processes. In lateral bending, ITL plays a significant role in carrying a

considerable amount of load [75]. Compared to other ligaments, there is no loading of the ITL when torsion is induced [76].

### **2.8.7 Facet Capsular Ligament**

The capsular ligaments encase the facet joints and are connected to the margins of the articular processes [46]. In all types of loading orientations, the capsular ligaments are strained [65]. Movement of the vertebrae is significantly limited by the CL [46]. The restriction of motion by CL is particularly ascertained during flexion motion [77].

## **2.9 Intervertebral Disc (IVD)**

Each vertebra in the spinal column is divided by a heterogeneous, fibrocartilaginous structure known as the intervertebral disc which helps in maintaining the flexibility and motion of the spine [78-80]. The discs allow the spine to bend and rotate, and transfer loads to the adjacent vertebral bodies [67, 81]. IVDs are thicker in the anterior part of the cervical and lumbar spine, while they are more uniform in the thoracic region [82]. It was shown that the IVD could resist compressive loads ranging between 2500N and 7650N [83]. Under greater amount of loads, IVDs behave stiffer while they are more flexible when subjected to the lower loads. Broberg et al. reported a linear increase in disc pressure with an increase in compressive load [84]. The pressure was measured 30 to 50% greater than the applied force per unit area [84]. The three most important components of the

intervertebral discs are the outer annulus fibrosus (AF), the central nucleus pulposus (NP), and the cartilaginous end plate (CEP) [85] (Figure 2-3).

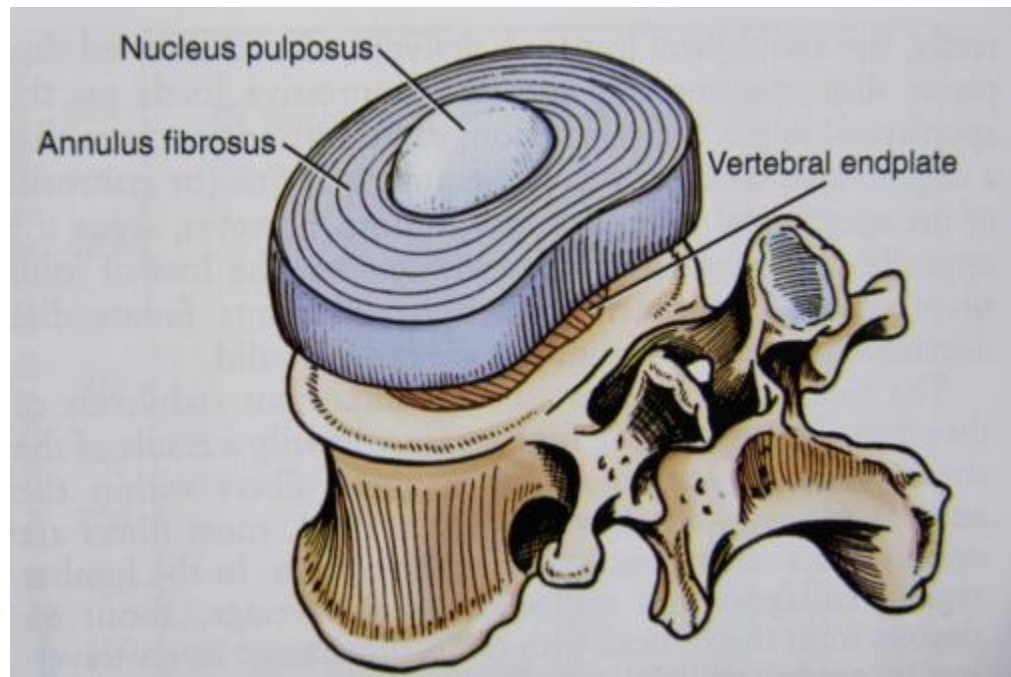


Figure 2-3 Posterolateral view of a intervertebral disc showing annulus fibrosus, nucleus pulposus, and vertebral endplate [32].

### **2.9.1 Annulus Fibrosus (AF)**

The anisotropic annulus fibrosus which surrounds NP and consists of approximately 15-25 concentric layers of collagen fibers called lamellae [86, 87]. The fibers are oriented diagonally at an angle of  $45^{\circ}$ - $65^{\circ}$  to the vertebral segments [88, 89]. This orientation of fibers in AF restrains the excessive shear loading and axial rotation motion between the vertebral bodies [34]. The AF can also be divided into the outer fibrous region and the inner fibrocartilaginous component [90]. In any anomalous micro-

movement of the disc, initially, the motion is restrained by the fibers present at the periphery of the AF [91, 92]. To the anterior part of the AF, the fibers are stiffer which provide resistance to stretching [93]. It is shown that the stiffness in the inner and posterior parts of AF is significantly lesser than the outer and anterior parts [94-98].

### **2.9.2 Nucleus Pulposus (NP)**

40-50% of the intervertebral disc volume is occupied by a gelatinous isotropic structure called NP [99, 100]. The main constituents of the NP are proteoglycan, collagen, and water [101]. The isotropic and homogeneous nucleus pulposus contains a large number of proteoglycans (Accounts for 35-65% of dry weight) providing a hydrodynamic behavior. The proteoglycans have a significant impact on the mechanical properties of the discs by binding the water into the tissue [99, 102]. With gradual decrease in the proteoglycan content of NP, the load-bearing behavior of the disc is highly affected [79]. The Collagen type II fibrils function to hold the nucleus together [86]. During compression loading, the hydrostatic pressure rises in the NP which creates tension in the adjacent AF [103-105]. The hydrostatic ability of the nucleus pulposus reduces gradually with aging, resulting in tears and gaps formation [106, 107].

### **2.9.3 Cartilaginous End Plate (CEP)**

The cartilaginous endplates in IVDs have a thickness of around 0.6 mm which are located between the NP and vertebral endplate [108]. These endplates are formed by a thin layer of hyaline cartilage and fibrocartilage that contribute in nutrient transportation to the

disc [109]. About 60% of CEP is occupied by water, and the rest is composed of collagen type II, and proteoglycans [105].

## **2.10 Disc Degeneration**

Intervertebral disc degeneration is a prevalent cause of low back pain and disability in the elderly population. The disc degeneration is commonly attributed to age, inadequate nutrition, genetic inheritance, and the history of loading [81, 110]. During the early stages of disc degeneration, the water and proteoglycan content of the nucleus pulposus reduce, which can lead to swelling pressure and disc height reduction [111-113]. With increasing disc degeneration, the collagens in the NP increase and make it stiffer and more fibrotic [114, 115]. Following this phenomena, the annulus and nucleus border becomes indistinguishable [81]. Due to discs dehydration during the degeneration process, the intradiscal pressure would reduce, and greater compressive load will transfer to the AF [116]. Main geometric changes associated with disc degeneration are AF bulging, osteophytes growth, endplate curvature alterations, and height reduction [117]. The biochemical and geometrical changes during disc degeneration result in biomechanical alterations of the spinal column such as changes in stiffness, ROM, and loadings. In the literature, there are contradictory observations of the degenerated discs' ROM. For severe disc degeneration, most of the studies reported stiffening of the segment compared to the healthy discs [118-120]. However, for the mild degeneration, instability was observed in some studies [121-123]. The reason for the variation in ROM of cadaver studies could be due to creep loading and endplate damage which do not necessarily indicate early degeneration [120]. Another reason for this discrepancy can be the study design, and the

number of specimens tested [120]. Moreover, testing different levels of specimens together while they differ in the stiffness and ROM may cause this inconsistency in the outcomes. Figure 2-4 shows the lateral view of a spine segment demonstrating healthy and degenerated discs.

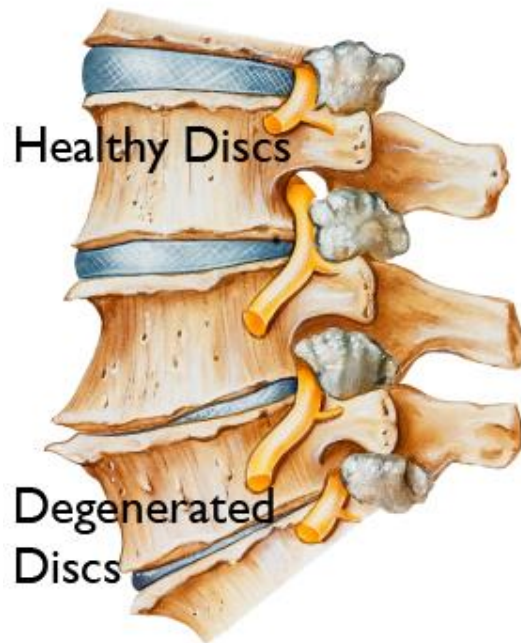


Figure 2-4 Lateral view of a spine segment showing healthy and degenerated discs. (Source: <https://healthspines.org/wp-content/uploads/2015/08/DDD.jpg>)

Kettler et al. in an in vitro study, evaluated the effect of disc degeneration on the flexibility of the lumbar spine [120]. They rated the degree of disc degeneration in 203 segments based on three criteria of height loss, osteophyte formation, and sclerosis. For assessing the ROM, an external moment of  $\pm 7.5\text{Nm}$  was applied to each segment. Their study indicated that with progress in disc degeneration, the stability in flexion/extension and lateral bending increases while the axial rotation decreases [120]. Mimura et al. have

conducted a similar study on disc degeneration. In their study, a maximum moment of 10 Nm was applied to test the flexibility of the segments. They observed that with an increase in disc degeneration, the ROM in flexion/extension and lateral bending decreased, while the axial rotation initially increased then decreased [118]. A brief description of in vitro studies that evaluate the effect of disc degeneration on the ROM is given below (Table 2.1).

Table 2.1 Summary of in vitro ROM studies on the disc degeneration [120]

| Study           | Number of discs | Age range | Classification system   | Grades | Flexibility test                                      | ROM in flexion/extension | ROM in lateral bending | ROM in axial rotation |
|-----------------|-----------------|-----------|---|--------|---|--------------------------|------------------------|-----------------------|
| Mimura et al.   | 47              | 35-64     | Radiographic (own system)   | 1 to 4 | Pure moments<br>±10 Nm                                |                          |                        |                       |
|                 |                 |           | Macroscopic (transverse slices: according to Nachemson [9])                                     |        |   |                          |                        |                       |
| Krismer et al.  | 36              | 20-92     | Macroscopic (transverse slices: according to Nachemson [9])                                     | 1 to 4 | Pure moments<br>±8.5 Nm                               | -                        |                        |                       |
| Oxland et al.   | 24              | Unknown   | Macroscopic (transverse slices plus removed nucleus material: according to Vernon-Roberts [95]) | 1 to 4 | Pure moments<br>±10 Nm plus<br>200 N axial<br>preload |                          |                        |                       |
| Fujiwara et al. | 110             | 39-88     | Magnetic resonance imaging (sagittal slices according to Thompson [96])                         | 1 to 5 | Pure moments<br>±6.6 Nm                               |                          |                        |                       |
| Tanaka et al.   | 114             | 39-87     | Macroscopic (sagittal slices according to Thompson [96])  | 1 to 5 | Pure moments<br>±5.7 Nm                               |                          |                        |                       |
| Kettler et al.  | 203             | 18-99     | Radiographic (according to Wilke [88])  | 0 to 3 | Pure moments<br>±7.5 Nm                               |                          |                        |                       |

The disc degeneration influence on the biomechanical behavior of the spine motion segments was also evaluated in different finite element (FE) studies. Rohlmann and colleagues simulated four different models of L3-L4 with the healthy, mildly degenerated, moderately degenerated, and severely degenerated disc. To simulate different motions of flexion, extension, lateral bending, and axial rotation, the inferior endplate of L4 was constrained in all degrees of freedom and pure moments of 10 Nm were applied to the proximal endplate of L3. They reported a similar trend of intersegmental rotation to the cadaveric study of Mimura et al. For axial rotation, they recorded an increasing motion followed by a decrease in severe degeneration. Also, the intradiscal pressure was lower, whereas the facet joint force and maximum von Mises stress in the AF were greater in the degenerated disc models [124]. Schmidt et al. under complex loadings, investigated the risk of healthy, mild, moderate, and severe disc degeneration prolapse at L4-L5 lumbar segment. In mildly degenerated disc, they observed an increase of ROM in flexion extension and axial rotation. In the moderate degeneration disc model, compared to healthy disc, only axial rotation showed greater ROM, and in the severe disc degeneration, the ROM in all directions decreased significantly [125]. In 2013, Park and colleagues conducted an FE analysis on different disc degeneration grades at the L4-L5 motion segment, and in terms of range of motion they reported that with further increase in disc degeneration, the intersegmental motions of flexion, extension, and lateral bending reduced while the axial rotation initially increased with mild and moderate degeneration and reduced with severe degeneration [126].

## **3 Literature Review**

### **3.1 Overview**

The purpose of this chapter was to review the adult spinal deformities more specifically sagittal malalignment, surgical treatment approaches, and treatment complications. Clinical, in-vitro, and in-silico studies related to instrument complications followed by pedicle subtraction osteotomy were discussed in this chapter.

### **3.2 Introduction**

Adult spinal deformity (ASD) is one of the most prevalent spinal disorders amongst elderly populations. ASD incorporates a broad spectrum of spinal disorders including adult scoliosis, degenerative scoliosis, kyphosis after osteoporotic vertebral fractures, degenerative kyphosis, sagittal and coronal imbalance, and iatrogenic spinal deformity [1, 2]. Historically, ASD assessment was attributed to the evaluation of the coronal plane. Over the last two decades, more attention was given to the significance of the sagittal plane. Sagittal plane imbalance of the spine has been associated with severe pain, and mental and physical disabilities [2, 7, 127]. Several etiologies have been recognized to be responsible for the sagittal plane deformities. The most prevalent causes include ankylosing spondylitis, post-laminectomy kyphosis, degenerative kyphosis, iatrogenic flat back

syndrome (fixed sagittal imbalance), and post traumatic kyphosis [5, 6, 128]. Treatment of the sagittal plane malalignment depending on the cause, location, and severity of the deformity varies among the patients [7].

### **3.3 Nomenclature**

Sagittal plane balance can be evaluated using radiographic imaging and clinical assessment.

Pelvic and spinal radiographic parameters are defined below.

#### **C7 plumb line**

The C7 plumb line is a vertical line dropped from the center of the C7 vertebral body and is used to assess the spinal alignment in sagittal and coronal planes. This line should intersect the upper endplate of S1.

#### **Pelvic incidence (PI)**

PI is the angle subtended by the line connecting the center of femoral heads and S1 superior endplate and the perpendicular to the sacral plate (Figure ).

#### **Pelvic tilt (PT)**

PT is the angle between the line connecting the center of the femoral heads and the midpoint of the S1 end plate and the vertical line originating at the center of the femoral heads (Figure ).

#### **Sacral slope (SS)**

SS is described as the angle subtended by the superior S1 endplate and the horizontal line (Figure ).

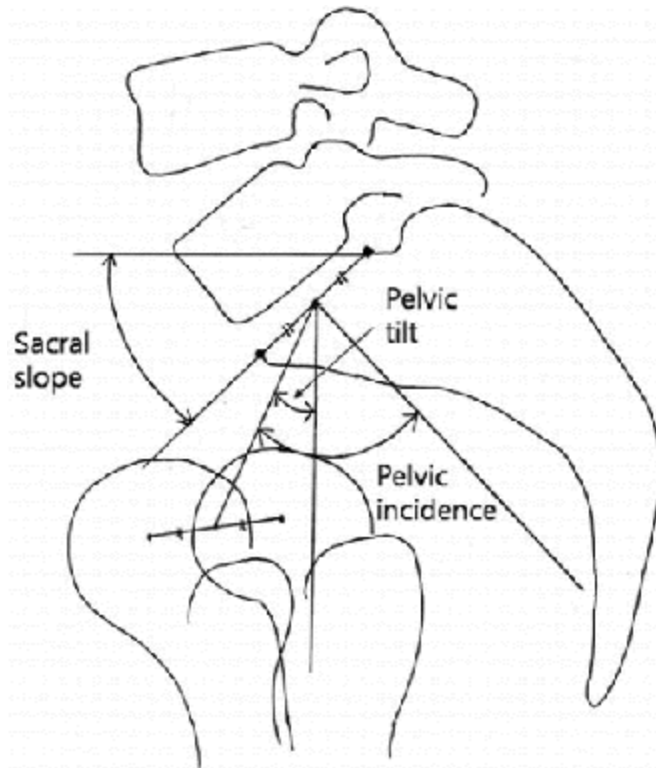


Figure 3-1 A demonstration of pelvic parameters including Pelvic tilt, sacral slope, and pelvic incidence. (Source: <http://www.eneurosurgery.com/wpimages/wp09866018.png>)

### **Sacral-pelvic angle (SPA)**

SPA is the angle between the line from the sacral endplate to the center of the femoral head and the line connecting the center of C7 to the midpoint of the sacral endplate.

### **Spino-sacral angle (SSA)**

The angle subtended by the line originating from the center of C7 to the center of the sacral endplate and the sacral endplate surface.

### **Sagittal vertical axis (SVA)**

The SVA is defined as the distance between the posterosuperior corner of S1 and the vertical plumb line of C7 (Figure 3-2).

## **Lumbar lordosis (LL)**

LL is defined as the angle between the superior endplates of L1 and S1 (Figure ).

## **Thoracic kyphosis (TK)**

TK is the angle between the superior endplate of T4 and inferior endplate of T12 (Figure ).

## **T1 Pelvic angle (TPA)**

TPA is described as the angle subtended by a line connecting the femoral head axis to the T1 centroid and the line passing through the S1 superior end plate midpoint and the femoral head axis.

## **T1 Spinopelvic inclination (T1SPI)**

T1SPI is the angle between the line connecting the femoral head axis to the centroid of T1 and the vertical line originating at the center of the femoral heads. TPA angle is the sum of the PT and T1SPI (Figure ).

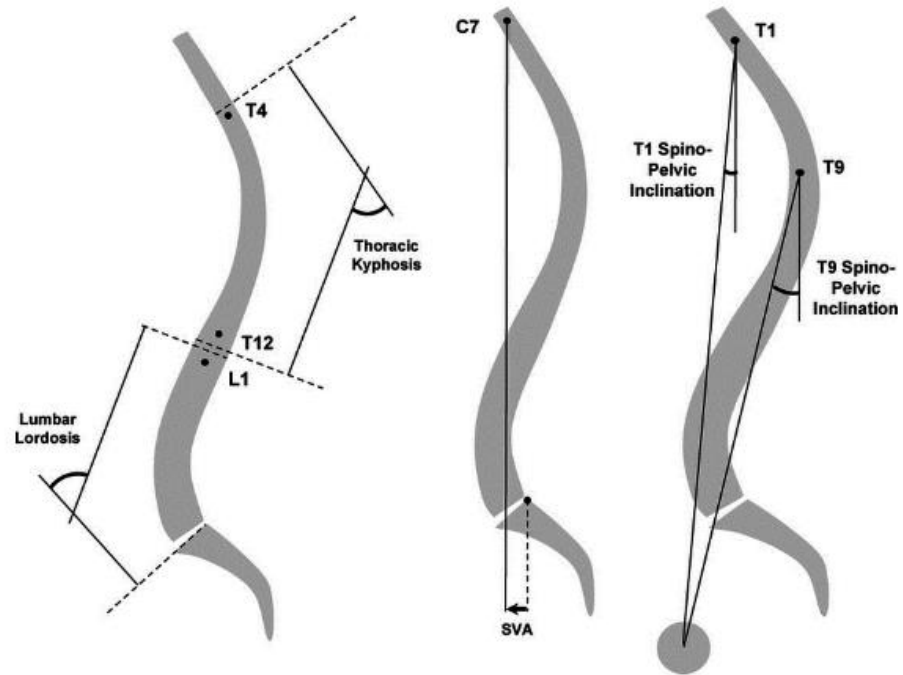


Figure 3-2 Sagittal spinal radiographic parameters. In this figure thoracic kyphosis (TK), lumbar lordosis (LL), T1 and T9 spinopelvic inclination angles and sagittal vertical axis (SVA) were demonstrated [129].

### 3.4 Normal Sagittal Balance

During the ideal sagittal spinal alignment, the standing posture of an individual is associated with the minimal muscular expenditure [130]. The economy concept cone proposed by Dubousset (Figure ) [130] represents a range of position for the body to sustain the balanced posture without the need of external support.

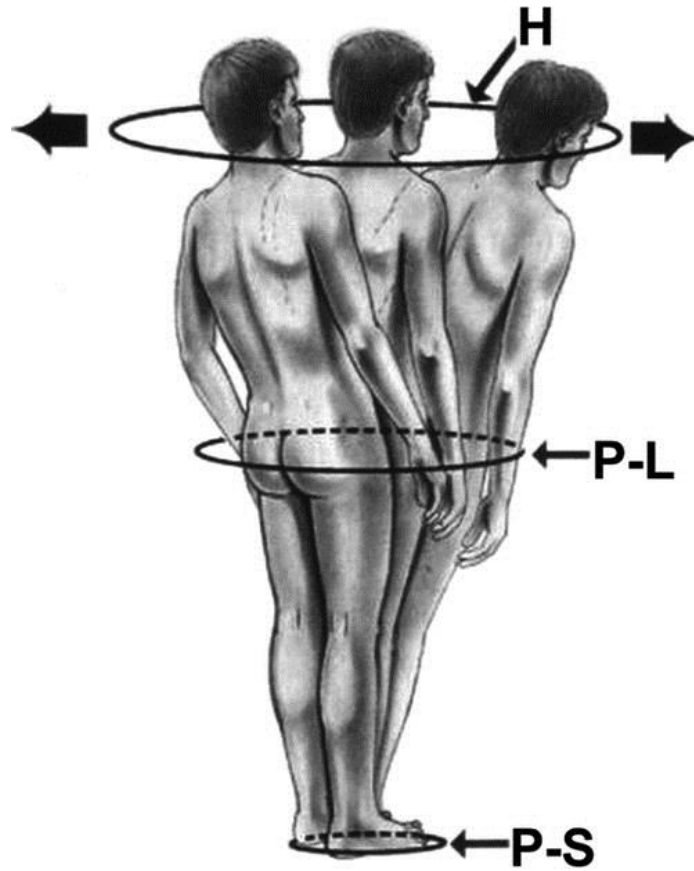


Figure 3-3 Cone of balance or economy. Deviation from the zones shown in the figure results in energy expenditure and muscular effort [129].

For healthy individuals, the PI angle ranges between  $34^\circ$  and  $84^\circ$ . This angle measures about  $52^\circ$  [131, 132]. Pelvic incidence is not changing after the adolescence [133]. The mean offset value reported for the SVA is 0.5 cm. SVA offset value of greater than 2.5 cm is assumed as an imbalance. The body represents a positive sagittal balance if the C7 plumb line is located anterior to the posterosuperior aspect of the S1, and it represents negative sagittal balance if it falls posterior to the posterosuperior aspect of the S1. The normal value for the PT measures approximately  $12^\circ$  with a range between  $5^\circ$  and  $30^\circ$  [131]. This angle is more of a posture related angle which alters with different postures [134]. Typically, SS

angle ranges from 20° to 65° with an approximate value of 40° [131, 132]. Similar to the pelvic tilt, this also is a posture related angle. There is a relationship between the pelvic parameters and the sacral slope such that the summation of PT and SS is equal to the pelvic incidence ( $PT+SS=PI$ ) [133]. The normal value of the thoracic kyphosis ranges from 20° to 50°. This value for the lumbar lordosis measures from 31° to 79° [134].

Lafage et al. have demonstrated that the T1SPI has a higher correlation with Health Related Quality of Life (HRQOL) than SVA and PT [135]. Schwab et al. have also suggested that the ultimate goal of sagittal imbalance correction surgeries should be lumbar lordosis within 9° of the pelvic incidence angle,  $SVA < 50$  m,  $PT < 20^\circ$ , and  $T1SPI < 0^\circ$  [129].

### **3.5 Sagittal Imbalance Etiology**

Sagittal imbalance in the spine can arise from iatrogenic causes or metabolic and genetic disorders such as ankylosing spondylitis and osteoporosis [7]. Bridwell et al. categorized the fixed sagittal imbalance into primary and secondary causes [136]. The primary cause of the fixed sagittal imbalance is multilevel degeneration of the discs which often is accompanied with degenerative scoliosis. Multilevel degeneration will result in loss of lordosis and anterior column height. The secondary cause of sagittal malalignment relates to the iatrogenic complications and previous spinal fusion surgeries. The application of distraction instrumentations such as Harrington rods as well as the use of compressive anterior instrumentation have been recognized to cause sagittal malalignment. Another reason for the iatrogenic flat back syndrome is recognized to be the failure to attain sufficient lumbar lordosis angle during posterior spinal fusion. Kyphosis or post traumatic

kyphosis can also develop following spinal fusion which may be the result of pseudoarthrosis or adjacent to a previous fusion [7].

### **3.6 Spinal Osteotomies**

The primary purpose of spinal deformity surgery is to achieve balance, inhibit the deformity progression, and mitigate pain in the patients [8]. With the advent of powerful techniques and instrumentation, spinal osteotomies have evolved to correct sagittal and coronal deformities of the spine. The posterior osteotomies are considered where the instrumentation alone or facet or ligament releases are not adequate to address the deformity. Before, any decision for the surgery, flexibility assessment of the curve is required to determine the surgical approach, spinal fusion levels, and osteotomy necessity. In general, if the deformity correction on the bending radiograph is less than 30%, the curve is considered as rigid and requires osteotomy [137].

The primary types of osteotomies are the Smith-Peterson osteotomy (SPO), pedicle subtraction osteotomy (PSO), bone-disc-bone osteotomy (BDBO), and vertebral column resection (VCR) (Figure ). SPO requires merely posterior column removal of the bone, while the PSO, BDBO, and VCR involve bone resection extending from posterior column to the anterior column (Three-column osteotomies). A review of each osteotomy type is given below.

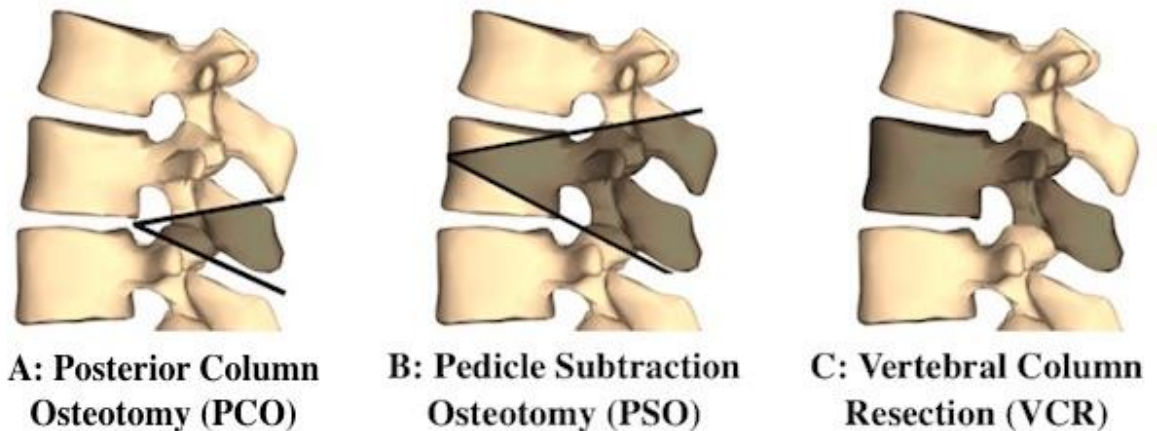


Figure 3-4 Different types of posterior spinal osteotomies. Smith-Peterson/PCO osteotomy (Left). Pedicle subtraction osteotomy (Middle). Vertebral column resection (Right). (Source: <http://columbiaspine.org/wp-content/uploads/2016/01/Deformity-correction-copy-1.jpg>)

### 3.6.1 Smith-Peterson Osteotomy (SPO)

SPO is a posterior column type of osteotomy which involves the resection of the spinous process, supraspinous, intra-spinous ligaments, ligamentum flavum, inferior lamina, and facet joints. The SPO uses the posterior side of the disc as a hinge, and the correction occurs through the intervertebral disc. In this osteotomy, the anterior column is lengthened while the posterior column is shortened [138, 139]. By applying compressive forces to the whole disc space, using posterior instrumentation, the osteotomy maintains closure. Using SPO approximately  $10^\circ$  ( $1^\circ/\text{mm}$  bone resection) of lordosis correction can be achieved [8, 138, 140]. Generally, in patients with a C7 plumb line in the positive range of 6 cm to 8 cm, SPO is used. Among the other osteotomies, SPO is the least complex surgery and can be applied in both coronal and sagittal plane deformities. However, when

intervertebral discs become rigid, as in the case of osteophyte formation, this type of osteotomy is not practical [141].

### **3.6.2 Pedicle Subtraction Osteotomy (PSO)**

PSO is a three column osteotomy in which the posterior elements, pedicles, and a v-shaped wedge through the pedicles are resected. This technique uses the anterior cortex of the vertebral body as a hinge to close the wedge resection. PSO provides a wide contact area at the bony surfaces of the posterior, middle, and anterior columns which diminishes the risk of pseudoarthrosis and enhances the stability [142]. Pedicle subtraction osteotomy can be used in both coronal and sagittal plane correction of spine curvatures. This procedure shortens the posterior column without lengthening the anterior column. Patients with sharp or angular kyphosis with significant sagittal malalignment >10 or 12cm, and those who have ankylosing spondylitis, iatrogenic flack back, and immobile deformities for whom the SPO cannot be effective, can benefit this technique [138, 140, 143]. PSO provides a greater correction than SPO, and it does not need a flexible intervertebral disc. However, the procedure is more challenging than the SPO and is accompanied by a significant blood loss (up to 2 liters). Cho et al. found about twice as much blood loss in a single PSO than in three levels of SPO [144]. In different studies, the reported degree of correction with the PSO has an average of 32° and ranges between 26.2° and 40.1° [4, 138, 140, 143, 145-148]. In the lumbar region, due to an adequate distal number of fixation points, PSO mostly tends to be performed at L2 or L3 levels [138]. It was shown by Roussouly that in most patients the apex of the lumbar lordosis is located at the L4 vertebra [149]. Besides, it was demonstrated that about 70 % of lumbar lordosis is occurring at L4-

S1 level [150]. Hence, optimal correction may happen by having the PSO at L4. Even though L4 vertebral body morphology provides more correction and mostly lower lumbar spine governs the lumbar lordosis angle, due to clinical aspects it is frequently not possible to carry out the osteotomy at this level. In this regard, Ottardi et al. recently performed a finite element study of the PSO at L3 and L4 levels and found a higher range of motion and instability at L4 [28]. In a prospective series of 63 cases, Cogniet et al. studied the clinical and radiological outcomes of PSO. They found that PSO is highly effective in patients possessing pelvic incidence of less than 60 degrees ( $PI < 60^\circ$ ), but as the pelvic incidence increases the PSO becomes less effective [151]. Instrumentation for the PSO should be performed prior to the osteotomy. In general, at least three levels below and above the osteotomy level are instrumented using pedicle screws [8]. At the osteotomy level, the rods are acutely contoured to correspond with the spine sagittal profile. Salvi et al. conducted a biomechanical study comparing the SPO and PSO for the surgical correction of kyphotic deformities. They found multilevel SPO can provide similar correction to one level PSO, however, the instrumentation load was higher in the PSO than multilevel SPO [152].

### **3.6.3 Bone-disc-bone Osteotomy (BDBO)**

In BDBO, the intervertebral disc with its adjacent end-plate(s) is resected. Usually, when the intervertebral disc space is at the apex or center of the rotational axis of the deformity, this type of osteotomy is preferred [153]. In addition, wherever a severe sagittal plane deformity exists which PSO correction is not sufficient, BDBO can be used. This type of osteotomy can be applied in three different types, and each type can provide

different amounts of deformity correction. The degree of correction with this technique ranges between 35° and 60° [8, 153]. Instrumentations in BDBO can be used at least two levels below and three levels above the osteotomy level. The bone-to-bone closure of the osteotomy region can be performed using the instrumentation which reduces the risk of pseudoarthrosis. In a group of patients with highly rigid kyphotic deformities treated with BDBO, Domanic et al. found an average of 49° of correction [154]. The advantage of this technique over the vertebral column resection is its high degree of correction and safety in the preservation of nerve roots while performing in the lumbar spine region [155].

#### **3.6.4 Vertebral Column Resection (VCR)**

In this technique, posterior elements of the VCR level, the vertebral body at the apex of the deformity, and the adjacent vertebral discs are resected [156]. VCR provides sagittal and coronal balance using shortening of the spinal column [156-158]. Usually, this method is accompanied by anterior fusion and use of anterior cages which increases the correction angle and anterior column height. Among different osteotomies, this technique provides the greatest correction of the deformity. It is mainly used for severely rigid multi planar deformities, sharp curvatures, hemivertebra, spondyloptosis, congenital kyphosis, resection of spinal tumors, and post traumatic deformities [2, 140, 153]. In the series of 70 patients, Suk et al. reported correction of 61.9° and 45.2° in coronal and sagittal planes, respectively [156]. While VCR is the most effective osteotomy of the spine, there is a significant risk of morbidity and neurological injury with this technique.

### **3.7 Minimally Invasive Surgery (MIS) Approaches for ASD**

Improvements in minimally invasive approaches for spinal fusion have led to ASD complication management by hybrid techniques. The use of MIS techniques decreases the amount of soft tissue trauma and morbidity in these surgeries. Park and colleagues compared two different MIS techniques to treat the ASD [159]. One group underwent hybrid techniques, including an initial multilevel lumbar lateral interbody fusion (LLIF) insertion and a secondary traditional open segmental posterior osteotomy. The other group, underwent a combination of MIS techniques using LLIF and transforaminal lumbar interbody fusion (TLIF) insertion. TLIF was used only in two patients. Instrumentation was performed in all patients, and none of them received any osteotomy or facet resection. Both approaches led to a considerable correction in the lumbar coronal deformity with a little improvement in the hybrid group. The hybrid group showed greater lumbar lordosis and decreased SVA. However, the complications rate was greater with the hybrid approach. Recently, a mini-open PSO method was described by Wang and Bordon, in which the patients underwent a minimally invasive posterior instrumentation followed by an open surgery on the osteotomy and adjacent levels only. They showed the feasibility of their technique with satisfactory radiographic outcomes. However, the complications rate with this technique was still high, and similar complications to the open surgery fashion were reported with the use of this technique [160].

### **3.8 Osteotomies and Complications**

Even though osteotomies are very efficient in addressing the spinal sagittal imbalance, these techniques are considered malignant and require accurate planning and

understanding of the risk factors. There are several complications associated with the use of osteotomies categorized as early and late complications. Primary late complications reported are proximal junctional kyphosis (PJK), pseudoarthrosis, rod fracture, screw loosening, and prominent iliac screws. Early complications included massive blood loss, neurological deficits, wound infection, dural tear, etc. [142]. Smith et al. studied the short-term morbidity and complications accompanied with fixed sagittal plane deformity correction. 402 cases (70%) out of five hundred seventy-eight patients were treated using osteotomies, including 135 SPO, 215 PSO, 18 VCR, 19 anterior discectomies with corpectomy techniques, and 15 unspecified osteotomies. They found 170 (29.4%) complications in 132 patients with the morbidity rate of 0.5%. Short-term complications included durotomy (5.9%), wound infection (3.8%), the new neurologic deficit (3.8%), implant failure (1.7%), wound hematoma (1.6%), epidural hematoma (1.4%), and pulmonary embolism (1%). Furthermore, they found that more aggressive osteotomies were associated with higher rate of complications from SPO (28.1%), to PSO (39.1%), to VCR (61.1%) [10].

In 2016, in a prospective multicenter study, Smith et al. investigated the perioperative and minimum 2-year complication rates accompanied with ASD surgery. In 203 patients, they reported 469 complications which mostly included implant related, radiographic, neurologic, operative, cardiopulmonary, and infection. A greater rate of complications occurred in patients with older age, higher body mass index, previous spine surgery, and three-column osteotomies [161].

Kim et al. retrospectively studied PSO in 35 patients with a minimum of 5 years follow up. As a late complication (More than 6months), they reported ten pseudarthroses

(29%) which mainly occurred at the thoracolumbar junction (90 percent). These complications were recognized due to localized patient pain complaints or instrumentation failure [145]. Buchowski et al. evaluated neurologic complications of PSO in 108 patients, and reported 12 intraoperative and postoperative deficits (11.1%) which 3 of them were permanent deficits [3]. In an investigation of 140 consecutive patients who were treated using PSO with a follow up of 8 years, Kim et al. found zero cases pseudoarthrosis [162]. In 2005, using a clinical approach, Cho et al. compared three or more SPOs to one PSO, and found a greater risk of coronal deformity deterioration in the group of patients treated with three or more SPOs than a single PSO [144].

### **3.9 Instrumentation Failure Following PSO**

Among several complications of PSO, instrumentation failure is a common source of complication and revision surgery [161]. Generally, rod fracture (RF) can be associated with significant impacts on the patients. It may develop pseudoarthrosis, severe pain, and loss of deformity correction in patients. RF can also reflect the instruments fatigue due to pseudoarthrosis [13]. As a result of these impacts, revision surgery may be required to address the complications.

Several risk factors have been reported to affect the rod fracture rate. These factors can be categorized in three subsets of patient-related, technique-related, and implant-related factors. Factors such as age, preoperative sagittal imbalance, lumbar disc geometry, and body mass can be assumed as patient-related factors. The extent of fusion levels, pelvic and sacrum fusion, inadequate anterior column support, inadequate correction with remaining sagittal imbalance, use of side-by-side connectors, rod bending and contouring,

sharp rod angle, and repeated rod contouring are the technique-related factors which influence the RF rate. For the implant-related factors, material type and diameter can play a significant role in RF [13-18]. A literature review of clinical, in vitro, and in silico studies of the factors affecting instrumentation failure following PSO is provided below.

### **3.9.1 Clinical Studies**

In a multicenter retrospective study of 442 patients, Smith et al. assessed the symptomatic rod fracture in adult spinal deformity. Authors reported 30 symptomatic RF (6.8%) in 442 patients. The RF rate after PSO was shown to be 15.8% (18 of 114 patients), and failure occurred at or adjacent to the level of the PSO region in 89% (16 out of 18) of the failures. In patients treated with PSO, they found a lower rate of RF with cobalt chromium (COCR) composition (7%) than stainless steel (17%) and titanium alloy (25%). Authors suggested higher body mass index (BMI) and postoperative residual sagittal imbalance may increase the risk of RF [13]. Similarly, Yang et al., Bridwell et al., and Upadhyaya et al. reported cases of RF at the PSO level [4, 163, 164].

In 2014, Smith et al. in a prospective multicenter investigation of rod fracture following ASD surgery, reported 9% (18 in 200 patients) of RF. The authors found that patients with RF were older, had greater BMI and higher correction of sagittal imbalance. The rate of RF in patients treated with PSO was 22%, and 10 out of 11 fractures occurred at the PSO region. The observed rate of RF was greater in patients treated with cobalt chromium rods than with stainless steel and titanium alloy rods [12]. In a recent investigation of rod stiffness in 54 patients who underwent ASD surgery, Han et al. found

a greater rate of RF with titanium alloy two-rod constructs (32.4%) compared with COCR multiple-rod construct (0%). In contrast, proximal junctional kyphosis occurrence was greater in COCR multiple-rod construct (60%) versus titanium alloy two-rod construct (26.5%) [165].

Berjano et al. evaluated the factors of failures in sagittal imbalance surgery. They determined insufficient correction, junctional kyphosis, screw loosening and pseudoarthrosis with rod fracture as the causes of failure and revisions [15].

In a recent study conducted by Briski et al., lumbar disc geometry was indicated as a risk factor affecting the rod failure. In their retrospective study, they compared the height of the intervertebral discs in two groups of patients with and without rod fractures. Thirty-seven patients were included in their study. Group one consisted of 11 patients who had experienced rod fracture, while the group two were 26 patients who did not have any evidence of rod fracture. The authors observed that the group of patients who experienced the rod fracture had larger non-fused disc heights, diameters and volumes [18].

In a retrospective study conducted by Barton et al., the authors investigated the risk factors for RF after posterior osteotomy in 75 patients with ASD. They found sagittal rod contour  $>60^\circ$ , the existence of dominos or parallel connectors, pseudoarthrosis at  $\geq 1$  year follow-up, and fusion construct crossing both lumbosacral and thoracolumbar junctions as the risk factors of rod fracture [14].

For three-column spinal osteotomies fixation, Hyun and colleagues compared the two groups of standard 2-rod constructs to multiple-rod constructs. In their retrospective study, each group included 50 patients treated with PSO and 16 patients with VCR. Significant differences were reported in the occurrence of revision surgery for

pseudoarthrosis and rod fracture between the two groups. Rod failure in the 2-rod constructs occurred in 11 cases while there were only two partial implant failures in multi-rod constructs.

Gupta et al. have recently reported on a 4-rod technique in which the principal rods were not connected to the pedicle screws anchored adjacent to the PSO levels, while additional two short rods were spanning on PSO level using anchors connected to the adjacent levels. They compared the rod fracture rate using this novel method with the traditional 2-rod technique, and reported 0 % rod failure with 4 rods, compared to a 25% of fracture with the 2 rods [29].

### **3.9.2 In-Silico and In-Vitro Studies**

A finite element (FE) study of the instability and instrumentation after PSO conducted by Charosky et al. demonstrated that the secondary motion of torsion during the lateral bending increased 200%. In their analysis, they also simulated high dehydrated and completely degenerated discs integrated with PSO at L4 level. They concluded that the primary instability after PSO is rotational and it increases with the disc degeneration [16].

In another FE analysis of the instrumentation following PSO, Luca et al. studied the effects of rod material, diameter, and bilateral dual parallel rod construct. Their results showed lower stresses for the titanium rods compared to COCR rods. In addition, the lowest stress was ensured in the multiple rod constructs [17].

Recently, Luca and colleagues in an FE analysis investigated the effect of anterior support on the posterior instrumentation following PSO. They simulated 30° of PSO at the L3 level and instrumented the adjacent intervertebral discs to PSO in three different cases

of above, below and both discs using transforaminal lumbar interbody fusion (TLIF) and extreme lateral interbody fusion (XLIF) cages. They evaluated the range of motion of the simulated models using  $\pm 7.5$  Nm moment on the cranial end plate of L1. The authors reported 4% reduction of motion using one cage, and with the use of two cages, it increased to about 8% reduction of motion. The force measured on the rods reduced by 3-8 % by the use of one cage, while by using two cages this magnitude increased to 15-17 %. Using single cage adjacent to the PSO region, the maximum von Mises tensile stress on the rods decreased about 20-30 %, whereas employing two cages resulted in 42-51 % reduction in the stress [27].

In 2012, Tang et al. conducted a biomechanical study on the severity of rod contour in a PSO setting. The authors performed biomechanical fatigue tests of the modified F1717 settings of 20, 40, and 60 degrees titanium alloy contoured rods at 400 N/40 N and 250 N/25 N. They found that the fatigue life of the rods depends significantly on the severity of the rod angle, and more severe angles have greater risk of fracture [166].

In an in vitro study, Hallager et al. investigated the use of supplemental short pre-contoured accessory rods. Eight constructs were tested to assess the range of motion and rod strain in: 1-Accessory rods added to the PSO; 2-Titanium composition versus COCR rods; 3-Use of interbody grafts adjacent to the PSO level. Accessory rods were attached to the primary rods medially, and a maximum moment of  $\pm 10$  Nm was applied caudally to the specimens. They found that the accessory rods experienced greater strain than the primary rods, and with the use of interbody spacers both accessory and main rods demonstrated lower strain. The greatest strain reduction occurred in COCR 4 rods instrumented with interbody spacers. They concluded that interbody spacers slightly

contributed to the stability and strain reduction when used adjacent to the PSO, and they are more responsible for maintaining the disc height [167].

Deviren et al. investigated the use of interbody cages adjacent to PSO level in flexion-extension, right/left lateral bending, and right/left axial rotation motions followed by fatigue bending test. The results of their study suggested that adding interbody cages adjacent to the PSO with bilateral pedicle screw instrumentation may enhance the rigidity of the construct. In the fatigue testing, the addition of cages increased dynamic stiffness of the PSO construct by 22.2% [22].

## **4 Material and Methods**

### **4.1 Overview**

In this section, the methodology used for the T10-pelvis finite element model development was initially described. Subsequently, the procedures used to make the PSO models of healthy and lumbar disc degeneration are elucidated in detail. Following this, further description of various instrumentation designs and their employment in the PSO models is given. This chapter also includes an explanation of the material properties used for the spinal elements and instrumentations. In addition, boundary conditions and loading protocols for different simulations are fully described. Finally, model validation and comparison of the various outcomes to the literature data is explained.

### **4.2 Finite Element Model Development**

This study was performed using a validated nonlinear, three-dimensional finite element model of the human thoracolumbosacral spine (T10-Pelvis) [32]. A brief description of the intact model development is given below.

The intact model of the ligamentous spine was based on computed tomography (CT), and magnetic resonance imaging (MRI) scans of a normal human with 1mm slice

thickness. MIMICS (Materialize Inc., Leuven, Belgium) software was utilized to produce the three-dimensional geometry of the spine and pelvis. Subsequently, IAFE-MESH (University of Iowa, Iowa) and HyperMesh (Altair Engineering, Michigan, USA) software was used to create the hexahedral elements (C3D8) and Tetrahedron (C3D4) elements on the components. Following meshing, all the components were assembled in the Abaqus 6.14 (Dassault Systèmes, Simulia Inc., Providence, RI) software.

The vertebral bodies were simulated using a trabecular (Cancellous) bone core surrounded by a thickness of 0.5 mm compact (Cortical) bone. Posterior region and vertebral body of the spine were modeled using three-dimensional eight nodes solid continuum elements. Extracted isotropic material properties from the literature were assigned to different bony regions.

The facet joints of the spine were simulated using three-dimensional GAPUNI elements with an initial gap of 0.5 mm. Articular surfaces were assigned an exponential contact that adjusts the force as the distance between the surfaces decrease. The cartilaginous layer at the sacroiliac joint was simulated using soft contact with force adjusting exponential behavior. Material properties of the bony structure and joints are presented in Table .

Table 4.1 Material properties of bony structure and joints of the spine and pelvis.

| <b>Component/ Material</b> | <b>Element Formulation</b> | <b>Constitutive Model</b> | <b>Young's Modulus (Mpa)</b> | <b>Poisson's Ratio</b> |
|----------------------------|----------------------------|---------------------------|------------------------------|------------------------|
| <b>Bony Structure</b>      |                            |                           |                              |                        |
| Vertebral Cortical Bone    | Hexahedral                 | Elastic                   | 12000                        | 0.3                    |

|                           |              |                         |       |     |
|---------------------------|--------------|-------------------------|-------|-----|
| Vertebral Cancellous Bone | Hexahedral   | Elastic                 | 100   | 0.2 |
| Posterior Cortical Bone   | Hexahedral   | Elastic                 | 12000 | 0.3 |
| Posterior Cancellous Bone | Hexahedral   | Elastic                 | 100   | 0.2 |
| Pelvic Cortical Bone      | Tetrahedron  | Elastic                 | 17000 | 0.3 |
| Pelvic Cancellous Bone    | Tetrahedron  | Elastic                 | 10    | 0.2 |
| <b>Joints</b>             |              |                         |       |     |
| Apophyseal Joints         | GAPUNI       | Non-linear soft contact | --    | --  |
| Sacroiliac Joints         | Soft Contact | Exponential Behavior    | --    | --  |

The main seven ligaments of the spine including anterior longitudinal, posterior longitudinal, capsular, ligamentum flavum, interspinous, supraspinous, and intertransverse ligaments were simulated using three-dimensional two-node truss elements (T3D2). Respective cross-sections were assigned to the spinal ligaments. Hypoelastic nonlinear material behavior was defined for each ligament based on their force-deflection curve. Six main pelvis ligaments were simulated similar to the spinal ligaments which are presented in Table . Initially, all ligaments were assumed to be in zero stress position.

Table 4.2 Material properties of the spine and pelvis ligaments.

| <b>Component/ Material</b> | <b>Element Formulation</b> | <b>Constitutive Model</b> | <b>Young's Modulus (Mpa)</b> | <b>Poisson's Ratio</b> |
|----------------------------|----------------------------|---------------------------|------------------------------|------------------------|
| Anterior Longitudinal      | Truss (No compression)     | Non-linear Hypoelastic    | 7.8 (<12%), 20 (>12%)        | 0.3                    |
| Posterior Longitudinal     | Truss (No compression)     | Non-linear Hypoelastic    | 10 (<11%), 20 (>11%)         | 0.3                    |

|                    |                        |                        |   |     |
|--------------------|------------------------|------------------------|---|-----|
| Ligamentum Flavum  | Truss (No compression) | Non-linear Hypoelastic | 15 (<6.2%),<br>19.5 (>6.2%)                             | 0.3 |
| Intertransverse    | Truss (No compression) | Non-linear Hypoelastic | 10 (<18%),<br>58.7 (>18%)                               | 0.3 |
| Interspinous       | Truss (No compression) | Non-linear Hypoelastic | 10 (<14%),<br>11.6 (>14%)                               | 0.3 |
| Supraspinous       | Truss (No compression) | Non-linear Hypoelastic | 8 (<20%),<br>15 (>20%)                                  | 0.3 |
| Capsular           | Truss (No compression) | Non-linear Hypoelastic | 7.5 (<25%),<br>32.9 (>25%)                              | 0.3 |
| Anterior SI        | Truss (No compression) | Non-linear Hypoelastic | 125 (<2.5%),<br>175 (>5%),<br>325 (>10%),<br>316 (>15%) | 0.3 |
| Inner Posterior SI | Truss (No compression) | Non-linear Hypoelastic | 43 (<2.5%),<br>61 (>5%),<br>113 (>10%),<br>110 (>15%)   | 0.3 |
| Outer Posterior SI | Truss (No compression) | Non-linear Hypoelastic | 150 (<2.5%),<br>211 (>5%),<br>391 (>10%),<br>381 (15%)  | 0.3 |
| Intraosseus        | Truss (No compression) | Non-linear Hypoelastic | 40 (<2.5%),<br>57 (>5%),<br>105 (>10%),<br>102 (>15%)   | 0.3 |
| Sacrospinous       | Truss (No compression) | Non-linear Hypoelastic | 304 (<2.5%),<br>428 (>5%),<br>792 (>10%),               | 0.3 |

|                |                        |                        |   |     |
|----------------|------------------------|------------------------|---|-----|
|                |                        |                        | 771<br>(>15%)   |     |
| Sacro-tuberous | Truss (No compression) | Non-linear Hypoelastic | 326 (<2.5%),<br>458 (>5%),<br>848 (>10%),<br>826 (>15%) | 0.3 |

The intervertebral discs were simulated using a composite structure composing of both annulus fibrosis and nucleus pulposus. The structure of annulus fibrosis was simulated as a solid ground substance reinforced with rebar elements. This ground substance was formed of three-dimensional hexahedral elements and was assigned Neo-Hookean hyperelastic material properties. The strain energy potential for the Neo-Hookean material is given in

Equation 1.

$$U = C_1(\bar{I}_1 - 3) + \frac{1}{d}(J - 1)^2$$

Equation 1

In Equation 1,  $C_1$  is the material constant that characterizes the deviatoric deformation,  $\bar{I}_1$  is the first deviatoric strain invariants,  $d$  is the material compressibility, and  $J$  is the local volume ratio.

Rebar elements were embedded into the ground matrix of the annulus with alternating angles of  $\pm 30^\circ$  to the transverse plane. For modeling the tension only behavior of the annulus fibers, “No compression” choice was selected for rebar elements. Moving from center to the outer layers, the thickness and stiffness of the fibers increased [168].

C3D8 hexahedral elements were utilized in the simulation of the nucleus pulposus. The nucleus pulposus was simulated using hyperelastic Mooney-Rivlin formulation ( $C_1$ ,  $C_2$ ). The strain energy potential of the Mooney-Rivlin material is defined by Equation 2.

$$U = C_1(\bar{I}_1 - 3) + C_2(\bar{I}_2 - 3) + \frac{1}{d}(J - 1)^2$$

Equation 2

In Equation 2,  $C_1$  and  $C_2$  are material constants that characterize the deviatoric deformation,  $\bar{I}_1$  and  $\bar{I}_2$  are first and second deviatoric strain invariants,  $d$  is the material compressibility, and  $J$  is the local volume ratio. The material properties of the disc components were presented in Table .

Figure shows the lateral and posterior views of the validated FE model of the spine and pelvis which was used for this study.

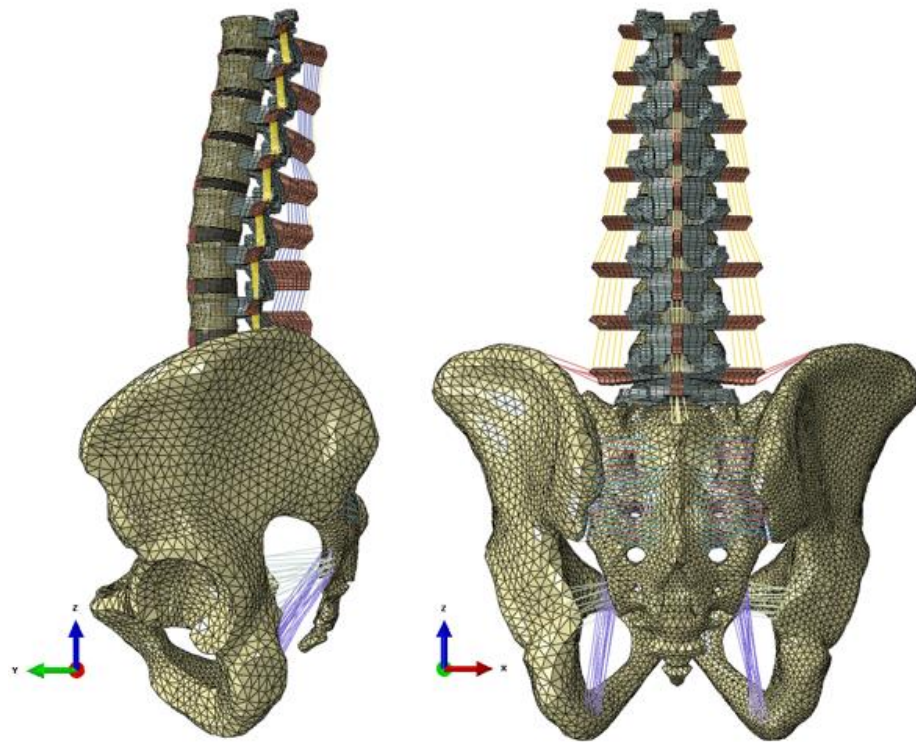


Figure 4-1 Lateral (Left) and posterior (Right) views of the spinopelvic model used for this study.

### 4.3 PSO Finite Element Model Development

This section describes the method utilized to create a finite element spinopelvic model treated with PSO at the L3 level, which was later used as a basis to produce different grades of disc degeneration representations integrated with PSO. The T10-Pelvis model was changed to simulate the PSO at the L3 level of the spine. To achieve this, posterior elements including posterior arch, posterior ligaments, transverse ligaments, interspinous ligaments, and supraspinous ligaments were removed initially. Subsequently, along with pedicles and transverse processes removal, a wedge-shaped bone resection of  $30^\circ$  was

performed at the vertebral body of L3. To simulate the closure of wedge resection at this level, the proximal part of L3 along with other upper levels were rotated around the anterior cortex of the L3 vertebral body until the two resected extremities touch. A surface to surface contact with a friction of 0.46 was defined between the two resected extremities [28, 169]. Figure shows the lateral and posterior views of the spinopelvic model following PSO at the L3 level.

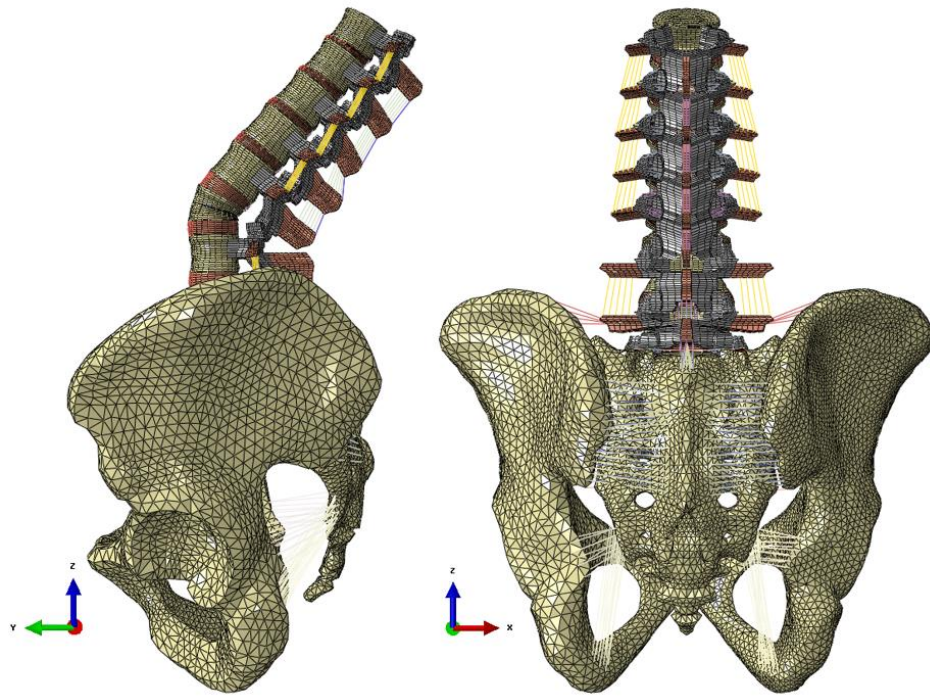


Figure 4-2 Lateral (Left) and Posterior (Right) views of the spinopelvic pelvic model following 30° of PSO at the L3 level. At the PSO level, posterior elements including posterior arch, posterior ligaments, transverse ligaments, interspinous ligaments, and supraspinous ligaments were removed.

## **4.4 Disc Degenerated PSO Finite Element Models Development**

Using a previously developed PSO model with healthy discs, three different simplified grades of degenerated lumbar discs (mild, moderate, and severe) were generated. The degeneration of the discs was simulated at all lumbar levels of the spine. To simulate the disc degeneration at different levels of the spine, the disc height was reduced, the compressibility of the nucleus was increased, and fiber and ligament stiffness were altered.

The height of the lumbar discs was reduced based on the grading system of disc degeneration described by Wilke et al. [117]. In their grading system, grade 0 was defined as 0%, grade 1 as 0-33%, grade 2 as 33-66%, and grade 3 as 66-100% height loss. However, to concentrate on the discs degeneration, in our study the formation of osteophyte and diffuse sclerosis were neglected. Compared to the normal disc height of different lumbar levels, the mild, moderate, and severe degenerated discs were simulated by a disc height reduction of 20%, 50%, and 80%, respectively. Lateral views of the developed models integrated with PSO and accompanied with various lumbar disc degeneration grades are shown in Figure . The anterior, posterior and average discs' heights of the lumbar segment for the healthy and degenerated models are given in Table 1.

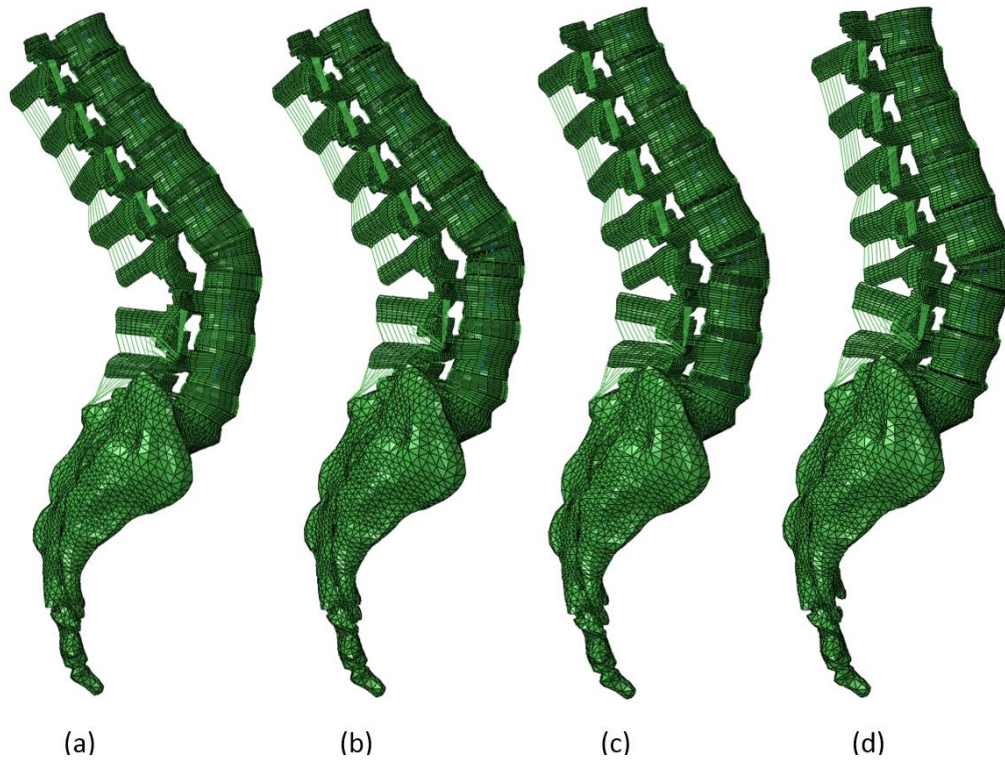


Figure 4-3 Lateral views of the developed spinopelvic FE models integrated with 30° of PSO at the L3 level accompanied with various lumbar intervertebral disc degeneration grades: (a) Healthy discs; (b) Mildly degenerated; (c) Moderately degenerated; (d) Severely degenerated. For the sake of intervertebral discs visualization, the ilium bones were not shown in this figure.

Table 1.3 Height measurements for healthy, mildly degenerated, moderately degenerated, and severely degenerated intervertebral discs of the lumbar segment.

| Disc Level | Anterior Disc Height (mm) | Posterior Disc Height (mm) | Average Disc Height (mm) | Average Mild Degenerated Disc Height | Average Moderate Degenerated Disc Height | Average Severe Degenerated Disc Height |
|------------|---------------------------|----------------------------|--------------------------|--------------------------------------|--|--|
| L1-L2      | 8.11                      | 6.54                       | 7.33                     | 5.86                                 | 3.66                                     | 1.47                                   |
| L2-L3      | 12.22                     | 7.45                       | 9.84                     | 7.87                                 | 4.92                                     | 1.97                                   |
| L3-L4      | 9.98                      | 9.99                       | 9.98                     | 7.99                                 | 4.99                                     | 2                                      |

|              |       |      |       |      |      |      |
|--------------|-------|------|-------|------|------|------|
| <b>L4-L5</b> | 14.34 | 9.64 | 11.99 | 9.59 | 6    | 2.4  |
| <b>L5-S1</b> | 14.26 | 8.6  | 11.43 | 9.14 | 5.72 | 2.29 |

With increasing disc degeneration the fibers and ligaments buckle [124]. Similar to Rohlmann et al. study, in our FE models of degenerated discs, to compensate for the change in length of the fibers and ligaments, their nonlinear force-deflection curves were offset. Therefore, when the buckled elements reached their original length, they became active.

As the disc degeneration increase, the nucleus and annulus structures become similar. The nucleus pulposus Young's modulus was increased from the healthy nucleus material values to the healthy annulus fibrosus ground substance values [124, 125]. The nucleus material properties for mild and moderate degenerated discs were linearly interpolated. Based on the previous in vitro studies [95, 98], the material properties of the annulus fibrosus ground substance were assumed to not alter with the disc degeneration. The corresponding material properties of the normal and degenerated disc components are given in Table .

Table 4.4 Material properties of the healthy and degenerated intervertebral discs.

| <b>Component/Material</b>  | <b>Element Formulation</b> | <b>Constitutive model</b>  | <b>Material parameters</b> |           |           |
|----------------------------|----------------------------|----------------------------|----------------------------|-----------|-----------|
|                            |                            |                            | <b>C1</b>                  | <b>C2</b> | <b>D1</b> |
| <b>Nucleus</b>             |                            |                            |                            |           |           |
| Nucleus/Healthy            | Hexahedral                 | Non-linear (Mooney Rivlin) | 0.12                       | 0.03      | 0.0005    |
| Nucleus/Mildly Degenerated | Hexahedral                 | Non-linear (Mooney Rivlin) | 0.135                      | 0.03375   | 0.03788   |

|                                |            |                            |        |         |         |
|--------------------------------|------------|----------------------------|--------|---------|---------|
| Nucleus/Moderately Degenerated | Hexahedral | Non-linear (Mooney Rivlin) | 0.1575 | 0.03938 | 0.09394 |
| Nucleus/Severely Degenerated   | Hexahedral | Non-linear (Mooney Rivlin) | 0.18   | 0.045   | 0.15    |
| <b>Annulus Fibrosus</b>        |            |                            |        |         |         |
| Annulus Fibrosus (Ground)      | Hexahedral | Non-linear (Neo Hookean)   | 0.348  | --      | 0.3     |
| Annulus Fibrosus (Fiber)       | Rebar      | Non-linear Hypoelastic     | --     | --      | --      |

## 4.5 Models Instrumentation

The instrumentation including pedicle screws and rods were meticulously designed in SolidWorks (Dassault Systèmes SolidWorks Corporation, Waltham, MA) software. Initially, a graphic STL file of all the models' geometry was imported into the SolidWorks. Subsequently, the graphic geometries were used to contribute in appropriate placement of pedicle screws and determining the rods contour. The complete instrumented models were then transferred to the Abaqus for modeling and analyzing.

Instrumentation included eighteen pedicle screws extending from T10 to iliac. Pedicles of T10, T11, and T12 vertebral levels were instrumented bilaterally with 4.5 mm pedicle screws with the length of 40 mm. Six 5.5 mm titanium alloy pedicle screws with the length of 45 mm were bilaterally anchored at L1, L2, and L4 pedicles. L5 and S1 pedicles were instrumented with 6.5 screws with the length of 45 mm and 55 mm, respectively. Two 8.5 mm iliac screws with the length of 80 mm were placed such that there was no screw prominence. All pedicle screws were assigned titanium alloy (Ti6Al4V) material properties (Young's Modulus (E) of 115 GPa and Poisson's ratio ( $\nu$ ) of 0.3 [170]).

COCR material properties (Young's Modulus ( $E$ ) of 241 GPa and Poisson's ratio ( $\nu$ ) of 0.3 [170]) were assigned to the two 5.5 mm rods. The pedicle screws were kinematically coupled to the pedicles of the vertebrae through bushings in all degrees of freedom. The rods were tied to the pedicle screws tulip heads. To connect the iliac screws to the rods, two connectors were bonded to the iliac screw tulip heads and rods. The connectors were assigned Ti6Al4V material properties. Figure shows the instrumented spinopelvic model with 30° of PSO at the L3 level.

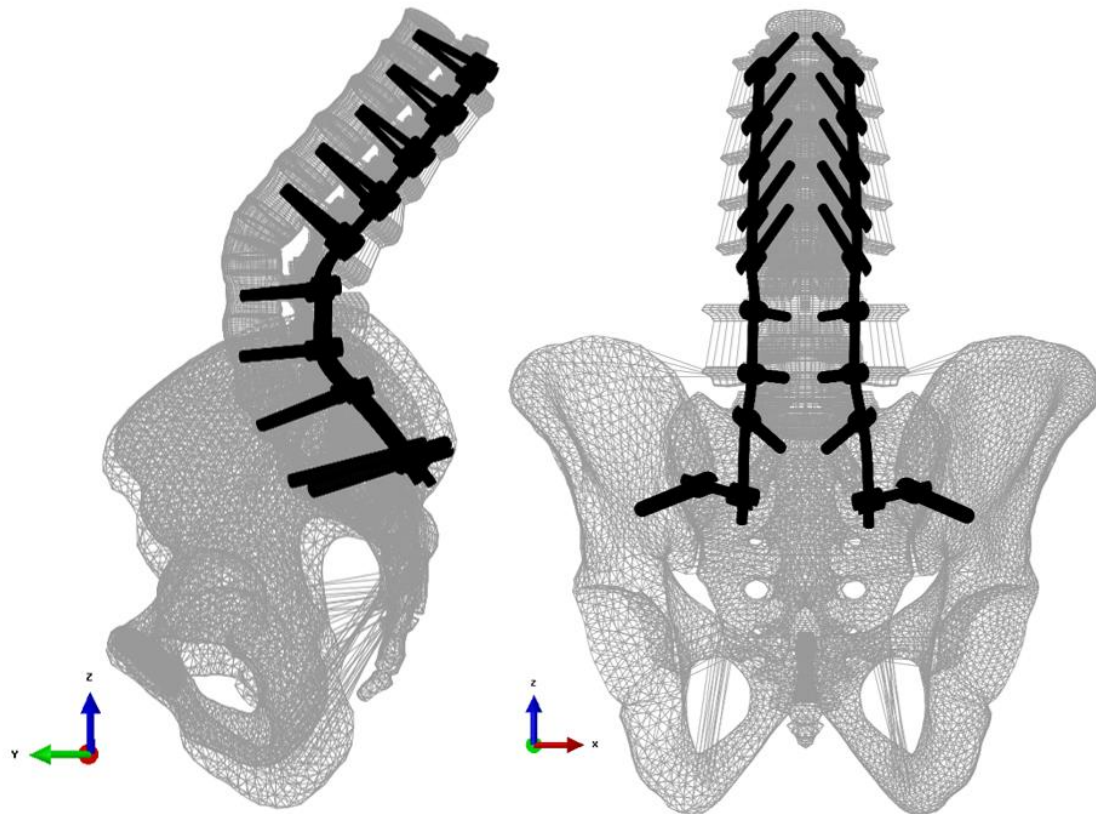


Figure 4-4 Lateral and posterior views of the instrumented spinopelvic healthy discs model treated with PSO at the L3 level. For the sake of instrumentation clarity, the spinopelvic geometry was made transparent. The instrumentations used in the model were shown in dark color.

## **4.6 FE Modeling of Alternative Instrumentation Techniques**

The high rate of rod failure following PSO has led to alterations in instrumentation strategies. This section describes the methodology of the alternative instrumentation techniques utilized following PSO. The previously PSO Instrumented FE model was utilized to study different instrumentation configurations. Various alternative techniques including the use of multiple rods, interbody cages, and cross connector were simulated. A detailed description of the simulated constructs is given below.

### **4.6.1 Multi-Rod FE Constructs**

In addition to the single bilateral rod instrumentation, 3-rod and 4-rod configurations were simulated. Multi-rod configurations included medially, laterally, and posteriorly affixed accessory rods, and the short rod technique proposed by Gupta et al. [29].

Four different models were developed for the medially affixed multi-rod constructs. In 3-rod constructs with the satellite rod affixed medially, the secondary rod was once connected to the right primary rod above L2 and below L4 pedicle screws (short) (Figure ), and in another model it was affixed to the right primary rod above L1 and below L5 pedicle screws (long) (Figure ). Similar to the 3-rod medially affixed constructs, two different short and long 4-rod constructs with the satellite rods attached medially were made (Figure and Figure ).

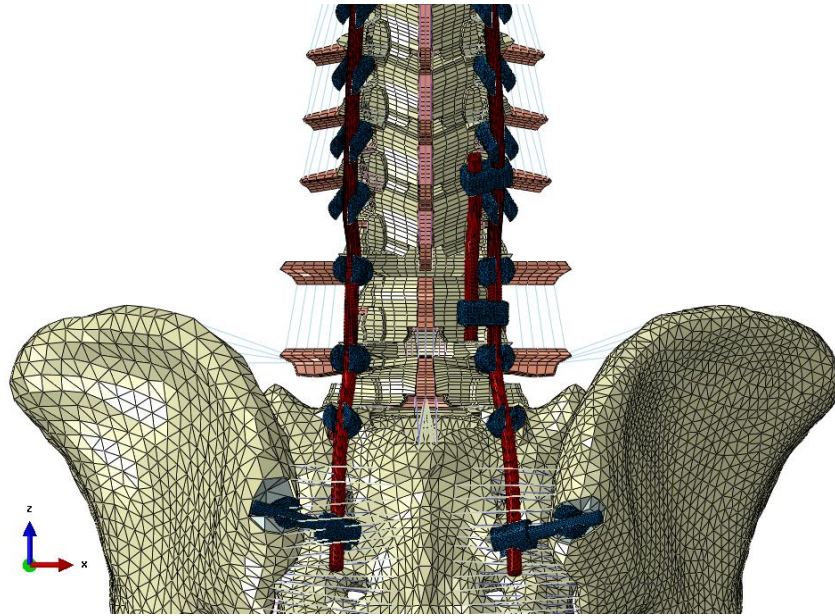


Figure 4-5 Posterior view of the instrumented PSO model using medially affixed 3-rod construct (Short). Using side-by-side cross connector, the secondary rod was connected to the right principal rod above L2 and below L4 pedicle screw levels.

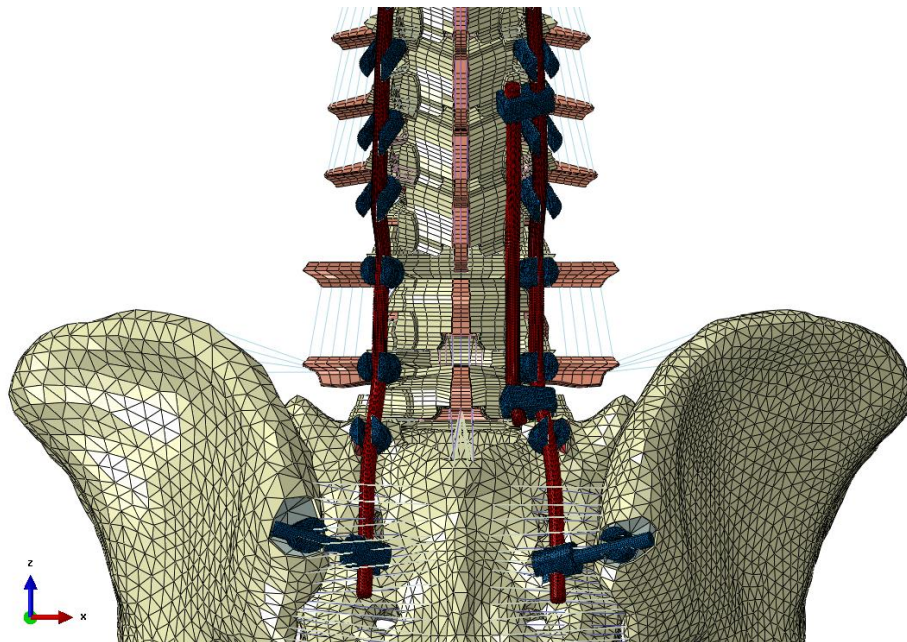


Figure 4-6 Posterior view of the instrumented PSO model using medially affixed 3-rod construct (Long). Using side-by-side cross connector, the secondary rod was connected to the right principal rod above L1 and below L5 pedicle screw levels.

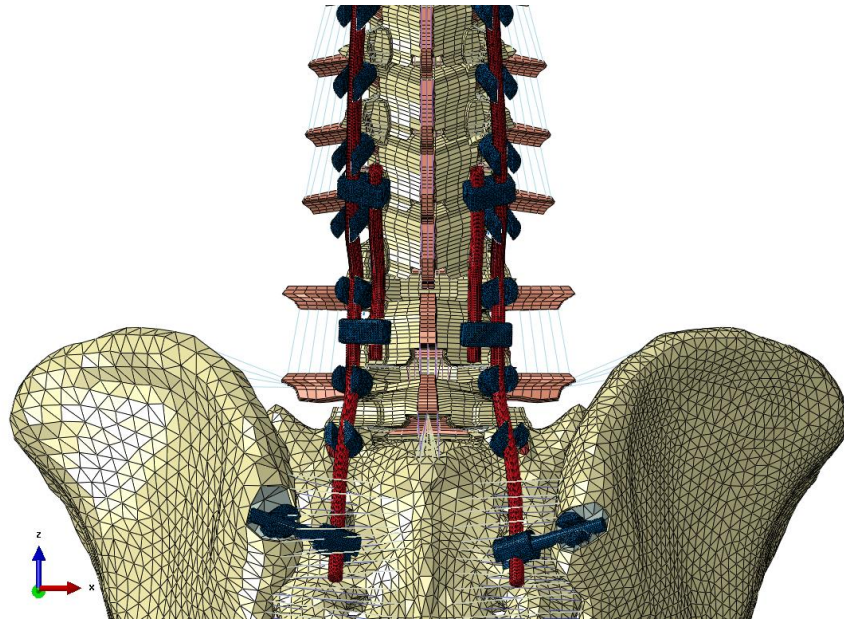


Figure 4-7 Posterior view of the instrumented PSO model using medially affixed 4-rod construct (Short). Using side-by-side cross connectors, the secondary rods were connected to the principal rods above L2 and below L4 pedicle screw levels.

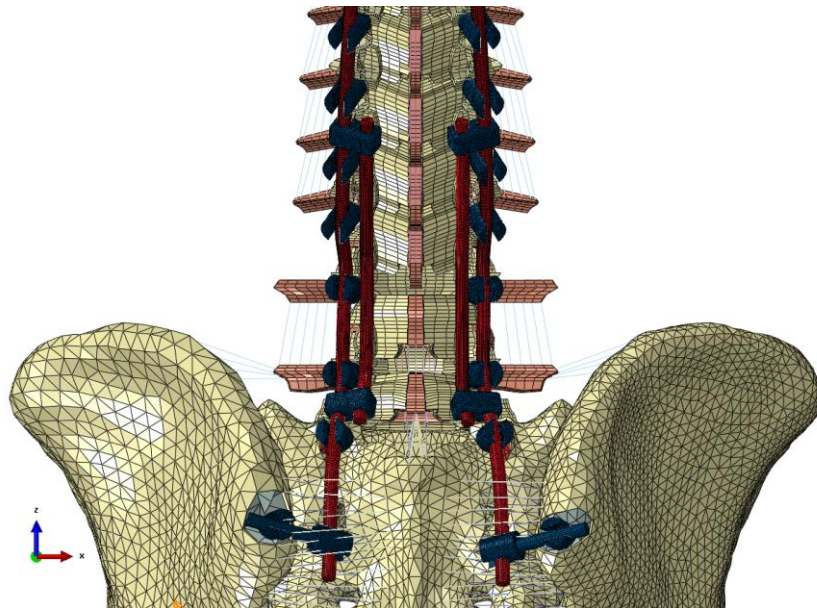


Figure 4-8 Posterior view of the instrumented PSO model using medially affixed 4-rod construct (Long). Using side-by-side cross connectors, the secondary rods were connected to the principal rods above L1 and below L5 pedicle screw levels.

Similar to the medially affixed satellite rod models, four different models were developed for the laterally affixed rod constructs. In multi-rod laterally affixed constructs, the secondary rods were once attached to the primary rods above L2 and below L4 pedicle screws (Short) (Figure and Figure ), and in the other models they were attached to the primary rods above L1 and below L5 pedicle screws (Long) (Figure and Figure ). In both medially and laterally affixed models, all the connections between the rods and side-by-side connectors were bonded using tie constraints.

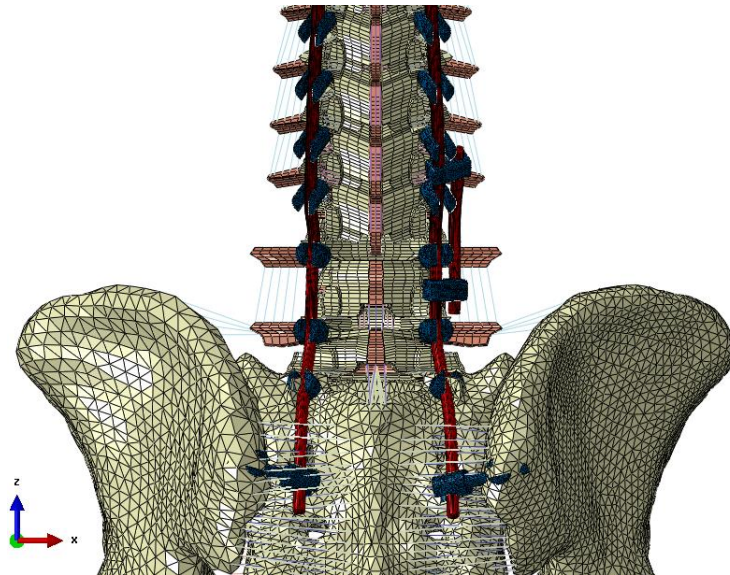


Figure 4-9 Posterior view of the instrumented PSO model using laterally affixed 3-rod construct (Short). Using side-by-side cross connector, the secondary rod was connected to the right principal rod above L2 and below L4 pedicle screw levels.

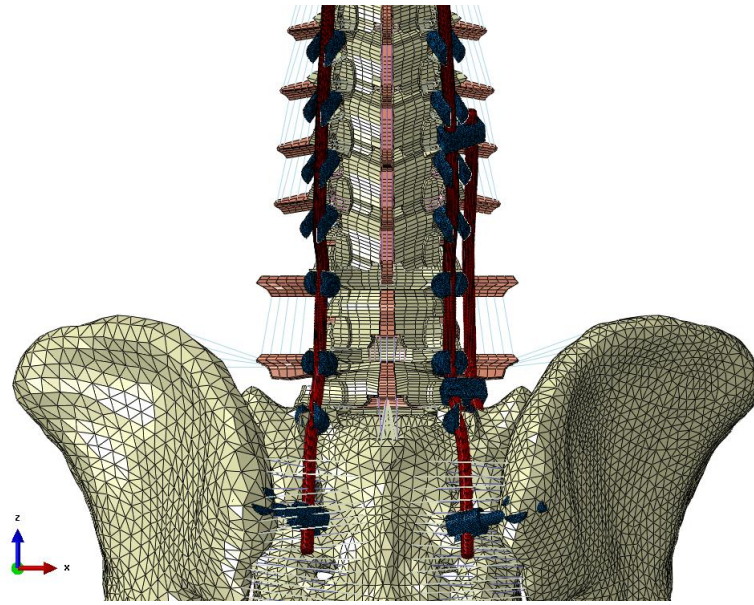


Figure 4-10 Posterior view of the instrumented PSO model using laterally affixed 3-rod construct (Long). Using side-by-side cross connector, the secondary rod was connected to the right principal rod above L1 and below L5 pedicle screw levels.

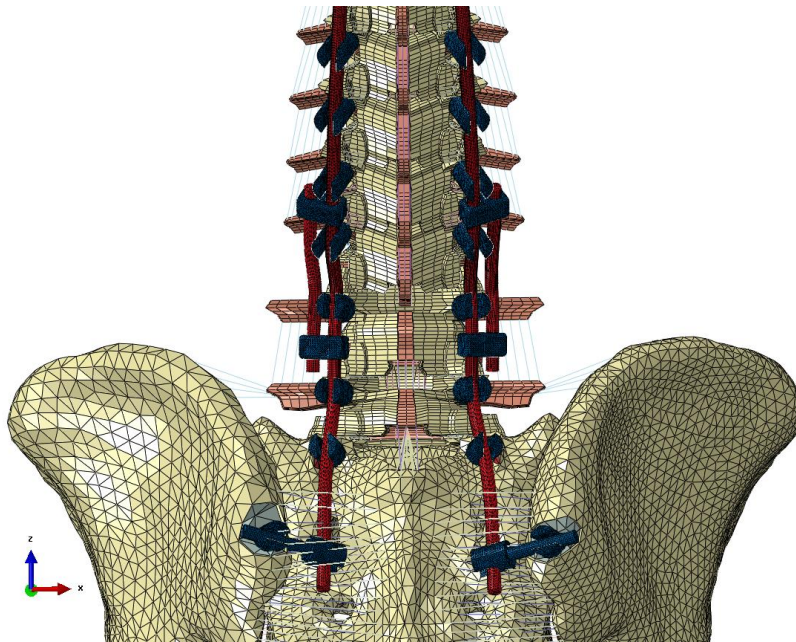


Figure 4-11 Posterior view of the instrumented PSO model using laterally affixed 4-rod construct (Short). Using side-by-side cross connectors, the secondary rods were connected to the principal rods above L2 and below L4 pedicle screw levels.

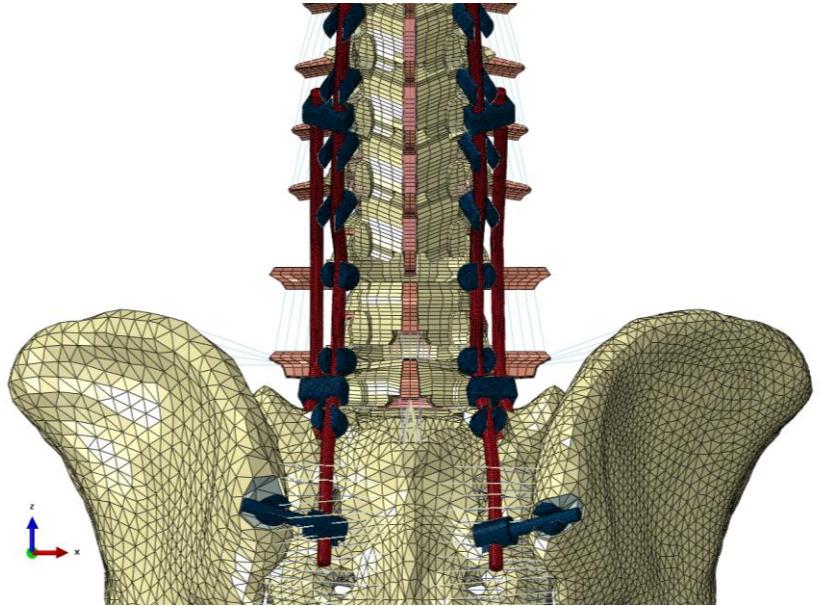


Figure 4-12 Posterior view of the instrumented PSO model using laterally affixed 4-rod construct (Long). Using side-by-side cross connectors, the secondary rods were connected to the principal rods above L1 and below L5 pedicle screw levels.

To attach the satellite rods posteriorly, a novel pedicle screw design patented by Frankel et al. was simulated [171]. In this technique, called “head-to-head” method, the setscrew of the primary pedicle screw was designed in a way that was mounted with a secondary shorter tulip. Using tie constraints, the satellite rods were attached to the secondary tulip heads. Two different models with “head-to-head” technique were made. In the first model, the pertaining novel screw design was anchored at L1 and L5 pedicles (Figure ), and in another model, they were instrumented at L1, L5, and S1 levels (Figure ).

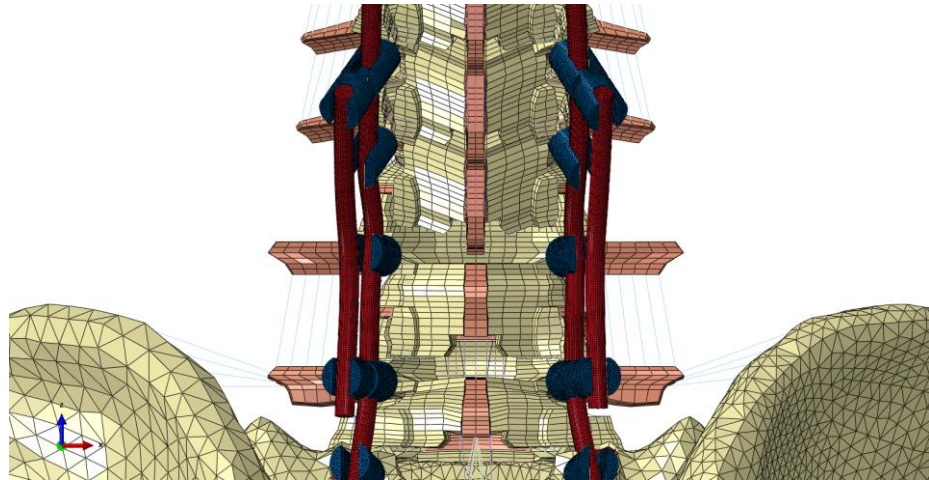


Figure 4-13 Posterior view of the instrumented PSO model using “head-to-head” dual rod technique (Short). The secondary rods were connected to the principal rods at L1 and L5 pedicle screw levels.

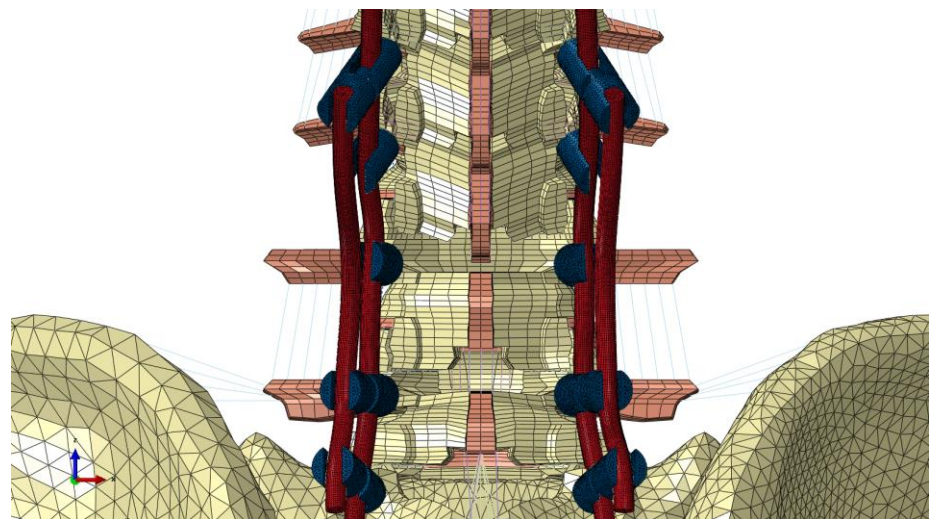


Figure 4-14 Posterior view of the instrumented PSO model using “head-to-head” dual rod technique (Long). The secondary rods were connected to the principal rods at L1, L5, and S1 screw levels.

Gupta et al. proposed a novel multi-rod technique (Short rod technique) in which the primary rods were not connected to the pedicle screws anchored adjacent to the PSO levels, while additional two short rods were spanning on the PSO level (L3) using anchors

connected to the adjacent levels. In the short rod model simulation, two principal rods were spanned from T10 to ilium without any connection to the pedicle screws immediately adjacent to the PSO (L2 and L4), while two additional shorter rods were only attached to the tulip heads immediately adjacent to the PSO (Figure ).

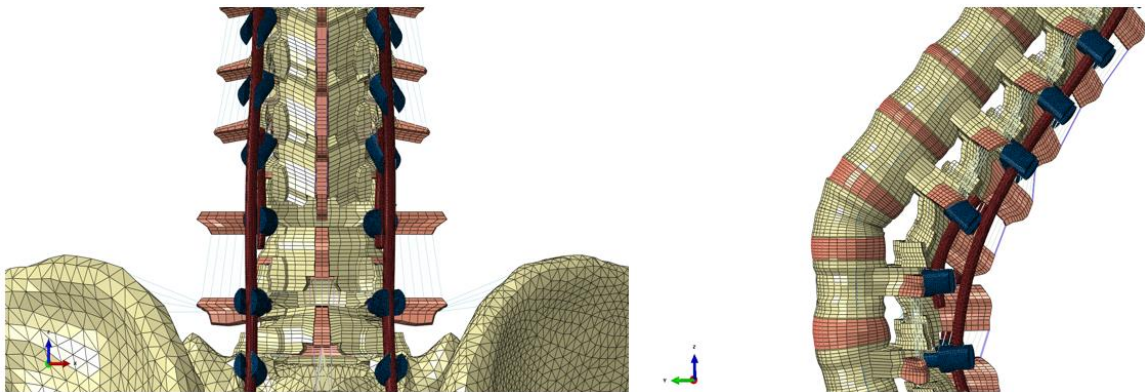


Figure 4-15 Lateral (right) and posterior (left) views of the instrumented PSO model using “short rod” technique. In this technique, the two primary rods were not connected to the pedicle screws immediately adjacent to the PSO, whereas two additional short rods were attached to the pedicle screws adjacent to the PSO. For the sake of instrumentation visualization, in the lateral view, the ilium bones were not shown.

In the above FE models, all the primary and accessory rods were assigned with COCR material properties, while the titanium alloy material properties were defined for the side-by-side connectors, accessory tulip heads, and set screws.

#### **4.6.2 Interbody Spacer FE Models**

The aforementioned instrumented PSO spinopelvic model was also supplemented with interbody spacers (Figure ). The lateral approach was used to instrument the lumbar intervertebral discs with the cages. In one case the intervertebral discs adjacent to the PSO were supplemented with two interbody spacers, and in another model, all the intervertebral

discs from L1 to S1 were instrumented using the cages. The ideal cage heights and lordosis angles for all the levels were calculated from the PSO spinopelvic FE model. Subsequently, the pertaining cages were meticulously designed in SolidWorks and imported into the Abaqus software for the instrumentation. A total nucleotomy and a partial annulotomy were performed by deleting the corresponding elements of the intervertebral discs. The tie constraints were used to simulate the intervertebral fusions. The interbody cages were assigned polyether ether ketone (PEEK) material properties ( $E=3600$ ,  $\nu=0.4$ ).

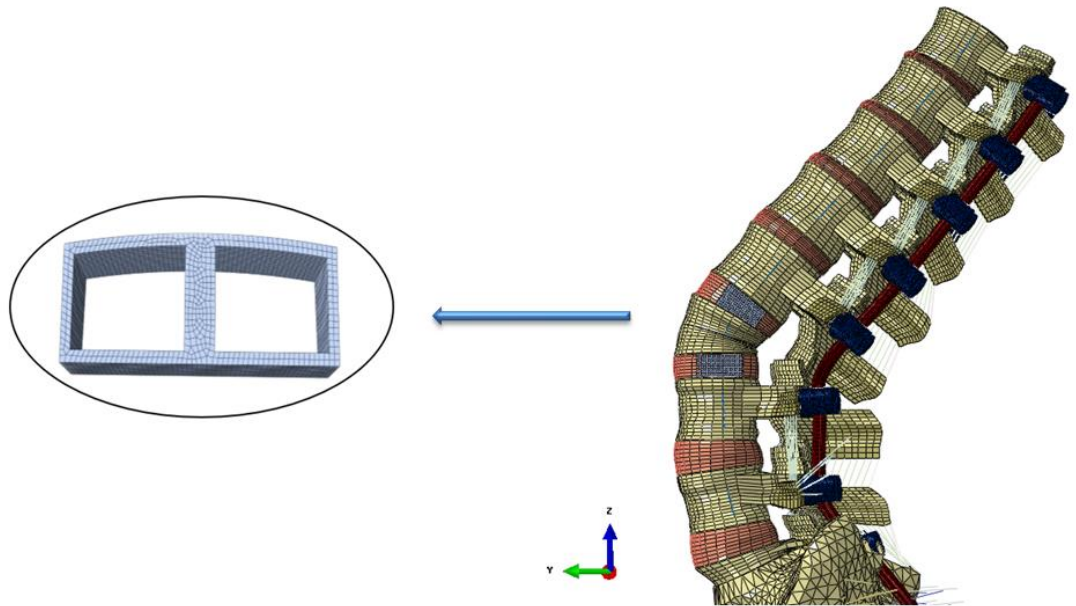


Figure 4-16 Lateral view of the instrumented spinopelvic model supplemented with interbody spacers adjacent to the PSO level (L3). On the left side, a top view of the meshed interbody spacer used in the model was demonstrated. For the sake of intervertebral discs visualization, the ilium bones were not shown in this figure.

### 4.6.3 Cross-Connector FE Models

Four different FE configurations of the cross-connectors were simulated (Figure ).

A geometry of the cross connector was accurately designed in SolidWorks and imported

to the Abaqus Software for analyzing. In the simulated instrumented PSO models, the cross-connectors were connected to the rods above (between L1 and L2 tulip heads), below (between L4 and L4 tulip heads), both above and below, and at the PSO level (between L2 and L4 tulip heads). The connection between the rods and cross-connectors were bonded using tie constraints. Ti6Al4V material properties were assigned to the cross-connectors. Figure shows the four different configurations of the cross-connector in the instrumented PSO model.

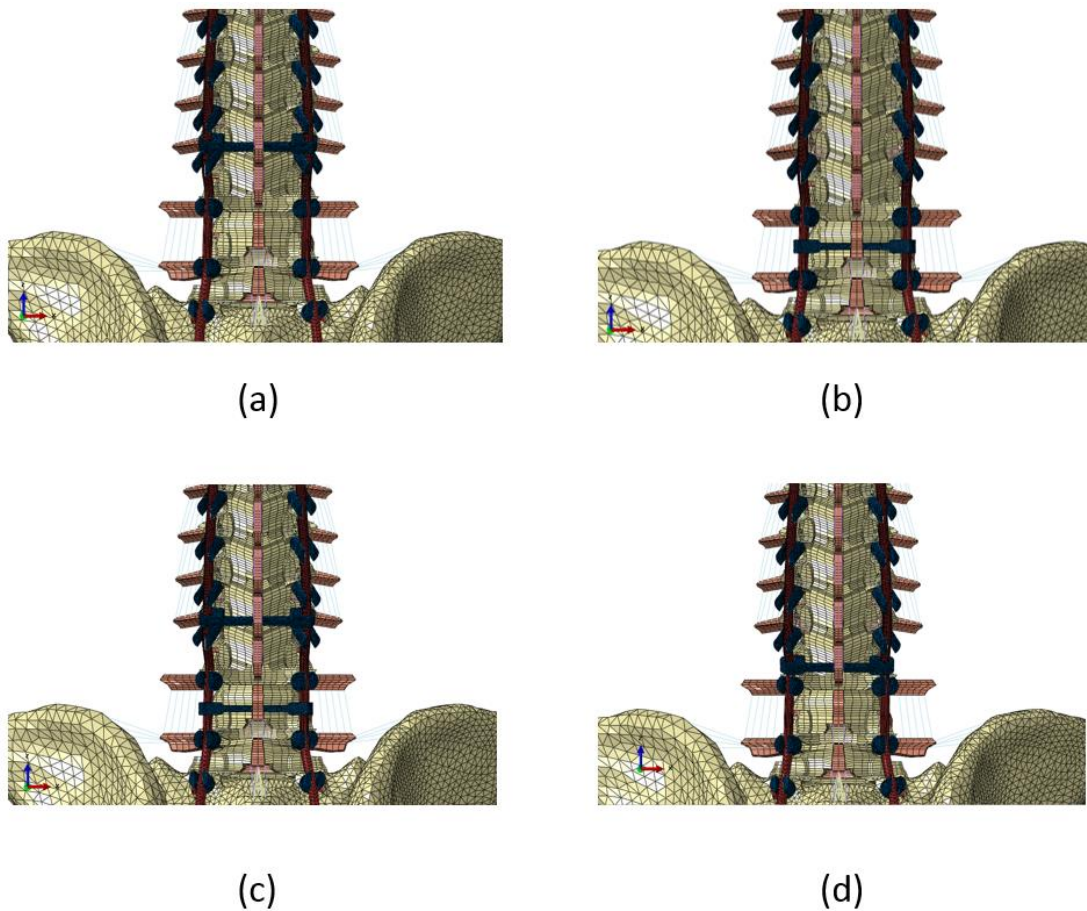


Figure 4-17 A posterior representation of four different configurations with the cross connector. (a) Cross connector located above the PSO level. (b) cross-connector located below the PSO level. (c) Cross connectors located above and below the PSO level. (d) Cross connector located at the PSO level.

## **4.7 Loading and Boundary Conditions**

The loading for the PSO spinopelvic FE models was applied in two different steps. During the simulation steps, the acetabulum surfaces of the pelvis were fixed in all degrees of freedom. In the first step, as previously published by Patwardhan et al., the follower load technique was utilized to mimic similar kinematics response as those in vivo [172]. In this step, using connector elements the follower loads of 300 N for thoracic spine and 400 N for lumbar spine were applied to the T10-pelvic model. Besides, a concentrated 400 N force was applied to the sacral base. In the second step, pure moments of 7.5 Nm were applied to a reference point above the T10 vertebral body in all the three anatomical directions of flexion (Flex), extension (Ext), right/left lateral bending (LB), and right/left axial rotation (AR). The reference point was kinematically coupled to the superior endplate of T10. The applied moments were in all directions.

## **4.8 Models Validation**

The main reason for the validation of an FE model is to ensure whether the model can predict previous experimental outcomes. Due to the lack of experimental data for the effect of PSO on the ROM, we compared the L1-S1 global ROM of our intact versus PSO models to the previous FE publications [16, 28]. Due to the severe instability of the PSO, similar to Ottardi et al., different motions of flexion, extension, lateral bending, and axial rotation were simulated using 7.5Nm, 3Nm, 4Nm, and 3Nm moments, respectively [28]. During the simulations, the inferior part of the sacrum was constrained in all directions.

The validation of the developed instrumented spinopelvic PSO model involved a comparison of this model to Deviren et al. in-vitro study [22]. Deviren and colleagues

conducted the range of motion bending tests on six instrumented specimens. In their study, the T12-S1 (excluding L3) instrumented specimens were tested before and after the PSO performance at the L3 level. These specimens were subjected to a maximum of 7.5 Nm moments in three anatomical directions of flexion-extension, right/left lateral bending, and right/left axial rotation. Similar tests were replicated in the instrumented FE models before and after the PSO simulation. In both models, a pure moment of 7.5 Nm was applied to a reference point above the upper vertebral body of T12. The point was kinematically coupled to the superior endplate of T12. The inferior part of the sacrum was constrained in all degrees of freedom.

To validate the degenerated lumbar motion segments of L1-L2, L4-L5, and L5-S1, the results of the FE models were compared to the previously published in vitro study conducted by Mimura et al. [118]. In their experimental study, they applied a maximum moment of 10 Nm to each motion segment and calculated the three-dimensional intervertebral motions of each vertebral level separately. In our study, pure moments of 10 Nm were applied to a reference point located above the proximal vertebra of each motion segment. This point was kinematically coupled to the superior endplate of the proximal vertebra. In each motion segment, the inferior endplate of the lower vertebral body was constrained in all degrees of freedom. Due to lack of data for the PSO associated with disc degeneration, we were not able to validate L2-L3 and L3-L4 motion segments.

## **4.9 Data Analysis**

The L1-S1 global ROM of the intact and PSO spinopelvic models and the L2-L4 ROM of the spinopelvic models instrumented from T12 to S1 (excluding L3) with and

without PSO were analyzed for validation purposes. To calculate the range of motion, the coordinates of the selected nodes were extracted from the output data base and imported into Excel (Microsoft Corporation, WA, USA). For flexion and extension motions, the angles within the sagittal plane were calculated. To measure the lateral bending, the motion was recorded in the coronal plane, and for axial rotation, the motion was calculated in the transverse plane. To validate the disc degenerated models, the range of motion of L1-L2, L4-L5, and L5-S1 segments with different grades of disc degeneration were assessed.

The L2-L4 global range of motion of the instrumented models with different grades of intervertebral disc degeneration were measured. Additionally, the T10-S1 global range of motion of all the instrumented spinopelvic models including different grades of intervertebral disc degeneration and various instrumentation configurations (multi-rod, interbody spacer, and cross-connectors) were calculated. For all the instrumented models, during various bending motions of flexion, extension, lateral bending, and axial rotation, the stress distribution plots were precisely evaluated. The values for the maximum von Mises stress on the rods were recorded. The magnitude of the force at the osteotomy site was recorded for entire degenerated, multi-rod, interbody, and cross-connector models.

## **5 Results**

### **5.1 Introduction**

The first step of this project was to validate the developed instrumented spinopelvic PSO model along with different disc degeneration grades. As described in the previous chapter, the range of motion data was obtained from the literature. The first section of this chapter is dedicated to the validation results of the FE models. The primary objectives of this study were to investigate the effect of lumbar disc height alteration due to degeneration and alternative instrumentation configurations on the rods following PSO. The second section in this chapter proceeds with the analyses of results from different disc degeneration models. Finally, the results of alternative instrumentation configurations are presented.

### **5.2 Validation Results**

For the validation of the PSO model, the trend of the L1-S1 global range of motion of the intact and PSO models was compared to the previous computational studies [16, 28]. Similar to the Ottardi et al. study, following 500N follower load application the flexion, extension, lateral bending and axial rotation motions were simulated using 7.5Nm, 3Nm, 4Nm, and 3Nm moments, respectively [28]. After PSO at L3, the L1-S1 flexion, extension, and axial rotation motions increased by 47%, 36%, and 57%, while the lateral bending

decreased by 25%. L1-S1 global ROM for the intact and PSO models during different loading cases is shown in Figure .

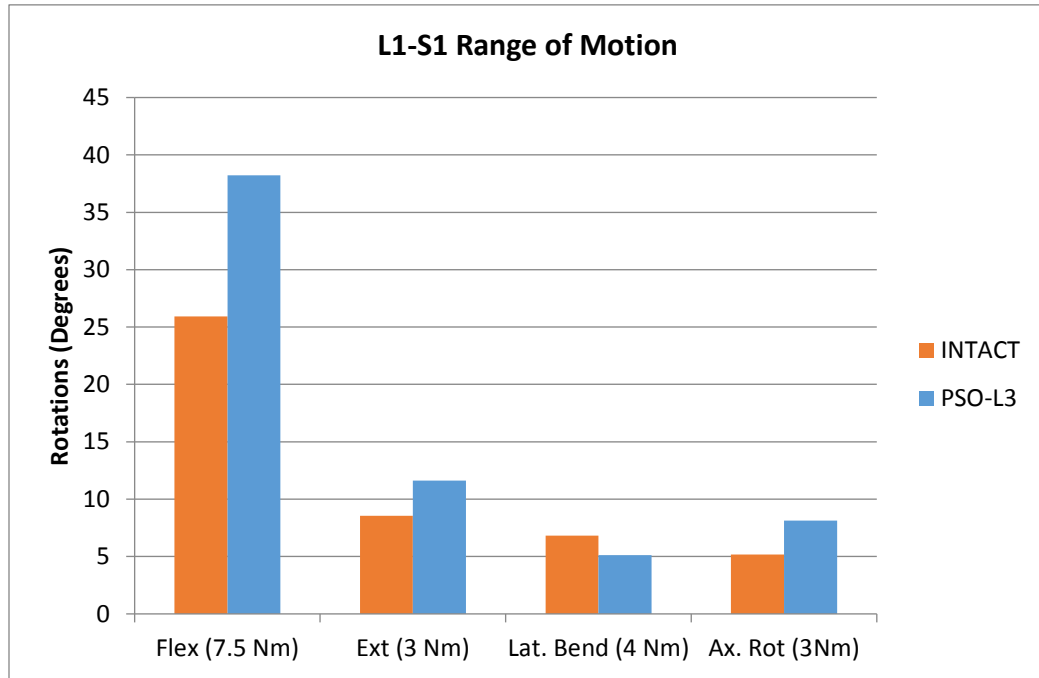


Figure 5-1 L1-S1 global ROM for the intact and PSO (at L3) FE models during during different loading cases.

For the validation of the instrumented PSO model, the range of motion predictions for T12-S1 (excluding L3) instrumented spinopelvic model before and after PSO inclusion were compared to Deviren et al. in vitro data. For this validation, the L2-L4 range of motion was considered. FE models predictions for flexion/extension and lateral bending motions fell within one standard deviation. For the axial rotation motion, by performing PSO, the same decreasing trend was observed. Figure shows the comparison between the current FE results with the Deviren et al. experimental study.

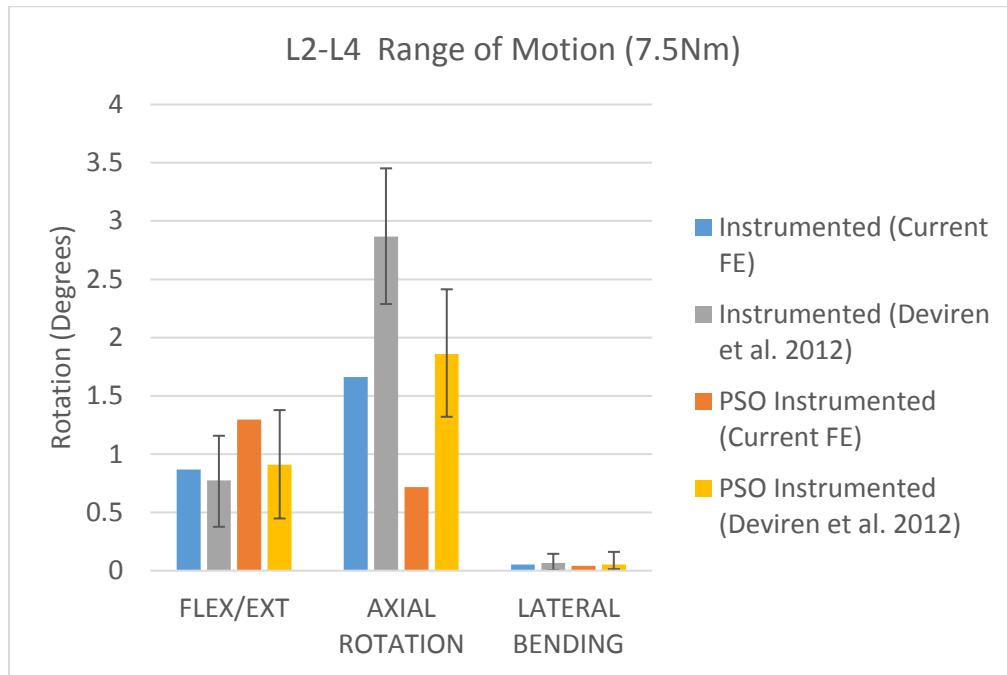


Figure 5-2 L2-L4 range of motion comparison of the instrumented FE models (before and after PSO performance) with experimental data at 7.5Nm.

To validate the developed disc degenerated FE models, only the range of motion for L1-L2, L4-L5, and L5-S1 motion segments were compared to the previously published Mimura et al. in vitro study (Figure , Figure , Figure ). Mimura et al. found that with the increase in disc degeneration the range of motion in flexion/extension and lateral bending decreased while in axial rotation initially increased then with the severe degeneration decreased. Our finite element model predicts the same trends of intersegmental rotations for different motion segments of L1-L2, L4-L5, and, L5-S1. For lateral bending our measured ranges of motion were significantly lower than those determined by Mimura et

al., however, the values for the healthy IVDs were previously validated using cadaver studies [32].

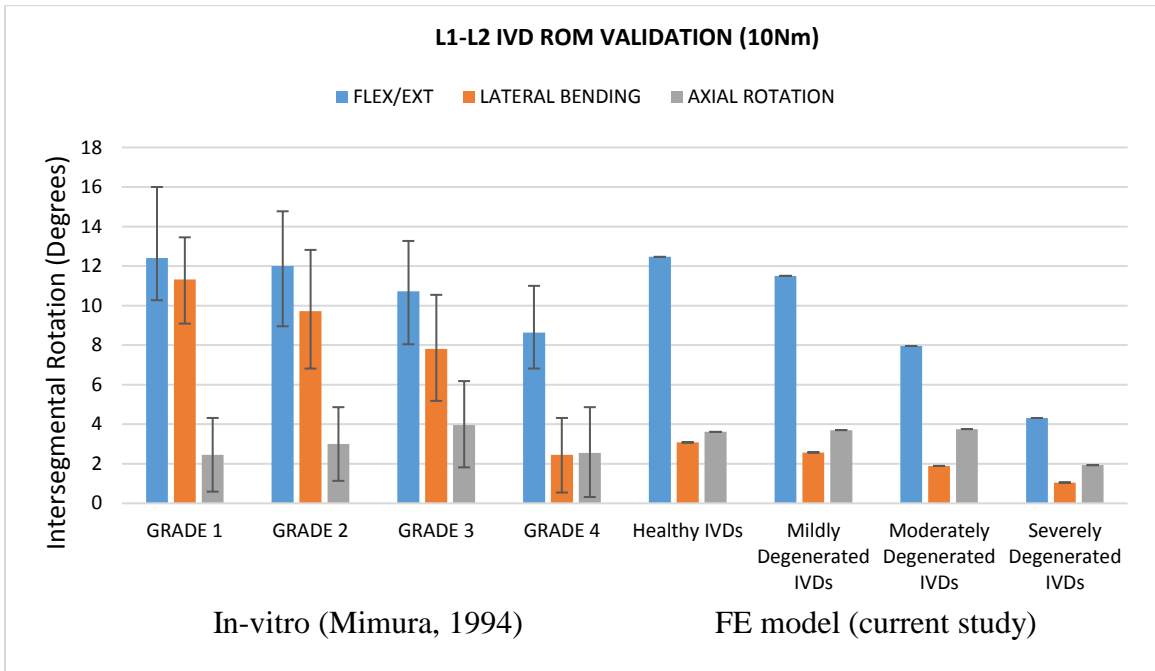


Figure 5-3 Comparison of ROMs of developed degenerated L1-L2 motion segments models to results from Mimura et al. study in flexion/extension, lateral bending, and axial rotation under 10 Nm moments.

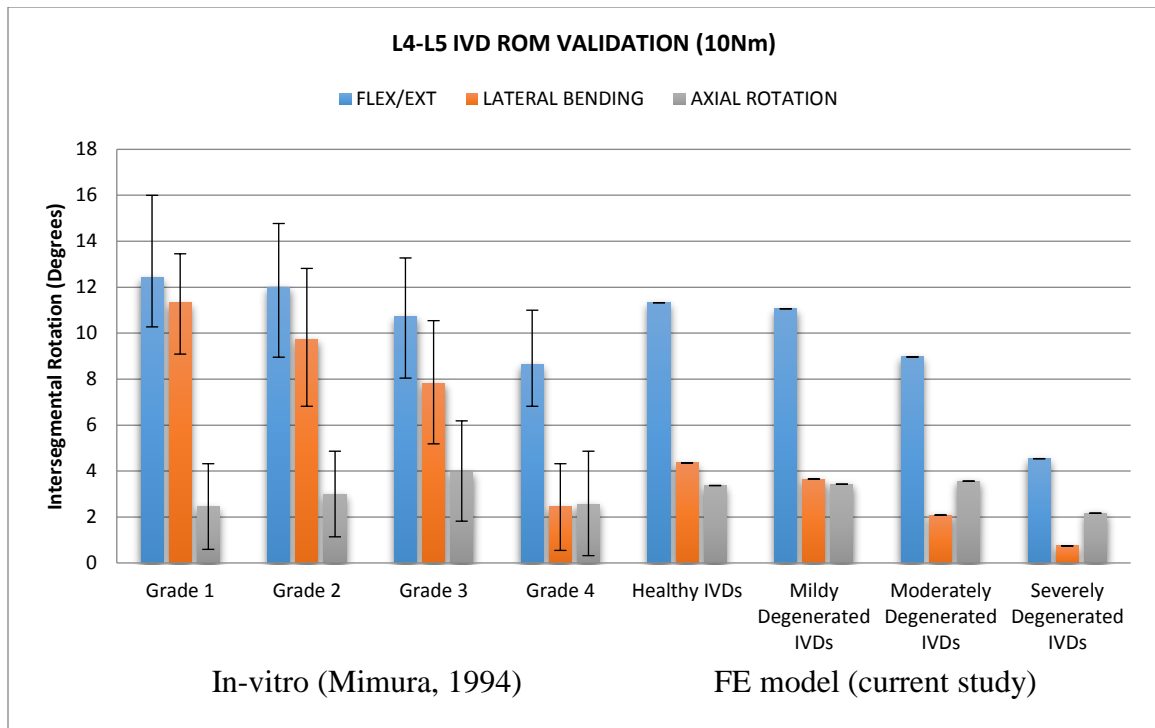


Figure 5-4 Comparison of ROMs of developed degenerated L4-L5 motion segments models to results from Mimura et al. study in flexion/extension, lateral bending, and axial rotation under 10 Nm moments.

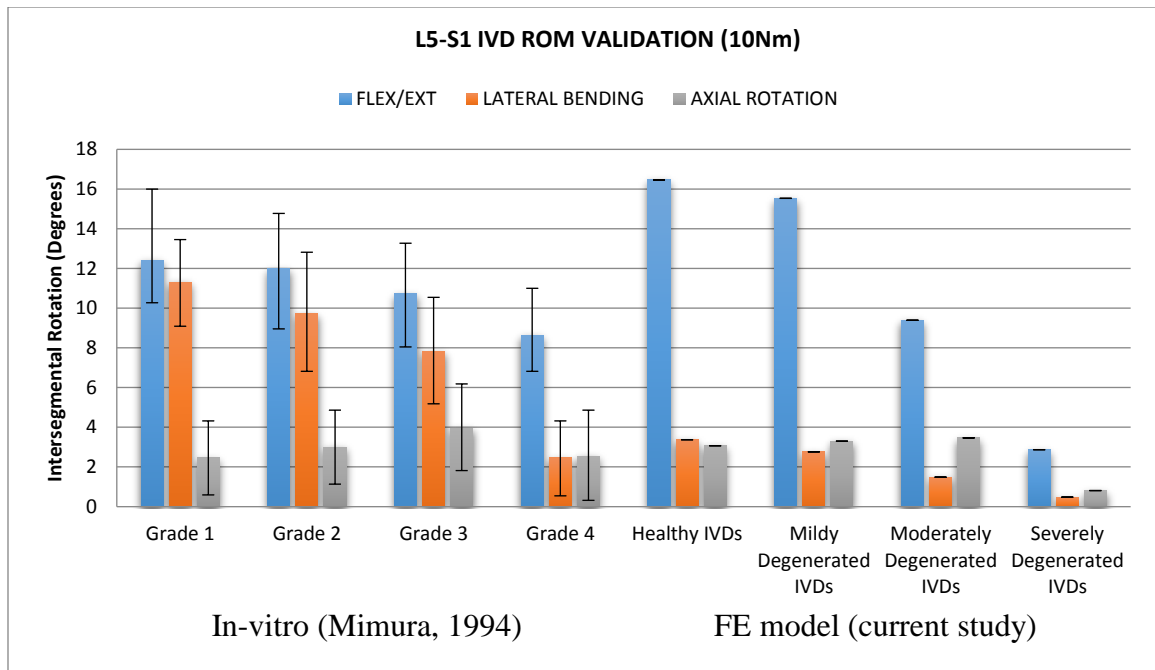


Figure 5-5 Comparison of ROMs of developed degenerated L5-S1 motion segments models to results from Mimura et al. study in flexion/extension, lateral bending, and axial rotation under 10 Nm moments.

In general, the developed instrumented PSO FE models with different grades of IVD degeneration were in good agreement with the rotations reported by the experimental studies.

## 5.3 Results of IVD Geometry Effects on the Rods Following PSO

### 5.3.1 Range of Motion Results

In brief, T10-pelvis PSO model along with the three mildly, moderately, and severely degenerated PSO models were instrumented via pedicle screws. Ranges of motions of different instrumented degenerated FE models were predicted with the existence of the follower loads and under moments of 7.5Nm.

With increasing in the disc degeneration, the L2-L4 global range of motion decreased in all loading cases of flexion, extension, lateral bending, and axial rotation. Compared to the healthy disc model, the mildly, moderately, and severely degenerated disc models showed 16%, 35%, and 54% reduction in flexion motion, respectively. In lateral bending the L2-L4 motion reduction of about 12%, 34%, and 60% was recorded with an increase in the disc degeneration grade. Compared to the healthy discs, with an increase in the disc degeneration, the L2-L4 axial rotation motion decreased about 5% (Mildly degenerated), 21% (Moderately degenerated), and 34% (Severely degenerated). Figure represents the T10-S1 global ROM of the instrumented PSO models with different grades of IVDs.

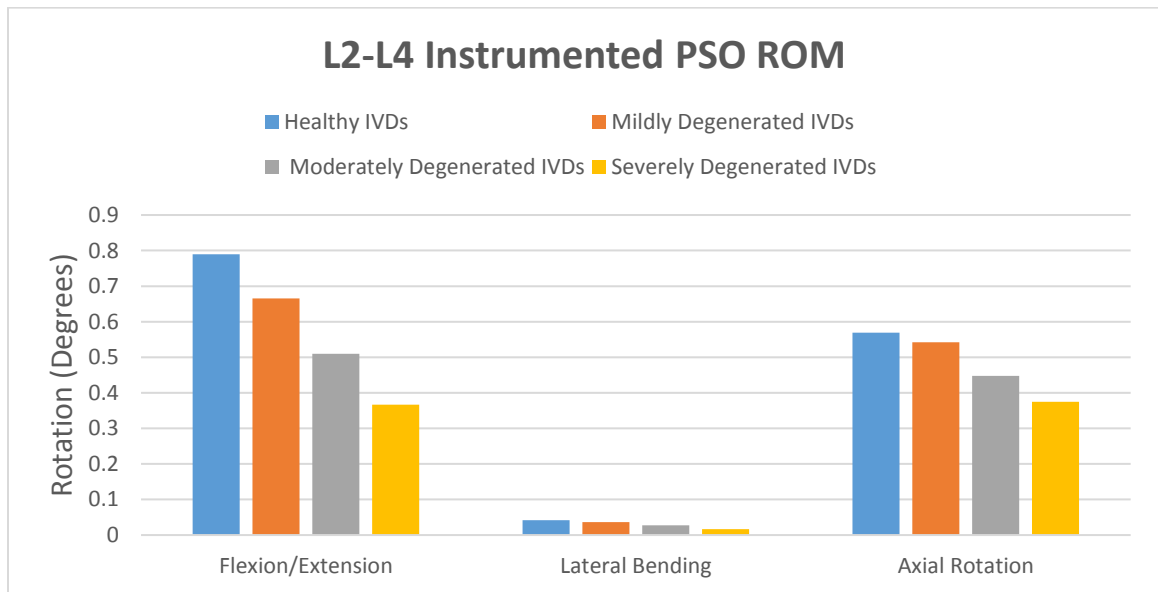


Figure 5-6 Instrumented L2-L4 Global ROM for different loading cases and different grades of disc degeneration.

With increasing in the disc degeneration, the largest variation in the T10-S1 global range of motion was found in flexion/extension motion. Comparing to the healthy IVD instrumented model, the mildly, moderately, and severely degenerated IVD instrumented models indicated approximately 10%, 26%, and 40% decrease in flexion/extension motion, respectively. Overall, in lateral bending and axial rotation with different grades of disc degeneration similar motions were observed. Comparing to the healthy discs, the maximum variation in the axial rotation range of motion was related to the severely degenerated discs in which about 8% reduction in motion was recorded. Figure represents the T10-S1 global ROM of the instrumented PSO models with different grades of IVDs.

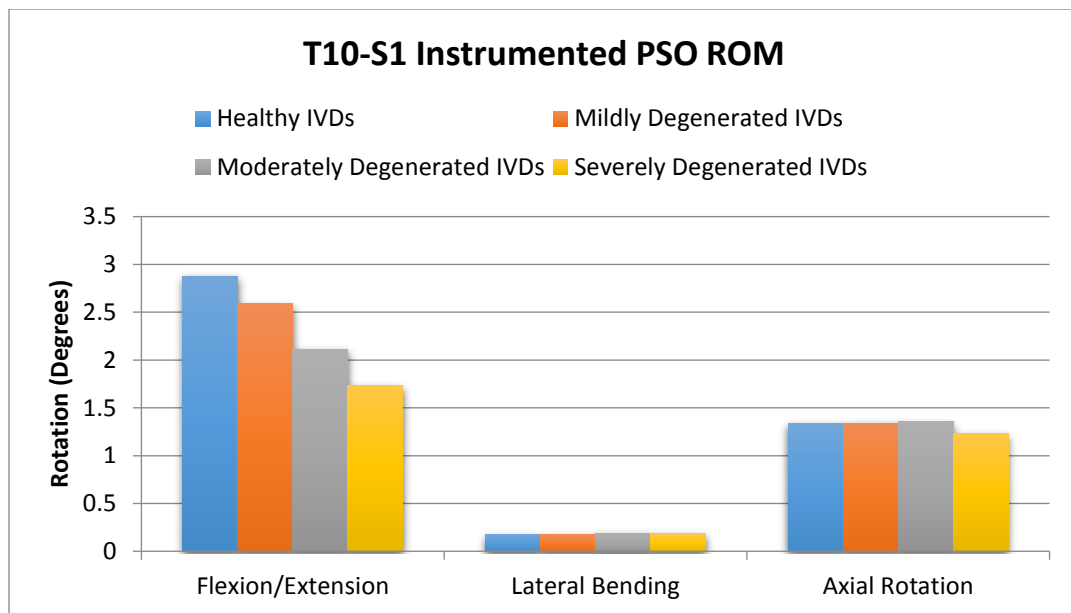


Figure 5-7 Instrumented T10-S1 Global ROM for different loading cases and different grades of disc degeneration.

### 5.3.2 Von Mises Stress Results

During different loading cases, the maximum von Mises stress on the rods was recorded. In all the models, the maximum von Mises stress on the rods occurred in the flexion motion. In the healthy IVD PSO model, the location of the maximum von Mises stress in different motions was at or adjacent to the PSO region. Overall, by increasing in the disc degeneration, the maximum von Mises stress values on the rods decreased. With different grades of IVD, in the left bending and left rotation motions the maximum von Mises stress was located at the PSO region and on the right rod, and in the right bending and right rotation motions, this value was located at the similar region on the left rod. Table shows the values and locations of the recorded maximum von Mises stress on the rods in different loading cases and different grades of disc degeneration.

Table 5.1 Maximum von Mises stress values and locations recorded on the rods in different motions and different grades of IVD degeneration.

|             | HEALTHY DISC       |                 | MILDLY DEGENERATED` |                 | MODERATELY DEGENERATED |                 | SEVERELY DEGENERATED |                 |
|-------------|--------------------|-----------------|---------------------|-----------------|------------------------|-----------------|----------------------|-----------------|
|             | Stress Value (MPa) | location        | Stress Value (MPa)  | location        | Stress Value (MPa)     | location        | Stress Value (MPa)   | location        |
| <b>FLEX</b> | 339                | PSO             | 321                 | PSO             | 267                    | PSO             | 224                  | PSO             |
| <b>EXT</b>  | 105                | L4-L5           | 90                  | L4-L5           | 81                     | S1-Iliac Screw  | 86                   | S1-Iliac Screw  |
| <b>LB</b>   | 221                | PSO (right rod) | 214                 | PSO (right rod) | 184                    | PSO (right rod) | 150                  | PSO (right rod) |
| <b>RB</b>   | 221                | PSO (left rod)  | 201                 | PSO (left rod)  | 187                    | PSO (left rod)  | 157                  | PSO (left rod)  |

|           |     |                 |     |                 |     |                 |     |                 |
|-----------|-----|-----------------|-----|-----------------|-----|-----------------|-----|-----------------|
| <b>LR</b> | 256 | PSO (right rod) | 240 | PSO (right rod) | 195 | PSO (right rod) | 170 | PSO (right rod) |
| <b>RR</b> | 256 | PSO (left rod)  | 227 | PSO (left rod)  | 197 | PSO (left rod)  | 174 | PSO (left rod)  |

### 5.3.3 Force Results

The load magnitude at the osteotomy site was measured for different constructs immediately after follower load application. With increasing in the disc degeneration, the magnitude of the load at the PSO site decreased. The measured force at this site for the healthy, mildly, moderately, and severely discs degenerated models were 248N, 257.1N, 272.1N, and 287.5N, respectively.

## 5.4 Results of Multi-Rod FE Constructs

### 5.4.1 Range of Motion Results

The PSO instrumented spinopelvic model was used to develop further multi-rod constructs. The T10-S1 global range of motion in different loading scenarios and multi-rod constructs were recorded.

Overall, medially affixed multi-rod constructs decreased flexion, extension, and left/right rotation motions. In lateral bending similar motions were observed within all the medially affixed multi-rod constructs. Comparing to the 2-rod construct, the 3-rod medially affixed short construct showed approximately 9% decrease in flexion and extension motions, and about 4% reduction in axial rotation. The 3-rod medially affixed long construct caused approximately 10%, 11%, and 6% reduction in flexion, extension, and axial rotation motions, respectively. Adding two satellite rods medially, decreased the

flexion, extension, and lateral bending by 15%, 16%, and 8%, respectively. Using two longer satellite rods decreased the ROM in flexion by 19%, in extension by 20%, and in axial rotation by 11%. The comparison of the instrumented T10-S1 global ROM for different medially affixed multi-rod constructs was shown in Figure .

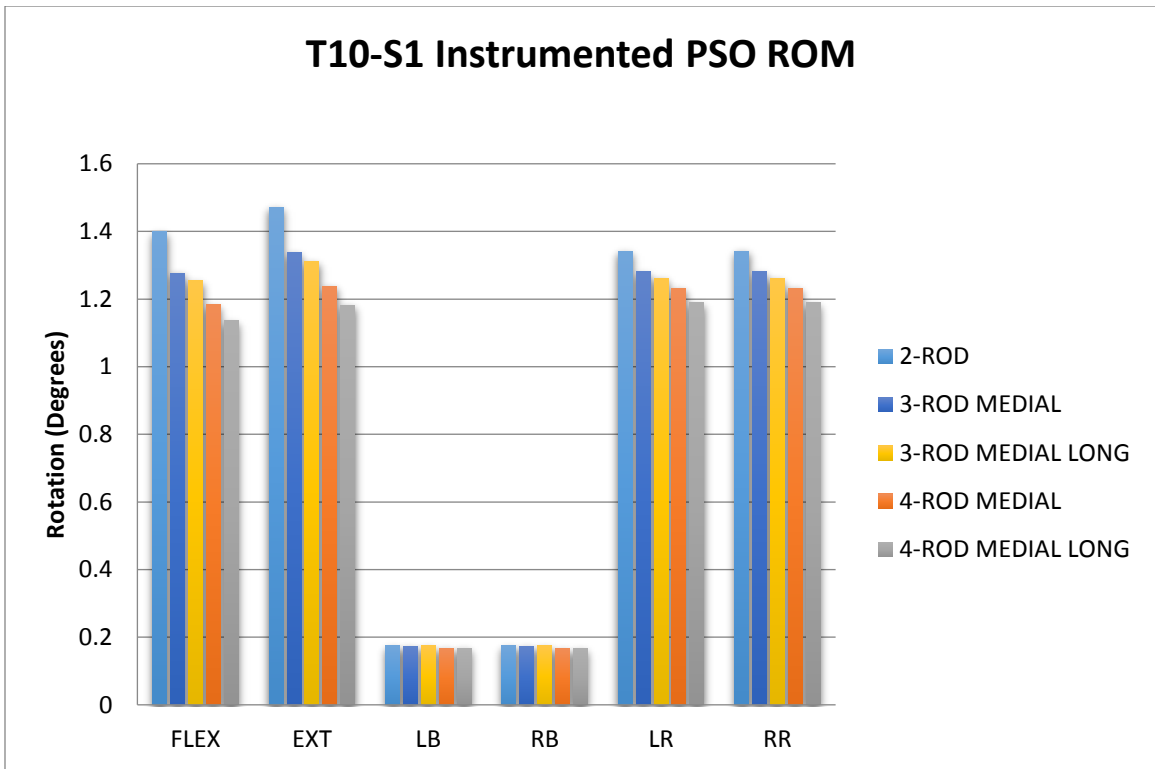


Figure 5-8 Comparison of the instrumented T10-S1 global ROM for different loading cases and different medially affixed multi-rod constructs.

Comparing to the 2-rod construct, in the laterally affixed multi-rod constructs, a similar trend of motion reduction was observed. 3-rod construct laterally affixed with short satellite rods decreased the flexion, extension, and axial rotation motions by about 6%, 7%, and 3%, respectively. Compared to the 2-rod construct, using a long laterally affixed 3-rod

construct reduced the flexion and extension by 8% and axial rotation by 5%. 4-rod laterally affixed configuration decreased the flexion by 11%, extension by 12% and axial rotation by 6%. In the 4-rod long laterally affixed construct, these reductions in flexion, extension, and axial rotation were about 14%, 15%, and 10%, respectively. The comparison of the instrumented T10-S1 global ROM for different laterally affixed multi-rod constructs was shown in Figure .

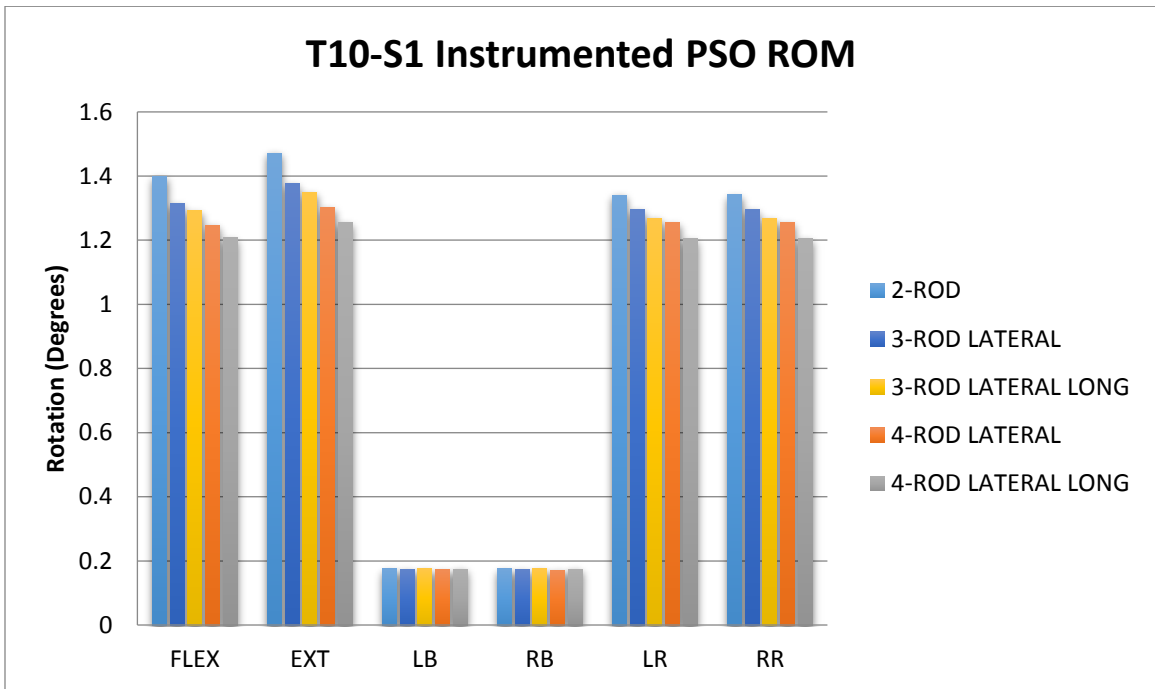


Figure 5-9 Comparison of the instrumented T10-S1 global ROM for different loading cases and different laterally affixed multi-rod constructs.

In the posteriorly affixed multi-rod constructs, the motions in all directions decreased noticeably. Adding two short accessory rods posteriorly with the head-to-head technique at the PSO region reduced flexion and extension by 36%, lateral bending by 17%, and axial rotation by 10%. With the same technique and having longer rods with one

more connection between the rods and the pedicle screws at the S1 anchors, the flexion, extension, lateral bending, and axial rotation motions declined by 42%, 43%, 21%, and 12%, respectively.

The Comparison of the instrumented T10-S1 global ROM for different loading cases and the two posteriorly affixed multi-rod constructs is given in Figure .

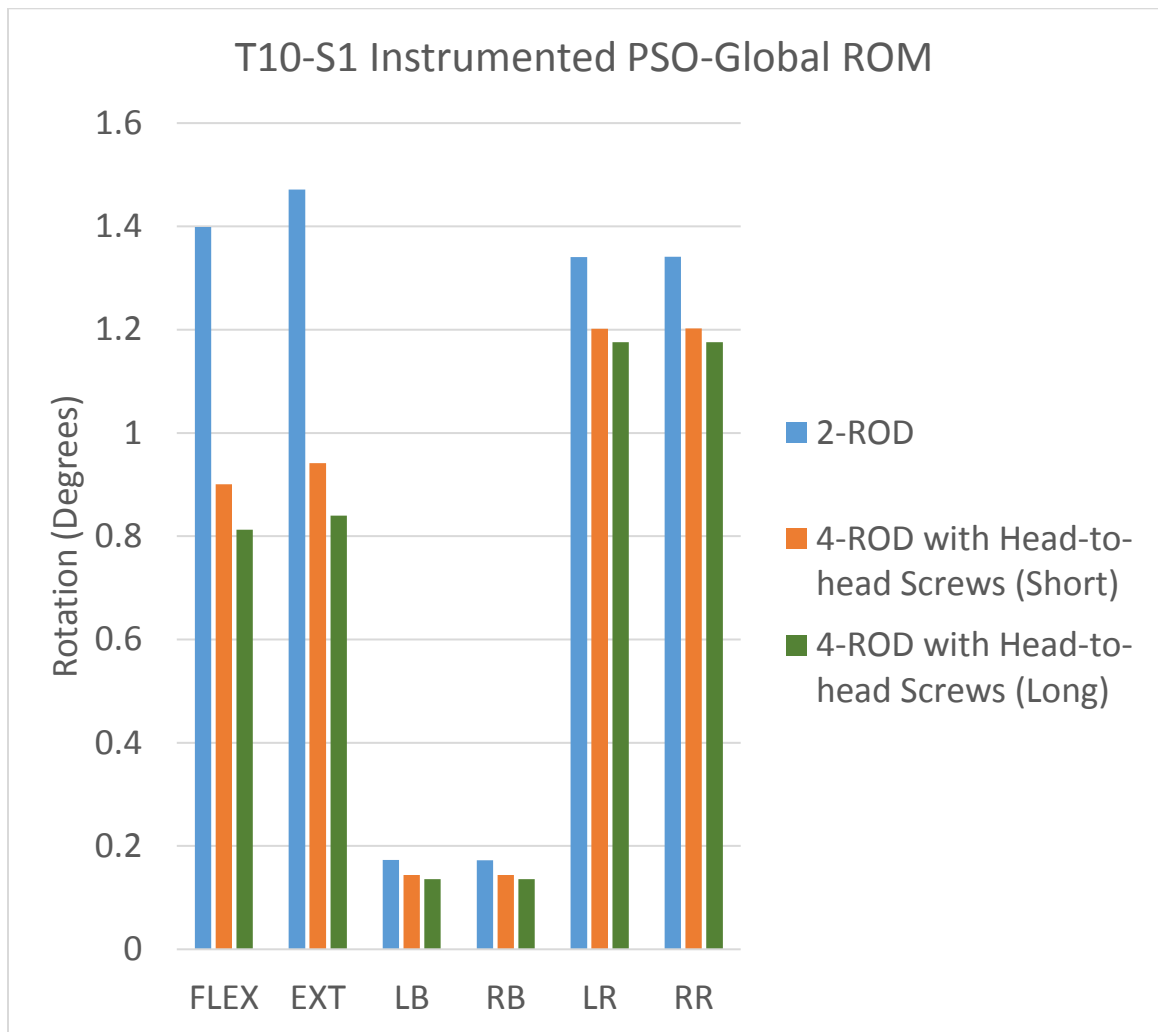


Figure 5-10 Comparison of the instrumented T10-S1 global ROM for different loading cases and different posteriorly affixed multi-rod constructs.

Compared to the 2-rod construct, the use of short-rod technique resulted in 11%, 4%, and 49% reduction in T10-S1 flexion, extension, and lateral bending motions, respectively, while the axial rotation motion increased by about 31%. A comparison of the instrumented T10-S1 global range of motion in different motions between the 2-rod and short-rod constructs is given in Figure .

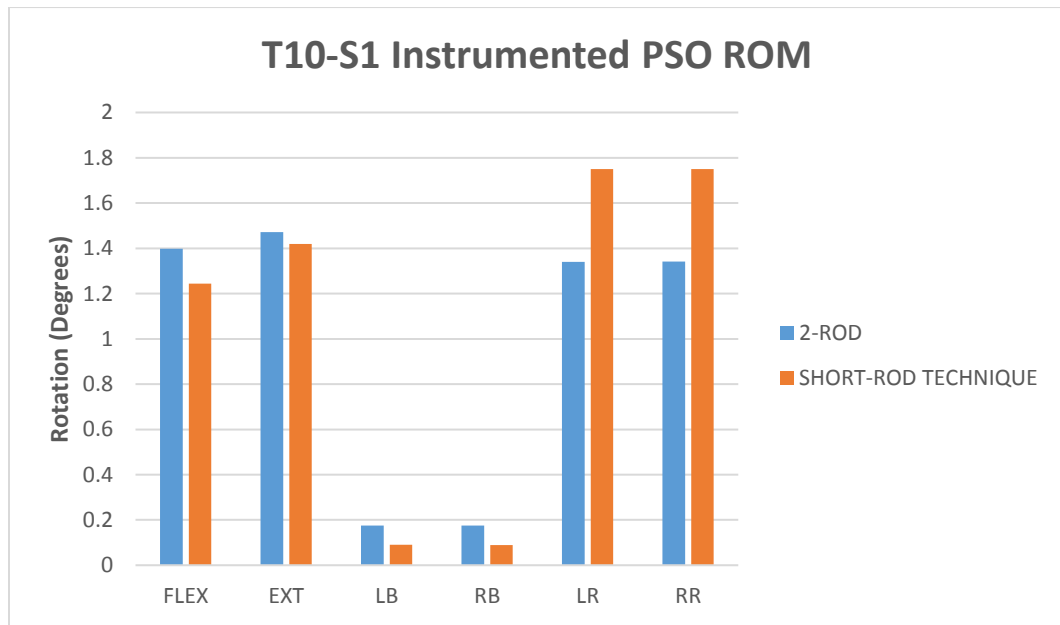


Figure 5-11 Comparison of the instrumented T10-S1 global ROM for different loading cases between the 2-rod and short-rod constructs.

## 5.4.2 Von Mises Stress Results

### 5.4.2.1 Maximum Von Mises Stress Results at the PSO Region

In general, by adding satellite rods in all the motions, magnitudes of the maximum von Mises stress at the PSO region on the rods decreased significantly. In all the multi-rod constructs (except short rod technique) the maximum von Mises stress on the rods was

found during the flexion motion. Using shorter satellite rods in all the configurations caused a greater maximum von Mises stress reduction at the PSO region in the flexion motion. In all the medially affixed multi-rod constructs, during different motions (except right bending in 3-rod constructs), the maximum von Mises stress recorded at the PSO region was greater in the satellite rods than the primary rods. However, in all the laterally affixed multi-rod constructs this value at the PSO region was greater on the primary rods than the accessory rods. At the PSO region, during all the loading directions the maximum von Mises stress in all the posteriorly affixed constructs (Except head-to-head technique during extension) occurred on the satellite rods. Compared to the two-rod construct, use of short-rod technique caused to reduce the maximum von Mises stress values at the PSO region in all the loading cases. At the PSO region, compared to the 2-rod construct, using of short-rod technique reduced the maximum von Mises stress by 48% in flexion. Compared to the same construct, adding a third short rod medially, caused a decrease of 22% in maximum von Mises stress at the PSO region during flexion, while using a longer rod reduced this value at the same region by approximately 13%. In the 4-rod medially affixed short and long accessory rods, the maximum von Mises stress at the PSO during the flexion motion decreased by 34% and 21%, respectively. In flexion motion 3-rod lateral short, 3-rod lateral long, 4-rod lateral short, and 4-rod lateral long constructs reduced the maximum von Mises stress recorded at the PSO region by 10%, 9%, 22%, and 21%, respectively. The maximum von Mises stress values and the locations on the rods at the PSO region in different constructs were given in Table , Table , Table , and Table .

Table 5.2 Maximum von Mises stress values and locations recorded on the rods at the PSO region during different loading cases in the two-rod and short-rod constructs.

|             | <b>TWO-ROD</b>     |           | <b>SHORT-ROD TECHNIQUE</b> |                                |
|-------------|--------------------|-----------|----------------------------|--------------------------------|
|             | Stress Value (MPa) | location  | Stress Value (MPa)         | location                       |
| <b>FLEX</b> | 339                | Both rods | 176                        | All rods                       |
| <b>EXT</b>  | 73                 | Both rods | 72                         | Short rods                     |
| <b>LB</b>   | 221                | RR        | 129                        | All rods except left long rod  |
| <b>RB</b>   | 221                | LR        | 134                        | All rods except right long rod |
| <b>LR</b>   | 256                | RR        | 227                        | Long rods                      |
| <b>RR</b>   | 256                | LR        | 226                        | Long rods                      |

Table 5.3 Maximum von Mises stress values and locations recorded on the rods at the PSO region in different motions and different medially affixed satellite rod constructs.

|             | <b>3-ROD MEDIAL (SHORT)</b> |                | <b>3-ROD MEDIAL (LONG)</b> |                | <b>4-ROD MEDIAL (SHORT)</b> |                       | <b>4-ROD MEDIAL (LONG)</b> |                       |
|-------------|-----------------------------|----------------|----------------------------|----------------|-----------------------------|-----------------------|----------------------------|-----------------------|
|             | Stress Value (MPa)          | location       | Stress Value (MPa)         | location       | Stress Value (MPa)          | location              | Stress Value (MPa)         | location              |
| <b>FLEX</b> | 264                         | RR (satellite) | 296                        | RR (satellite) | 225                         | Both rods (satellite) | 267                        | Both rods (satellite) |
| <b>EXT</b>  | 54                          | RR (satellite) | 69                         | RR (satellite) | 44                          | Both rods (satellite) | 60                         | Both rods (satellite) |
| <b>LB</b>   | 182                         | RR (satellite) | 198                        | RR (satellite) | 162                         | RR (satellite)        | 168                        | RR (satellite)        |
| <b>RB</b>   | 180                         | LR (Primary)   | 173                        | LR (Primary)   | 167                         | LR (satellite)        | 188                        | LR (satellite)        |

|           |     |                   |     |                   |     |                   |     |                   |
|-----------|-----|-------------------|-----|-------------------|-----|-------------------|-----|-------------------|
| <b>LR</b> | 176 | RR<br>(satellite) | 202 | RR<br>(satellite) | 153 | RR<br>(satellite) | 170 | RR<br>(satellite) |
| <b>RR</b> | 207 | LR<br>(Primary)   | 202 | LR<br>(Primary)   | 151 | LR<br>(satellite) | 188 | LR<br>(satellite) |

Table 5.4 Maximum von Mises stress values and locations recorded on the rods at the PSO region in different motions and different laterally affixed satellite rod constructs.

|             | <b>3-ROD LATERAL (SHORT)</b> |              | <b>3-ROD LATERAL (LONG)</b> |              | <b>4-ROD LATERAL (SHORT)</b> |                     | <b>4-ROD LATERAL (LONG)</b> |                     |
|-------------|------------------------------|--------------|-----------------------------|--------------|------------------------------|---------------------|-----------------------------|---------------------|
|             | Stress Value (MPa)           | location     | Stress Value (MPa)          | location     | Stress Value (MPa)           | location            | Stress Value (MPa)          | location            |
| <b>FLEX</b> | 304                          | RR (primary) | 308                         | RR (primary) | 263                          | Both rods (primary) | 268                         | Both rods (primary) |
| <b>EXT</b>  | 54                           | RR (primary) | 52                          | RR (primary) | 45                           | Both rods (primary) | 50                          | Both rods (primary) |
| <b>LB</b>   | 202                          | RR (primary) | 199                         | RR (primary) | 180                          | RR (primary)        | 177                         | RR (primary)        |
| <b>RB</b>   | 189                          | LR (primary) | 191                         | LR (primary) | 175                          | LR (primary)        | 173                         | LR (primary)        |
| <b>LR</b>   | 221                          | RR (primary) | 232                         | RR (primary) | 194                          | RR (primary)        | 205                         | RR (primary)        |
| <b>RR</b>   | 218                          | LR (primary) | 220                         | LR (primary) | 190                          | LR (primary)        | 202                         | LR (primary)        |

Table 5.5 Maximum von Mises stress values and locations recorded on the rods at the PSO region in different motions and different posteriorly affixed satellite rod constructs.

|             | <b>4-ROD HEAD-TO-HEAD (SHORT)</b> |                       | <b>4-ROD HEAD-TO-HEAD (LONG)</b> |                       |
|-------------|-----------------------------------|-----------------------|----------------------------------|-----------------------|
|             | Stress Value (MPa)                | location              | Stress Value (MPa)               | location              |
| <b>FLEX</b> | 196                               | Both rods (satellite) | 217                              | Both rods (satellite) |

|            |     |                     |     |                     |
|------------|-----|---------------------|-----|---------------------|
| <b>EXT</b> | 74  | Both rods (primary) | 79  | Both rods (primary) |
| <b>LB</b>  | 154 | RR (satellite)      | 172 | RR (satellite)      |
| <b>RB</b>  | 150 | LR (satellite)      | 161 | LR (satellite)      |
| <b>LR</b>  | 153 | RR (satellite)      | 173 | RR (satellite)      |
| <b>RR</b>  | 148 | LR (satellite)      | 161 | LR (satellite)      |

#### 5.4.2.2 Maximum Von Mises Stress Results on the Rods

In the 3-rod medially affixed construct with short satellite rod connected to the right primary rod, in all the motions except left rotation the location of the maximum von Mises stress on the rods was below the distal domino, while in the left rotation it was found above the proximal connector. Adding the third rod on the right side of the spine caused greater stress value in right bending than left bending and left rotation than right rotation. The value of the maximum von Mises stress recorded for this construct was similar to the value recorded on the rods in the 2-rod construct.

In the 3-rod medially affixed construct with the longer satellite rod, during flexion and left bending motions the maximum von Mises stress occurred at the PSO region of the accessory rod. In extension, right bending, and left rotation motions the location of the maximum von Mises stress was adjacent to the connector on the primary rod. Given that the satellite rod was attached to the right primary rod, in right rotation, the maximum stress happened at the PSO region of the left primary rod.

In the medially affixed 4-rod construct with short satellite rods, the location of the maximum von Mises stress was on the primary rods and adjacent to the side-by-side connectors. Overall, for this construct, the maximum von Mises stress values recorded for different loading cases were lower than the 2-rod construct.

Similar to the 4-rod construct medially affixed with short accessory rods, in the 4-rod construct medially affixed with long satellite rods, the location of maximum von Mises stress was on the primary rod and adjacent to the connectors. At the PSO region, in all the loadings the stress values were greater on the satellite rods than the primary ones. During flexion motion, a maximum von Mises stress of about 267 MPa at both locations of PSO on the satellite rods and below the distal dominos were recorded. Among all the medially affixed multi-rod constructs, the 4-rod medially affixed construct with longer accessory rods showed the lowest value of the maximum von Mises stress during the flexion motion. Figure shows the von Mises stress contour on the instrumentation during flexion in 4-rod medially affixed satellite rod constructs. Table shows the values and locations of the recorded maximum von Mises stress on the rods in different loading cases and different medially affixed satellite rod constructs.

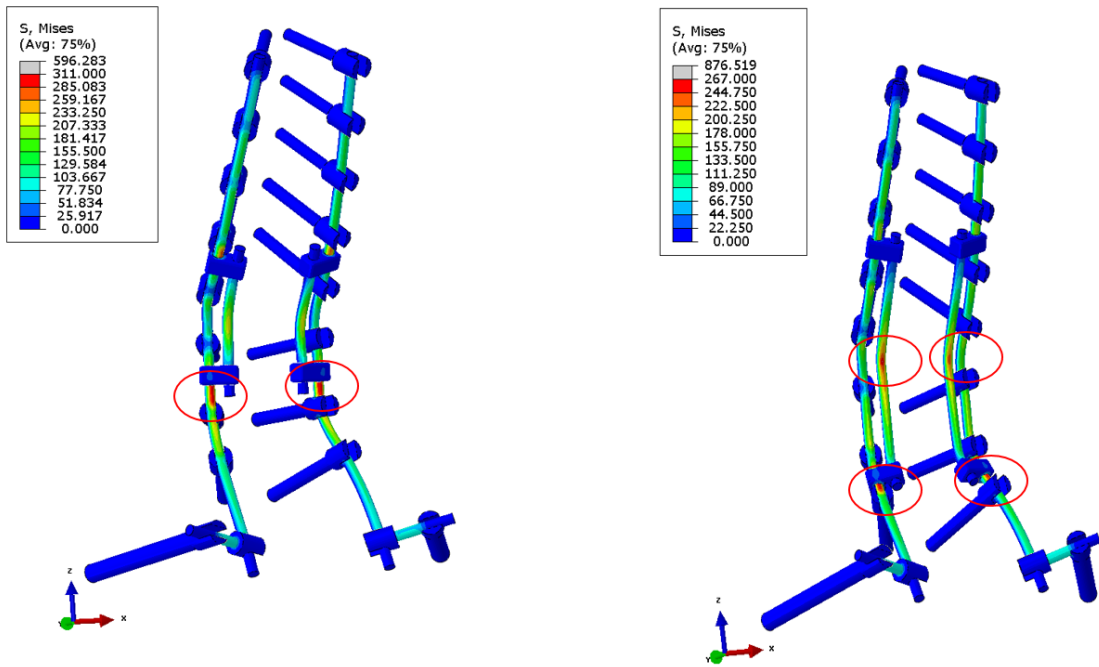


Figure 5-12 The von Mises stress contour on the instrumentation during flexion in 4-rod medially affixed short satellite rod (Left) and 4-rod medially affixed long satellite rod (Right) constructs. The red oval shapes show the location of the maximum von Mises stress on the rods.

Table 5.6 Maximum von Mises stress values and locations recorded on the rods in different motions and different medially affixed satellite rod constructs.

|             | <b>3-ROD<br/>MEDIAL<br/>(SHORT)</b> |                       | <b>3-ROD<br/>MEDIAL<br/>(LONG)</b> |                       | <b>4-ROD<br/>MEDIAL<br/>(SHORT)</b> |                       | <b>4-ROD<br/>MEDIAL<br/>(LONG)</b> |   |
|-------------|-------------------------------------|-----------------------|------------------------------------|-----------------------|-------------------------------------|-----------------------|------------------------------------|---|
|             | Stress Value (MPa)                  | location              | Stress Value (MPa)                 | location              | Stress Value (MPa)                  | location              | Stress Value (MPa)                 | location                                    |
| <b>FLEX</b> | 343                                 | Adjacent to Connector | 296                                | PSO (satellite rod)   | 311                                 | Adjacent to Connector | 267                                | Adjacent to Connector + PSO (satellite rod) |
| <b>EXT</b>  | 109                                 | Adjacent to Connector | 114                                | Adjacent to Connector | 103                                 | Adjacent to Connector | 114                                | Adjacent to Connector                       |

|           |     |                                |     |                        |     |                       |     |                       |
|-----------|-----|--------------------------------|-----|------------------------|-----|-----------------------|-----|-----------------------|
| <b>LB</b> | 229 | Adjacent to Connector          | 198 | PSO (satellite rod)    | 214 | Adjacent to Connector | 232 | Adjacent to Connector |
| <b>RB</b> | 237 | Adjacent to Connector          | 237 | Adjacent to Connector  | 214 | Adjacent to Connector | 225 | Adjacent to Connector |
| <b>LR</b> | 286 | Adjacent to Proximal Connector | 216 | Adjacent to Connector  | 260 | Adjacent to Connector | 198 | Adjacent to Connector |
| <b>RR</b> | 227 | Adjacent to Connector          | 202 | PSO (left primary rod) | 256 | Adjacent to Connector | 207 | Adjacent to Connector |

Similar to the 3-rod construct affixed medially with a short satellite rod, in the 3-rod laterally affixed construct with a short satellite rod the maximum von Mises stress occurred adjacent to the side-by-side connectors. For this construct, the recorded maximum von Mises stress values in different motions were greater than the 3-rod short medially affixed construct. The maximum von Mises stress recorded on the rods in this construct was about 4% greater than what was recorded for the 2-rod construct. Given that satellite rod was attached to the right primary rod, the maximum von Mises stress value on the right primary rod was greater in right bending and left rotation than in left bending and right rotation, respectively.

In the 3-rod construct affixed laterally with the longer satellite rod, during flexion and left bending the maximum von Mises stress occurred at the PSO region of the primary rod connected to the satellite rod. In extension, right bending, and left rotation the location of the maximum von Mises stress was adjacent to the connector on the primary rod. Given that satellite rod was attached to the right primary rod, in right rotation motion, the maximum stress occurred at the PSO region of the left primary rod.

Similar to the 4-rod construct affixed medially with short satellite rods, in the 4-rod construct affixed laterally with short accessory rods, the location of the maximum von Mises stress was on the primary rods and adjacent to the side-by-side connectors. In general, for this construct, the maximum von Mises stress values recorded in different loading cases were greater than the 4-rod construct affixed medially with short satellite rods.

In the 4-rod construct affixed laterally with long satellite rods, the maximum von Mises stress was on the primary rod and adjacent to the connectors. At the PSO region, in all the loadings the stress values were greater on the primary rods than the satellite rods. During flexion motion, the maximum von Mises stress of about 274 MPa at both locations of PSO on the primary rods and below the distal side-by-side connectors were recorded. Among all the laterally affixed multi-rod constructs, the 4-rod construct affixed laterally with longer accessory rods showed the lowest value of the maximum von Mises stress during the flexion motion. Figure shows the von Mises stress contour on the instrumentation during flexion in 4-rod laterally affixed satellite rod constructs. Table shows the values and locations of the recorded maximum von Mises stress on the rods in different loading cases and different laterally affixed satellite rod constructs.

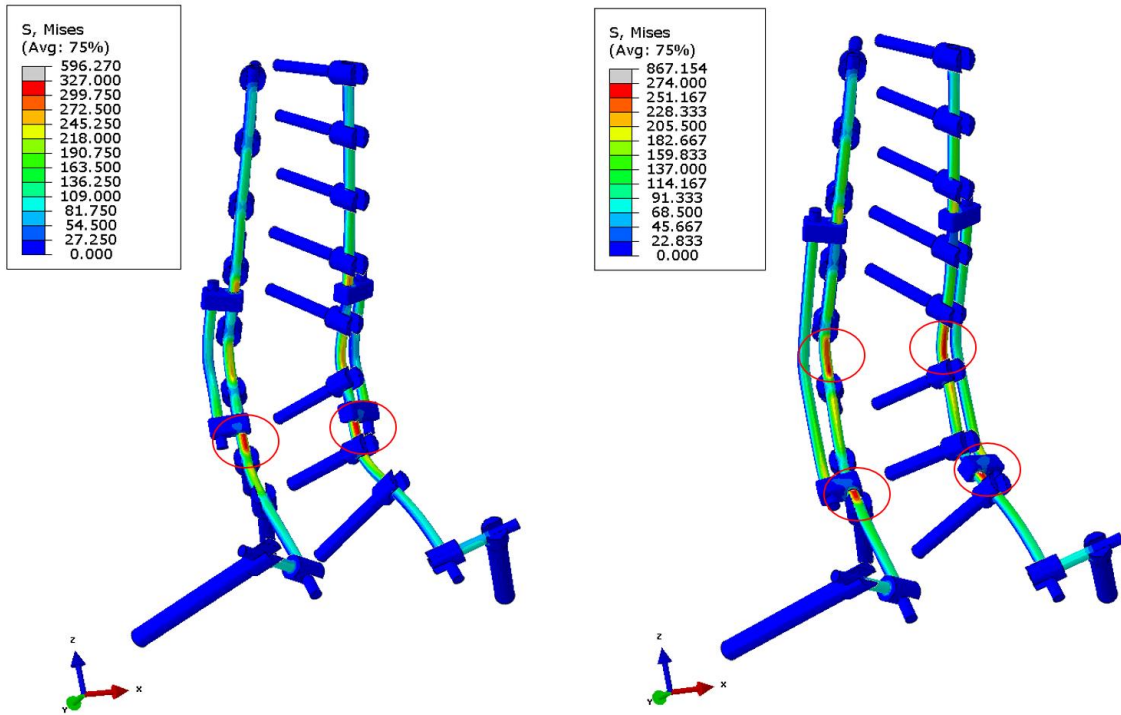


Figure 5-13 The von Mises stress contour on the instrumentation during flexion in 4-rod laterally affixed short satellite rod (Left) and 4-rod laterally affixed long satellite rod (Right) constructs. The red oval shapes show the location of the maximum von Mises stress on the rods.

Table 5.7 Maximum von Mises stress values and locations recorded on the rods in different motions and different laterally affixed satellite rod constructs.

|             | 3-ROD LATERAL (SHORT) |                       | 3-ROD LATERAL (LONG) |                       | 4-ROD LATERAL (SHORT) |                       | 4-ROD LATERAL (LONG) |   |
|-------------|-----------------------|-----------------------|----------------------|-----------------------|-----------------------|-----------------------|----------------------|---|
|             | Stress Value (MPa)    | location              | Stress Value (MPa)   | location              | Stress Value (MPa)    | location              | Stress Value (MPa)   | location                                  |
| <b>FLEX</b> | 353                   | Adjacent to Connector | 308                  | PSO (primary rod)     | 327                   | Adjacent to Connector | 274                  | Adjacent to Connector + PSO (primary rod) |
| <b>EXT</b>  | 117                   | Adjacent to Connector | 121                  | Adjacent to Connector | 110                   | Adjacent to Connector | 117                  | Adjacent to Connector                     |
| <b>LB</b>   | 235                   | Adjacent to Connector | 199                  | PSO (primary rod)     | 221                   | Adjacent to Connector | 239                  | Adjacent to Connector                     |

|           |     |                                |     |                        |     |                       |     |                       |
|-----------|-----|--------------------------------|-----|------------------------|-----|-----------------------|-----|-----------------------|
| <b>RB</b> | 246 | Adjacent to Connector          | 255 | Adjacent to Connector  | 228 | Adjacent to Connector | 239 | Adjacent to Connector |
| <b>LR</b> | 304 | Adjacent to Connector          | 243 | Adjacent to Connector  | 283 | Adjacent to Connector | 227 | Adjacent to Connector |
| <b>RR</b> | 236 | Adjacent to Proximal Connector | 220 | PSO (Primary Left Rod) | 277 | Adjacent to Connector | 225 | Adjacent to Connector |

In all the loading cases, posteriorly affixed constructs showed a significant reduction in the maximum von Mises stress values compared to the 2-rod construct. The location of the maximum von Mises stress in the 4-rod head-to-head models was adjacent to the anchors that the accessory rods were connected. Using longer satellite rods with the posteriorly affixed satellite rods caused a greater reduction in the maximum von Mises stresses on the rods in all the loading directions. Figure shows the von Mises stress contour on the instrumentation during flexion in 4-rod posteriorly affixed satellite rod constructs. Table shows the values and locations of the recorded maximum von Mises stress on the rods in different loading cases and different medially affixed satellite rod constructs.

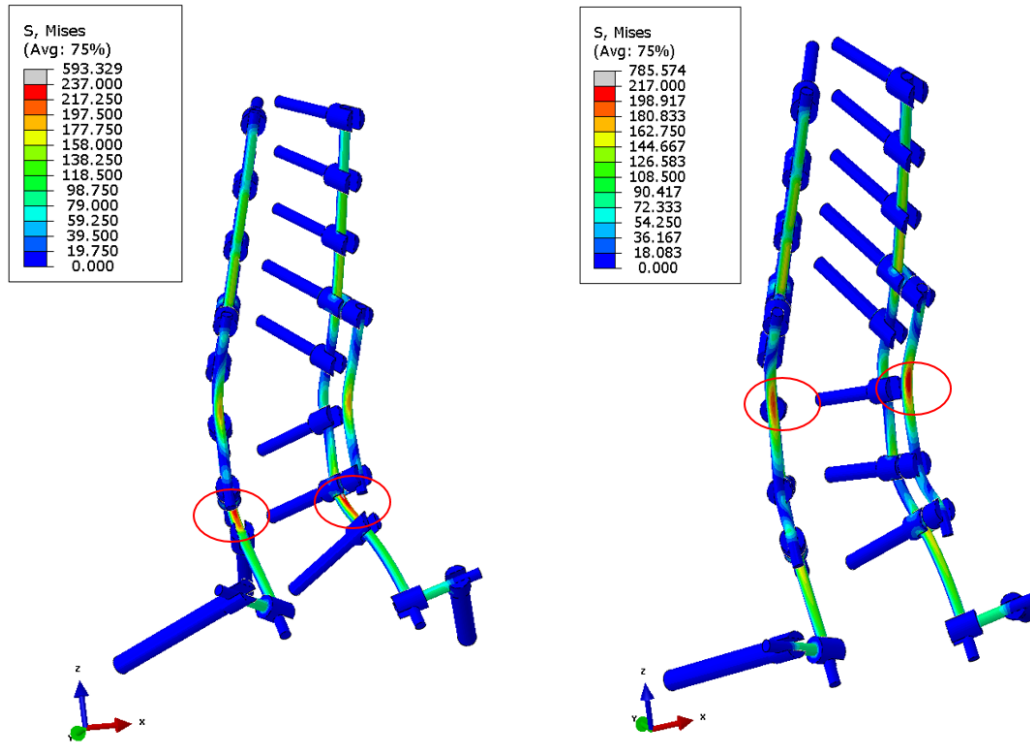


Figure 5-14 The von Mises stress contour on the instrumentation during flexion in 4-rod posteriorly affixed short satellite rod (Left) and 4-rod posteriorly affixed long satellite rod (Right) constructs. The red oval shapes show the location of the maximum von Mises stress on the rods.

Table 5.8 Maximum von Mises stress values and locations recorded on the rods in different motions and different posteriorly affixed satellite rod constructs.

|             | 4-ROD HEAD-TO-HEAD (SHORT) |                           | 4-ROD HEAD-TO-HEAD (LONG) |                           |
|-------------|----------------------------|---------------------------|---------------------------|---------------------------|
|             | Stress Value (MPa)         | location                  | Stress Value (MPa)        | location                  |
| <b>FLEX</b> | 237                        | L5-S1                     | 217                       | PSO (satellite rod)       |
| <b>EXT</b>  | 96                         | L5-S1                     | 79                        | PSO (primary rod)         |
| <b>LB</b>   | 210                        | L5-S1 (right primary rod) | 172                       | PSO (right satellite rod) |

|           |     |                                    |     |                            |
|-----------|-----|------------------------------------|-----|----------------------------|
| <b>RB</b> | 210 | L5-S1 (left primary rod)           | 162 | PSO (left satellite rod)   |
| <b>LR</b> | 173 | T12-L1 & L5-S1 (right primary rod) | 173 | T12-L1 (right primary rod) |
| <b>RR</b> | 176 | T12-L1 & L5-S1 (left primary rod)  | 170 | T12-L1 (left primary rod)  |

In all the loading cases, the short-rod construct showed a significant reduction in the maximum von Mises stress values compared to the 2-rod construct. During different motions, the maximum von Mises stress on the rods occurred on the longer rods. Figure shows the von Mises stress contour on the instrumentation during flexion in 2-rod and short-rod constructs. A comparison of the maximum von Mises stress values and locations recorded on the rods during different motions between the 2-rod and short-rod constructs was shown in Table .

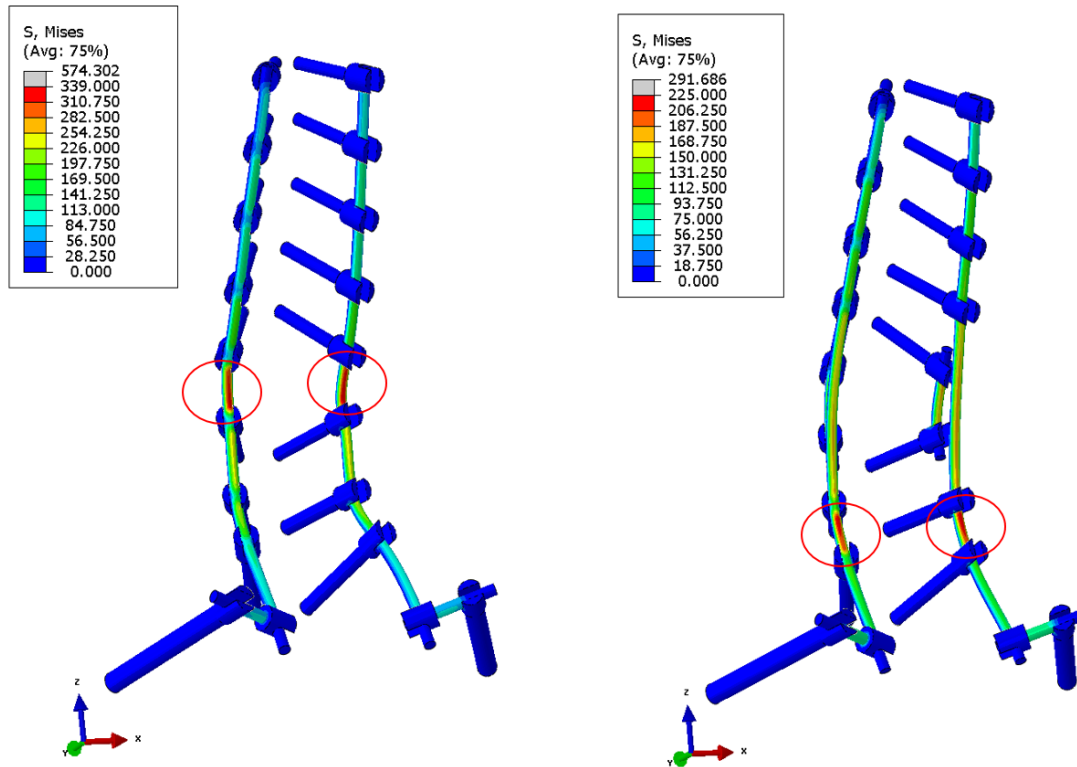


Figure 5-15 The von Mises stress contour on the instrumentation during flexion in 2-rod (Left) and short-rod (Right) constructs. The red oval shapes show the location of the maximum von Mises stress on the rods.

Table 5.9 Comparison of the Maximum von Mises stress values and locations recorded on the rods during different loading cases between the 2-rod and short-rod constructs.

|             | TWO-ROD            |                 | SHORT-ROD TECHNIQUE |                   |
|-------------|--------------------|-----------------|---------------------|-------------------|
|             | Stress Value (MPa) | location        | Stress Value (MPa)  | location          |
| <b>FLEX</b> | 339                | PSO             | 225                 | L5-S1 (long rods) |
| <b>EXT</b>  | 105                | L4-L5           | 95                  | L5-S1 (long rods) |
| <b>LB</b>   | 221                | PSO (right rod) | 195                 | L5-S1 (long rods) |

|           |     |                 |     |                   |
|-----------|-----|-----------------|-----|-------------------|
| <b>RB</b> | 221 | PSO (left rod)  | 191 | L5-S1 (long rods) |
| <b>LR</b> | 256 | PSO (right rod) | 227 | L1-L5 (long rods) |
| <b>RR</b> | 256 | PSO (left rod)  | 226 | L1-L5 (long rods) |

### 5.4.3 Force Results

The load magnitude at the osteotomy site was measured for different constructs immediately after follower load application. Compared to the 2-rod construct, using a 3-rod construct with a short or long medially affixed satellite rod decreased the load acting on the PSO by approximately 9%. In the 4-rod medially affixed constructs shorter satellite rods caused approximately 16% reduction in the loading on the PSO, while the use of longer rods caused about 17% decrease, compared to the 2-rod construct. With the comparison to the 2-rod construct, the 3-rod lateral short and long constructs caused about 6% and 5% reduction in the loads at the PSO, respectively. 4-rod lateral short and long constructs also decreased the force acting at the PSO region by 11% and 8%, respectively. The greatest amount of loading reduction at the PSO region compared to the 2-rod construct was recorded in the posteriorly affixed constructs. With the short and long satellite rods in the “head-to-head” constructs the magnitude of the force at the PSO reduced by 37% and 38%, respectively. Compared to the 2-rod construct, the least reduction in the force magnitude (0.2%) was measured with the use of “short-rod” technique. The values of the force recorded at the PSO region for different multi-rod constructs are presented in Table .

Table 5.10 Magnitude of the load acting on the PSO region in different constructs and after follower load application.

| <b>Constructs</b>            | <b>Force Magnitude</b> |
|------------------------------|------------------------|
| <b>2-rod</b>                 | 248                    |
| <b>3-Rod Medial (Short)</b>  | 226.3                  |
| <b>3-Rod Medial (Long)</b>   | 225.2                  |
| <b>4-Rod Medial (Short)</b>  | 208.9                  |
| <b>4-Rod Medial (Long)</b>   | 206.2                  |
| <b>3-Rod Lateral (Short)</b> | 233.6                  |
| <b>3-Rod Lateral (Long)</b>  | 236                    |
| <b>4-Rod Lateral (Short)</b> | 221.9                  |
| <b>4-Rod Lateral (Long)</b>  | 227                    |
| <b>Short-Rod Technique</b>   | 247.6                  |
| <b>Head-to-Head (Short)</b>  | 156.5                  |
| <b>Head-to-Head (Long)</b>   | 153.9                  |

## **5.5 Results of the FE Interbody Spacer Constructs**

### **5.5.1 Range of Motion Results**

Supplementing the instrumented spinopelvic PSO model using interbody spacers reduced the T10-S1 range of motion. The reduction of motion in flexion, extension, lateral bending, and axial rotation due to the insertion of interbody spacers below and above the PSO level was about 22%, 21%, 4%, and 11%, respectively. Compared to the 2-rod construct, in a case where all the lumbar levels were fused using the interbody spacers, T10-S1 flexion, extension, lateral bending, and axial rotation motions reduced about 56%, 56%, 8%, and 26%, respectively. A comparison of the instrumented T10-S1 global ROM for different loading cases and different configurations of interbody spacers is shown in Figure .

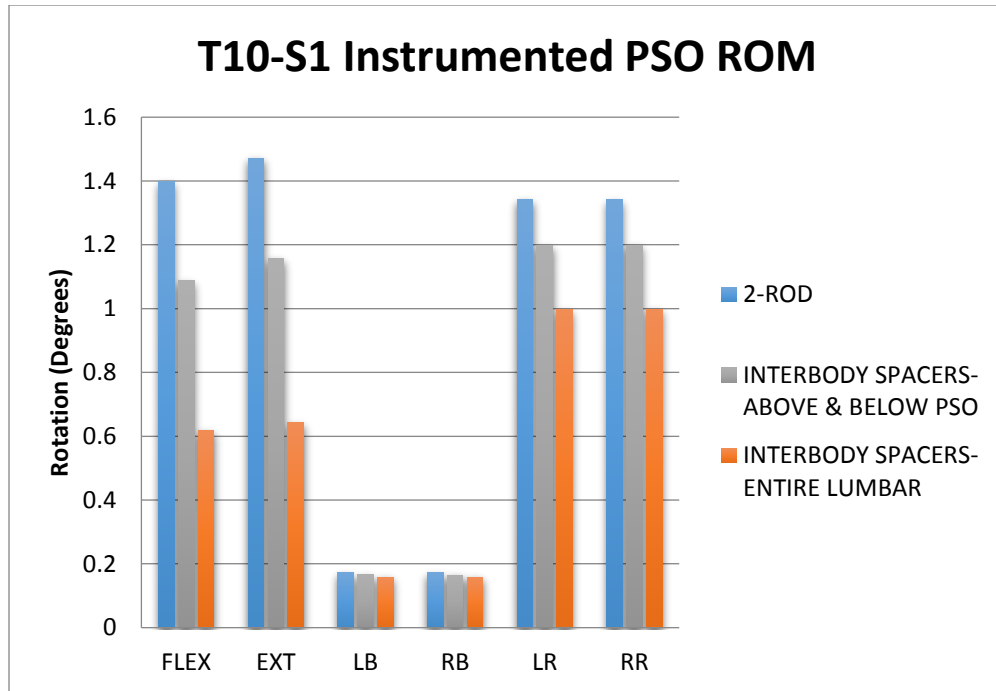


Figure 5-16 Comparison of the instrumented T10-S1 global ROM for different loading cases and different configurations of interbody spacers.

### 5.5.2 Von Mises Stress Results

Using two interbody spacers above and below the PSO level had a significant effect in decreasing the maximum von Mises stress on the rods. The greatest variation of the maximum von Mises stress occurred in flexion motion. Compared to the 2-rod constructs, during this motion about 33% maximum von Mises stress reduction on the rods was observed. The least stress reduction related to the extension motion and it was about 4%. Instrumenting all the lumbar spine levels with the interbody spacers significantly decreased the stress values in all the loading cases. Similar to the two cage model, the greatest reduction in the maximum von Mises stress was in flexion which was about 60%, and the least stress reduction was in extension, and it was approximately 21%. Interestingly, adding

interbody spacers above and below the PSO (at L2-L3 and L3-L4) shifted the location of maximum von Mises stress on the rods in different loading cases to L4-L5. Table shows maximum von Mises stress values and locations on the rods in different loading cases and interbody spacer constructs.

Table 5.11 Maximum von Mises stress values and locations recorded on the rods in different motions and different interbody spacer constructs.

|             | <b>INTERBODY SPACERS ABOVE &amp; BELOW PSO</b> |                   | <b>INTERBODY SPACERS ENTIRE LUMBAR LEVELS</b> |                     |
|-------------|--|-------------------|---|---------------------|
|             | Stress Value (MPa)                             | location          | Stress Value (MPa)                            | location            |
| <b>FLEX</b> | 227  | L4-L5             | 134   | T11-T12             |
| <b>EXT</b>  | 101  | L4-L5             | 83  | S1-Iliac Screw      |
| <b>LB</b>   | 197  | L4-L5 (right rod) | 121   | T10-T11 (left rod)  |
| <b>RB</b>   | 201  | L4-L5 (left rod)  | 121   | T10-T11 (right rod) |
| <b>LR</b>   | 224  | L4-L5 (right rod) | 173   | T12-L1 (right rod)  |
| <b>RR</b>   | 220  | L4-L5 (left rod)  | 174   | T12-L1 (left rod)   |

### 5.5.3 Force Results

Use of interbody spacers considerably increased the force magnitude at the PSO fracture site. Adding two interbody spacers adjacent to the PSO level caused a force magnitude of 335.6N at the PSO site. By adding the interbody spacers at all the lumbar levels, this value changed to 353.4N.

## **5.6 Results of the FE Cross-Connector Constructs**

### **5.6.1 Range of Motion Results**

By adding different configurations of the cross connector to the 2-rod construct of the PSO, similar T10-S1 lateral bending ROM was observed. The greatest variation of about 2% in lateral bending was seen when the connector was added above the PSO. Among different cross-connector constructs, the greatest reduction of about 2.5% in flexion motion was recorded while the cross-connector was used at the PSO region. In the axial rotation, adding a cross-connector above and below the PSO reduced the range of motion about 5%. This was followed by the construct in which the cross-connector was instrumented above the PSO that reduced the axial rotation about 3%. A comparison of the instrumented T10-S1 global range of motion for different motions and configurations of the cross-connector is given in Figure .

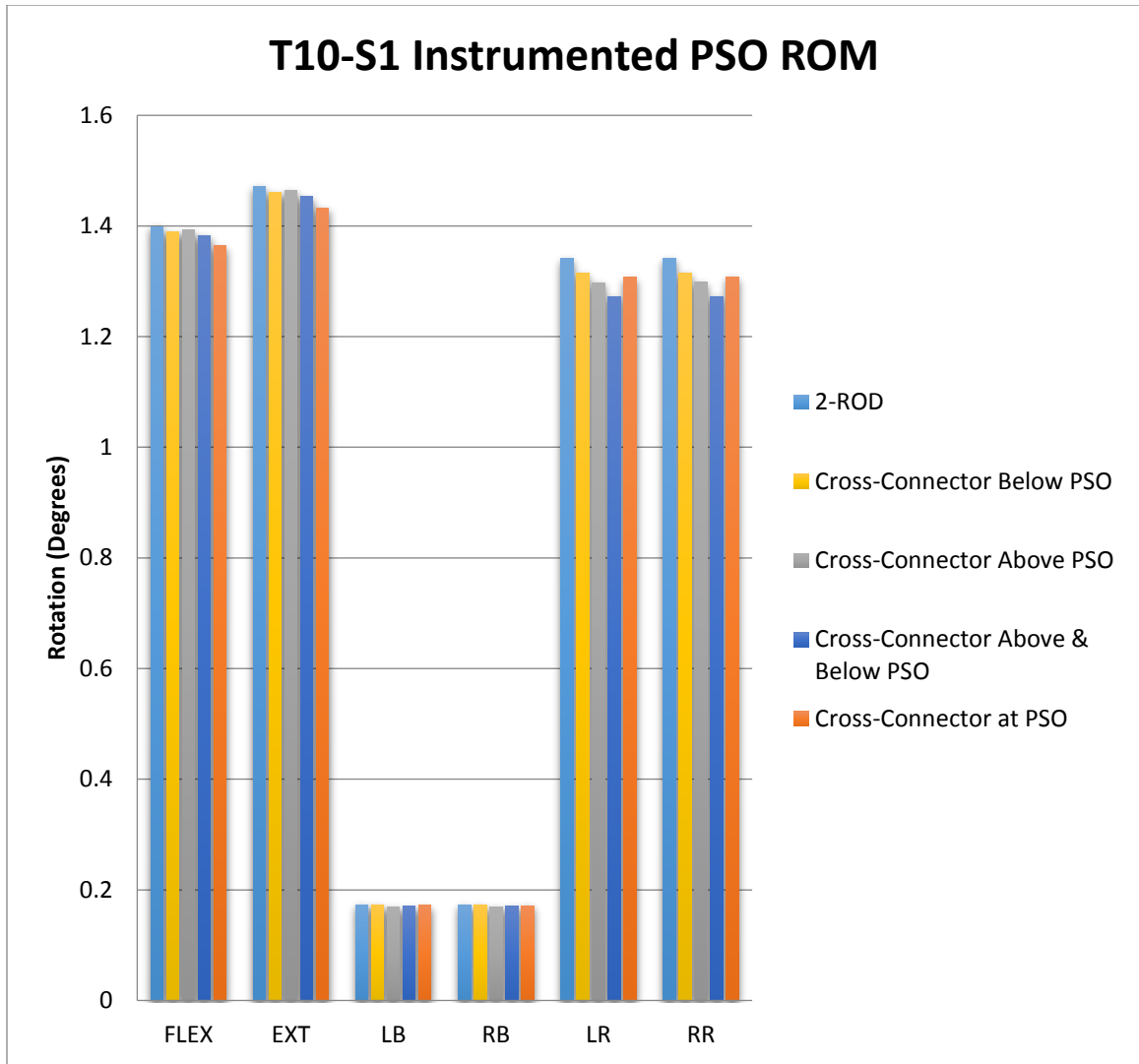


Figure 5-17 Comparison of the instrumented T10-S1 global ROM for different loading cases and different locations of the cross-connector.

### 5.6.2 Von Mises Stress Results

In different cross connector constructs, the maximum von Mises stress on the rods was similar for different loading cases. Compared to the 2-rod constructs, adding a cross-connector at the PSO decreased the maximum von Mises stress on the rods during flexion, extension, and left or right rotation by about 1%, 2%, and 2%, respectively, while it

increased the stress by about 2% in lateral bending. In comparison with the 2-rod construct, during extension adding the cross-connector below the PSO increased the maximum von Mises stress on the rods by approximately 7%. In all other settings and motions, minor changes in the maximum stress values were recorded. Table shows the location and values of the maximum von Mises stress on the rods in different loading cases and cross-connector configurations.

Table 5.12 Maximum von Mises stress values and locations recorded on the rods in different motions and different locations of the cross-connector.

|             | <b>CROSS CONNECTOR AT PSO</b> |                 | <b>CROSS CONNECTOR ABOVE PSO</b> |                 | <b>CROSS CONNECTOR BELOW PSO</b> |                 | <b>CROSS CONNECTOR ABOVE &amp; BELOW</b> |                 |
|-------------|-------------------------------|-----------------|----------------------------------|-----------------|----------------------------------|-----------------|--|-----------------|
|             | Stress Value (MPa)            | location        | Stress Value (MPa)               | location        | Stress Value (MPa)               | location        | Stress Value (MPa)                       | location        |
| <b>FLEX</b> | 336                           | PSO             | 340                              | PSO             | 340                              | PSO             | 342                                      | PSO             |
| <b>EXT</b>  | 103                           | L4-L5           | 105                              | L4-L5           | 112                              | S1-Iliac Screw  | 112                                      | S1-Iliac Screw  |
| <b>LB</b>   | 226                           | PSO (right rod) | 222                              | PSO (right rod) | 221                              | PSO (right rod) | 221                                      | PSO (right rod) |
| <b>RB</b>   | 225                           | PSO (left rod)  | 222                              | PSO (left rod)  | 221                              | PSO (left rod)  | 221                                      | PSO (left rod)  |
| <b>LR</b>   | 250                           | PSO (right rod) | 252                              | PSO (right rod) | 261                              | PSO (right rod) | 256                                      | PSO (right rod) |
| <b>RR</b>   | 250                           | PSO (left rod)  | 251                              | PSO (left rod)  | 261                              | PSO (left rod)  | 256                                      | PSO (left rod)  |

### **5.6.3 Force Results**

By adding cross-connector to the 2-rod construct, the magnitude of the force acting on the fractured surface due to PSO decreased. By having the cross-connector at the PSO region the force magnitude reduced to 241.6N. Adding the cross-connector above and below the PSO decreased the force magnitude to 246.7N. Similar force magnitudes were obtained by attaching the cross-connector above (247.3N) or below (247.4N) PSO.

## **6 Discussion**

### **6.1 Overview**

This chapter covers a thorough discussion of the results for the present FE study, beginning with the validation results of the FE models, and proceeding to a discussion on the effects of intervertebral disc geometry and degeneration on the rods following PSO. In the second part of this chapter, the results for the alternative constructs following PSO are discussed in detail. Finally, the limitations and conclusions of the study are described.

### **6.2 FE Models Validation**

The osseoligamentous 3D PSO spinopelvic model was initially developed from a previously validated spinopelvic FE model. Due to the lack of any experimental work on the PSO kinematics exclusively, the trend of L1-S1 ROM of the spinopelvic models before and after PSO was compared to previously published FEA data [16, 28]. Due to the severe instability of the PSO and convergence issues at 7.5Nm, similar moments applied by Ottardi et al. in different directions were used in this study (7.5Nm in flexion, 3Nm in extension, 4Nm in lateral bending, and 3Nm in axial rotation). Despite the differences in the geometries and simulation methods, the results of Ottardi et al. study show a similar

increasing trend in flexion, extension and axial rotation. In lateral bending, our results showed 26% reduction of motion while Ottardi et al. reported an increase of about 8%. However, Charosky et al. have previously reported that in lateral bending the PSO alone caused 17% reduction in the motion.

For further validation, the instrumented PSO model range of motion data across the osteotomy site (L2-L4) was compared to the Deviren et al. experimental work [22]. The model outcomes agreed reasonably well with the experimental data. For flexion/extension and lateral bending range of motions, the values fell within one standard deviation of the mean, while the axial rotation motion fell within two standard deviations from the mean.

The biomechanics of the intervertebral disc degeneration is extremely complex, and there is a lack of experimental work on the degenerated spine that includes a PSO. Given the PSO at the L3 level and the lack of experimental data for degenerated intervertebral discs adjacent to the PSO, the range of motion for only L1-L2, L4-L5, and L5-S1 segments were compared to the experiments in the literature. The trend of ROM for the disc degeneration models of the three aforementioned levels agreed well with the Mimura et al. experimental study [118]. In their study, with increasing in the disc degeneration, flexion-extension and lateral bending motions decreased while the axial rotation initially increased then decreased. In our study, the same trend of ROM was observed. For the healthy disc motion segments, the lateral bending ROM values fell within three standard deviations of the mean. For this motion, the model was previously validated using other cadaver studies [32]. Park et al. reported a similar ROM trend for the L4-L5 motion segment [126]. The authors reported a reduction with disc degeneration in flexion-extension and lateral

bending motions, while the axial rotation showed an increase in early stages of degeneration and then decreased with severe degeneration.

### **6.3 IVD Geometry Effects on the Rods Following PSO**

Pedicle subtraction osteotomy is an intricate surgical intervention to correct sagittal plane deformities. Although PSO is a very effective method to address the sagittal malalignment, it is associated with a great risk of complications. Among several complications associated with this method, rod failure is a major reason for revision surgeries [9, 12, 13, 161, 164]. In a multicenter retrospective study, Smith et al. reported 15.8% symptomatic rod fracture following PSO [13]. In another prospective multicenter investigation, the rate of rod fracture in patients underwent PSO was reported to be about 22% [161].

In a recent study, Briski et al. indicated the lumbar disc geometry as a risk factor affecting the rod failure [18]. The authors reported that the group of patients who experienced the rod fracture had larger non-fused disc heights at the two levels immediately cranial and caudal to the PSO. The first objective of the present FE study was to understand the effect of lumbar disc height on the rods following PSO. Therefore, three different disc degenerated models with different heights (Mildly degenerated, moderately degenerated, and severely degenerated) were developed and analyzed regarding the range of motion, anterior force at the osteotomy site, and the maximum von Mises stress on the rods. The results of the current study indicate that larger discs adjacent to the PSO leads to a greater motion and instability at this region. The superior mobility of the segments adjacent to the

PSO region can result in a greater maximum von Mises stress on the rods. Due to lower stress values on the rods with further disc degeneration, lower risk of rod fracture is expected. The results further indicated that after follower load application with an increase in the disc degeneration a greater amount of load acts on the osteotomy region. These observations indicate that with the disc degeneration a greater amount of load is carried by the anterior column of the spine and a lower portion of the total load is transferred to the posterior instrumentation. The lower amount of load transfer to the instrumentation also can result in the reduction of the maximum von Mises stress on the rods.

Several studies investigated the location of rod failure following PSO [16, 166, 173, 174]. In a multicenter retrospective study of 443 patients Smith et al., assessed the symptomatic rod fracture following adult spinal deformity. The rods failed at or adjacent to the level of the PSO region in 89% (16 out of 18) of the fractures. Tang et al. conducted a biomechanical study on the severity of the rod contour in a PSO setting. The authors found that the fatigue life of the rods depends significantly on the severity of the rod angle, and more severe angles have a greater risk of fracture. The results of our study also showed that the maximum von Mises stress concentration in the instrumented PSO models with different disc heights occurred during the flexion motion and at the PSO region.

## **6.4 FE Analysis of the Multi-rod Constructs**

To mitigate the rod fracture rate, clinicians have used various techniques in supplementing the posterior instrumentations. New techniques involve using the multi-rod configurations which enhance the stiffness and stability of the construct. Hallager et al. in

an in vitro study assessed the effect of adding two short pre-contoured accessory rods medially to the primary rods on the range of motion and rods strain after PSO. They concluded that the accessory and COCR rods provided the greatest motion reduction at the PSO level. The results of the current study also showed that by adding satellite rods medially and laterally the global T10-S1 range of motion decreased in all directions and more specifically during flexion, extension, and axial rotation. A greater motion reduction in all directions was observed in the medially affixed multi-rod settings than in the corresponding laterally affixed multi-rod constructs. In general, among all multi-rod constructs, due to the greater rigidity of the instrumentation the motion reduction in different loading directions with the longer satellite rods was greater than the shorter rods.

The novel pedicle screw design patented by Frankel et al. allows for the posterior connection between the secondary rods and the primary rods [171]. Even though these screws have not been manufactured or tested before, the results of our FE simulations were promising. Among all multi-rod constructs, the greatest motion reduction in all directions was observed with the use of longer posteriorly affixed “head-to-head” 4-rod technique. In this construct, the longer rod and greater number of connections between the primary and satellite rods enhance the stiffness of the instrumentation and explain the higher stability of the construct.

Hyun et al. compared the rod fracture rate in multi-rod constructs to standard 2-rod constructs following 3-column osteotomies [21]. Their retrospective comparative study showed that the 2-rod constructs had significantly greater rod breakage than the multi-rod constructs. Overall, having multiple rods attached together using side-by-side connectors increases the moment of inertia which results in lower stress on the instrumentations. The

result of our computational study also indicated that by adding satellite rods in all the motions, the magnitude of the maximum von Mises stress at the PSO region on the rods decreased significantly. Lower maximum stress values at the PSO region indicate a lower risk of rod failure at this site. However, it was observed that in several multi-rod cases by adding the satellite rods using dominos the location of the maximum von Mises stress on the rods in different motions occurred adjacent to the connectors. The stress concentration adjacent to the dominos is due to the transition from more rigid two bonded rods section (primary and secondary rods) to the less rigid one rod (primary rod) section. In the biomechanical study of Hallager et al., authors reported with medially connected satellite rods in the 4-rod constructs greater strain occurred on the accessory rods [167]. Moreover, Luca et al. conducted a finite element study on the similar constructs with titanium alloy rods and recorded greater maximum von Mises stress at the PSO region of the accessory rods [17]. Our results indicate that in both medially and laterally affixed multi-rod constructs the maximum von Mises stress at the PSO region occurred on the medial rods. In the medially affixed constructs greater maximum von Mises stress occurred on the satellite rods while in the laterally affixed multi-rod constructs it was located on the primary rods. These observations indicate that at the PSO region in the medially affixed constructs there is a greater risk of rod failure in satellite rods while in the laterally affixed constructs it is on the primary rods. In addition, the maximum von Mises stress values recorded for the two constructs at the PSO region was greater in laterally affixed constructs than the medially affixed ones which imply a greater risk of failure in laterally affixed constructs. These findings exhibit a significant benefit in supplementing the PSO setting

with the medially affixed satellite rods over the laterally affixed satellite rods that in the case of rod failure the surgeon can readily replace the satellite rods instead of primary rods.

In the posteriorly connected satellite rod constructs the location of maximum von Mises stress in different loading cases occurred either adjacent to the anchors where the secondary rods ended or at the PSO region. Similar to the medially and laterally affixed satellite rod constructs, due to transition in the rigidity from two-rod to one-rod region the stress concentration adjacent to these anchors was high. The longer head-to-head construct had a greater number of connections between the primary and secondary rods. This increased the stability of the instrumentation and led to a lower maximum von Mises stress in flexion motion on the primary rods, and finally a lower risk of rod fracture. In flexion motion, posteriorly affixed multi-rod constructs decrease the maximum von Mises stress on the rods more than the medially and laterally affixed satellite rod constructs. Luca et al. in a finite element study of the instrumentation failure following PSO also noted that placing the satellite rods posteriorly allowed for more stress reduction on the instrumentation [17].

Gupta et al. have recently reported on a 4-rod technique in which the principal rods were not connected to the pedicle screws anchored adjacent to the PSO level, while additional two short rods were spanning on the PSO level using anchors connected to the adjacent levels [29]. They compared the rod fracture rate using this novel method with the traditional 2-rod technique, and reported 0 % rod failure with 4 rods, compared to a 25% of fracture with the 2-rod. For this construct, our results also showed a significant reduction in the maximum von Mises stress values in different motions compared to the 2-rod construct. With this method, the longer rods are not connected to the anchors adjacent to

the PSO averting a need for severe rod contouring at this region. In this regard, Tang et al. conducted a biomechanical study on the severity of rod contour in a PSO setting and found that the fatigue life of the rods depends significantly on the severity of the rod contour, and more severe angles have a greater risk of fracture [166].

Similar to Luca et al. observations that adding two satellite rods medially increases the posterior force on the instrumentation, our results show that following follower load application in all multi-rod constructs the load acting on the PSO region decreases. Adding secondary rods enhances the stiffness of the instrumentation which leads to greater load transfer to the posterior instrumentation that causes a reduction in the force acting on the osteotomy region. Among all multi-rod constructs, the closest force magnitude recorded at the osteotomy site to the 2-rod construct was seen in the short-rod technique.

Bone healing is a complex procedure which is influenced by multiple factors. The dynamics and distribution of the mechanical loading, bone cells and mechanical receptors, blood perfusion, metabolite supplies, growth factors, cytokines, and hormones are among several important factors affecting the bone fracture healing [175-179]. According to the Wolff's Laws, the mechanical function influences the bone tissue formation and remodeling [180]. Mechanical loading causes strain on the bone that yields signals which cells can detect and respond. In bone fracture healing excessive strain on the fracture site results in instability followed by delayed healing or non-union. On the other hand, rigid instrumentation often causes very limited strain at the fracture site which is inadequate to stimulate the bone formation. As a result of the inadequate stimulus, the callus formation may weaken, and a non-union might occur [181, 182]. Our findings showed that with the use of multi-rod constructs (except short-rod technique) the magnitude of the force acting

on the osteotomy site decreased significantly. Even though multi-rod constructs decrease the rod fracture rate by reducing the maximum von Mises stress, due to force reduction on the anterior column they may delay the bone union at the PSO site. In this regard, the short-rod technique not only provided similar force acting on the anterior column, but also it was accompanied with a significant maximum von Mises stress reduction on the rods. The results of the current analysis are also in good agreement with the outcomes of the Luca et al. FE study [17].

## **6.5 FE Analysis of the Interbody Spacer Constructs**

Another goal of our study was to investigate the biomechanical effects of interbody spacers in the long constructs followed by PSO. To mitigate pseudoarthrosis and rod fracture rate, Enercan et al. suggested the use of interbody spacers adjacent to the PSO level [153]. Deviren et al. in a cadaveric study investigated the use of interbody spacers adjacent to the PSO level in different loading cases and reported a modest stabilization effect. There are only two computational studies that investigated the effect of adding interbody spacers in the models having PSO fused with anchors at the two levels above and below the osteotomy level [16, 27]. Charosky et al. reported a reduction in bending moments on the rods when an interbody spacer was used below the PSO [16]. Luca et al. in a finite element study showed that following the use of two interbody spacers above and below PSO about 8% reduction in ROM and 42-51% reduction in maximum von Mises stresses on the rods were achieved [27]. These values could not be directly compared to our results due to differences in the geometries, materials, cage designs, and levels of

instrumentation. Our findings showed that by adding two interbody spacers above and below the PSO, the range of motion in different directions decreased about 4-22% while adding cages to all L1-S1 IVDs reduced the ROM in different directions from 8-56%. Hallager et al. also in a biomechanical study reported that by adding interbody spacers above and below the PSO, the magnitude of the strain measured on the rods decreased in flexion-extension motion [167]. In this regard, our computational analyses showed that adding interbody spacer above and below the PSO level decreased the maximum von Mises stress recorded on the rods by about 33% while adding it to all lumbar levels further decreased the maximum von Mises stress values by about 49%.

Our computational analyses showed that by adding interbody spacers to the 2-rod construct, the magnitude of the force acting on the osteotomy region increased. Adding interbody spacers to the anterior column increases the stiffness of this region. The increase in the stiffness of the spine causes a load transfer to the anterior column. More forces acting on the spine decreases the force acting on the instrumentation which leads to lower von Mises stresses and finally lower risk of rod fracture.

## **6.6 FE Analysis of the Cross-Connector Constructs**

Adding cross-connector in spinal fusions have been shown to enhance the torsional stiffness in constructs [183-185]. However, to the author's knowledge, there has been no study on the effect of adding cross-connector to the PSO setting. Kuklo et al. in a biomechanical study investigated the use of cross-connectors following long segment instrumentation. They found that cross-connectors did not affect flexion-extension or

lateral bending stability while axial rotation stability improved significantly. In our FEA, we studied four different configurations of cross-connectors (At the PSO, above PSO, below PSO, and above and below PSO). The results of our computational modeling showed that by adding cross-connector to the 2-rod constructs the values of T10-S1 ROM and the maximum von Mises stress on the rods did not change significantly. The greatest motion reduction of about 5% was recorded in axial rotation and by adding the cross-connectors above and below the PSO region. However, during axial rotation in this construct, no significant change was recorded in the value of the maximum von Mises stress. Compared to the 2-rod construct, during some motions in different cross-connector configurations, minor increases in the values of maximum von Mises stress on the rods were recorded. In flexion motion, when two cross-connectors were added above and below the PSO, a slight increase in the maximum von Mises stress on the rods at the PSO region was observed. Barton et al. also indicated that the use of two or more cross-links held an increased risk of rod fracture with borderline statistical significance [14]. Yamaguchi et al. suggested that more rigid constructs may have lower mechanical slop that exacerbates the rod failure [186]. Following the same postulation, using multiple cross-connectors results in a more rigid construct which resists greater portion of loading as opposed to a less rigid 2-rod construct that provides a greater range of motion and mechanical slop.

Adding cross-connectors to the PSO setting slightly decreased the force acting on the osteotomy level. Similar to the multi-rod constructs, adding cross-connectors enhances the rigidity of the configuration leading to a greater transfer of the loads to the posterior instrumentation. This load transfer to the posterior instrumentation causes a reduction in the force acting on the osteotomy surfaces.

## 6.7 Limitations and Future Work

Similar to any other finite element analysis, the limitations of the current computational study should be taken into account. Unavailability of the range of motion data for the cadaveric osteoligamentous spine associated with PSO is a limitation of this study. Nevertheless, the results of the current study were compared to the previous FE studies, and despite different modeling techniques, similar trends of ROMs were achieved. Besides, the range of motion of the instrumented PSO model at the osteotomy region was compared to the Deviren et al. cadaveric study [22]. Second important limitation of the current study was that no muscle forces were simulated in the models. However, this limitation was mitigated using the follower load method as previously published by Patwardhan et al. [172]. Follower load method provides similar kinematic responses as those in vivo. Third, the contacts and constraints in the models and the geometries of the implants were simplified, and the index surgery procedure was not simulated. In this regard, the simulation of the residual stress on the rods and other components which is caused by intraoperative contouring and the spine instrumentation maneuvers was neglected in the models.

Spine degeneration is a very complex process, and different factors are involved which cannot be readily simulated using FE analyses. For instance, osteophyte formation which is often associated with the disc degeneration was not considered in our models. In addition, the change in the height of the intervertebral discs may result in decreased or increased lordosis angles which can affect the instrumentation contours, ROM, and stress values on the rods. Moreover, facets degeneration and annulus tears during degeneration

process were neglected in these simulations. Due to the lack of information for the degenerated annulus material properties, the material properties of this component was not altered within different grades of degeneration.

Dynamic analysis of the components such as fatigue test provides more accurate failure assessment of the rods. No dynamic analysis was simulated in this study, and fatigue testing of different constructs of the current FE study is suggested for the future assessments. Other recommendations for future studies include considering several variables like preoperative flexibility, preoperative radiographic parameters (lordosis angle, pelvic incidence, SVA etc.), the extent of fusion levels, weight, PSO correction angle, and size and type of instrumentation. Another avenue of the research could include in vivo studies of the animal models. Using these models we can also evaluate the quality of the bone growth and union at the osteotomy site using different instrumentation techniques. Moreover, the model of this dissertation only consisted of osteoligamentous components of the spine. However, the addition of muscle forces to such a model could allow for more accurate determination of the biomechanics and failure modes of different components. The addition of the full thoracic and cervical regions to this study can further elucidate the changes in the kinematics of the upper levels following PSO. These models could also allow evaluating the construct stiffness as a risk factor for proximal junctional kyphosis.

## 6.8 Conclusions

The effects of the lumbar disc height alteration due to degeneration on the range of motion, maximum von Mises stress on the rods, and the loads on the osteotomy site were studied. In addition to that, the effects of alternative instrumentation techniques using various medially, laterally, and posteriorly affixed satellite rods configurations, the short-rod technique proposed by Gupta et al., and adding interbody spacers and cross-connectors to the PSO setting were analyzed. The results of the study satisfy all the previously outlined hypotheses.

The findings of the current FE study imply that due to degeneration as the lumbar disc height decreases, the stability adjacent to the PSO region increases and the maximum von Mises stress on the rods reduces which results in a lower risk of rod fracture. In addition, with an increase in the disc degeneration the amount of load acting on the osteotomy region increases. Results of the disc degeneration study also showed that the maximum von Mises stress on the rods occurs during flexion motion and at the PSO region.

In multi-rod constructs, adding multiple accessory rods increases the stability of the construct, and at the PSO region decreases the maximum von Mises stress on the rods. Among all multi-rod constructs, the greatest motion reduction in all directions was observed with the use of posteriorly affixed “head-to-head” 4-rod technique followed by medially affixed and laterally affixed satellite rods. Moreover, the results for the medially and laterally affixed satellite rods highlighted that the maximum von Mises stress on the rods occurs adjacent to the dominos, while at the PSO region it occurs on the medial rods. These observations indicate that at the PSO region in the medially affixed constructs there

is a greater risk of rod failure in satellite rods while in the laterally affixed constructs it is on the primary rods. These findings exhibit a significant benefit in supplementing the PSO setting with the medially affixed satellite rods over the laterally affixed satellite rods that in the case of rod failure at the PSO region the surgeon can simply replace the satellite rods instead of the primary rods. The assessment of the load acting on the osteotomy region also signified that except short-rod technique all other multi-rod constructs decrease the magnitude of the load acting on this region which may cause in delayed union or non-union of the PSO site. The greatest load reduction at the osteotomy region was recorded in the posteriorly affixed head-to-head constructs followed by 4-rod medially and laterally affixed satellite rod configurations. In conclusion, the current FEA of the von Mises stress values showed that the 4-rod posteriorly affixed head-to-head technique has the lowest risk of rod failure followed by the short-rod method and medially and laterally affixed satellite rods.

Additionally, interbody spacer placement in the PSO setting decreases the ROM and the maximum von Mises stress on the rods, while it increases the force acting on the osteotomy region. Hence, adding interbody spacers to the PSO setting may contribute in the bone union at the osteotomy region and can decrease the risk of rod failure.

Finally, adding cross-connectors to a PSO acute setting has a slight stabilizing potential in axial rotation motion. Additionally, the greater number of cross-links increases the rigidity of the construct which results in increasing the maximum von Mises stress values at the PSO region, and ultimately exacerbates the rod fracture.

## 7 References

1. Youssef, J., et al., Current status of adult spinal deformity. *Global spine journal*, 2013. 3(01): p. 051-062.
2. Yamato, Y., et al., Calculation of the target lumbar lordosis angle for restoring an optimal pelvic tilt in elderly patients with adult spinal deformity. *Spine*, 2016. 41(4): p. E211-E217.
3. Buchowski, J.M., et al., Neurologic complications of lumbar pedicle subtraction osteotomy: a 10-year assessment. *Spine*, 2007. 32(20): p. 2245-2252.
4. Bridwell, K.H., et al., Pedicle subtraction osteotomy for the treatment of fixed sagittal imbalance. *JBJS*, 2003. 85(3): p. 454-463.
5. Booth, K.C., et al., Complications and predictive factors for the successful treatment of flatback deformity (fixed sagittal imbalance). *Spine*, 1999. 24(16): p. 1712.
6. Casey, M.P., et al., The effect of Harrington rod contouring on lumbar lordosis. *Spine*, 1987. 12(8): p. 750-753.
7. Joseph Jr, S.A., et al., Sagittal plane deformity in the adult patient. *Journal of the American Academy of Orthopaedic Surgeons*, 2009. 17(6): p. 378-388.
8. Kose, K.C., et al., Spinal osteotomies: indications, limits and pitfalls. *EFORT Open Reviews*, 2017. 2(3): p. 73-82.
9. Schwab, F., et al., The comprehensive anatomical spinal osteotomy classification. *Neurosurgery*, 2013. 76(suppl\_1): p. S33-S41.
10. Smith, J.S., et al., Short-term morbidity and mortality associated with correction of thoracolumbar fixed sagittal plane deformity: a report from the Scoliosis Research Society Morbidity and Mortality Committee. *Spine*, 2011. 36(12): p. 958-964.

11. Charles, Y.P., B. Yu, and J.-P. Steib, Sacroiliac joint luxation after pedicle subtraction osteotomy: report of two cases and analysis of failure mechanism. *European Spine Journal*, 2016. 25: p. 63.
12. Smith, J.S., et al., Prospective multicenter assessment of risk factors for rod fracture following surgery for adult spinal deformity. *Journal of Neurosurgery: Spine*, 2014. 21(6): p. 994-1003.
13. Smith, J.S., et al., Assessment of symptomatic rod fracture after posterior instrumented fusion for adult spinal deformity. *Neurosurgery*, 2012. 71(4): p. 862-868.
14. Barton, C., et al., Risk factors for rod fracture after posterior correction of adult spinal deformity with osteotomy: a retrospective case-series. *Scoliosis*, 2015. 10(1): p. 30.
15. Berjano, P., et al., Failures and revisions in surgery for sagittal imbalance: analysis of factors influencing failure. *European Spine Journal*, 2013. 22(6): p. 853-858.
16. Charosky, S., P. Moreno, and P. Maxy, Instability and instrumentation failures after a PSO: a finite element analysis. *European Spine Journal*, 2014. 23(11): p. 2340-2349.
17. Luca, A., et al., Instrumentation failure following pedicle subtraction osteotomy: the role of rod material, diameter, and multi-rod constructs. *European Spine Journal*, 2017. 26(3): p. 764-770.
18. Briski, D., J. Zavatsky, and B. Cook, How Lumbar Disc Geometrics Affect the Risk for Rod Fracture in Patients Undergoing Adult Spinal Deformity Surgery: An Initial Report. *Global Spine Journal*, 2016. 6(1\_suppl): p. s-0036-1582869-s-0036-1582869.
19. Barrey, C., et al., Pedicle subtraction osteotomy in the lumbar spine: indications, technical aspects, results and complications. *European journal of orthopaedic surgery & traumatology: orthopedie traumatologie*, 2014. 24: p. S21-30.
20. Cho, K.-J., et al., Pedicle subtraction osteotomy in elderly patients with degenerative sagittal imbalance. *Spine*, 2013. 38(24): p. E1561-E1566.
21. Hyun, S.-J., et al., Comparison of standard 2-rod constructs to multiple-rod constructs for fixation across 3-column spinal osteotomies. *Spine*, 2014. 39(22): p. 1899-1904.

22. Deviren, V., et al., Construct rigidity after fatigue loading in pedicle subtraction osteotomy with or without adjacent interbody structural cages. *Global spine journal*, 2012. 2(04): p. 213-220.
23. Slivka, M.A., Y.K. Fan, and J.C. Eck, The effect of contouring on fatigue strength of spinal rods: is it okay to re-bend and which materials are best? *Spine deformity*, 2013. 1(6): p. 395-400.
24. Nguyen, T., et al., The fatigue life of contoured cobalt chrome posterior spinal fusion rods. *Proceedings of the Institution of Mechanical Engineers, Part H: Journal of Engineering in Medicine*, 2011. 225(2): p. 194-198.
25. Stambough, J.L., et al., Biomechanical assessment of titanium and stainless steel posterior spinal constructs: effects of absolute/relative loading and frequency on fatigue life and determination of failure modes. *Clinical Spine Surgery*, 1997. 10(6): p. 473-481.
26. Lindsey, C., et al., The effects of rod contouring on spinal construct fatigue strength. *Spine*, 2006. 31(15): p. 1680-1687.
27. Luca, A., et al., Anterior support reduces the stresses on the posterior instrumentation after pedicle subtraction osteotomy: a finite-element study. *European Spine Journal*, 2017: p. 1-7.
28. Ottardi, C., et al., Finite element analysis of the lumbar destabilization following pedicle subtraction osteotomy. *Medical engineering & physics*, 2016. 38(5): p. 506-509.
29. Gupta, S., et al. Four Rods Prevent Rod Breakage and Pseudarthrosis in Pedicle Subtraction Osteotomies.: Gp243. in *Spine Journal Meeting Abstracts*. 2014. LWW.
30. Najarian, S., J. Dargahi, and B. Heidari, Biomechanical effect of posterior elements and ligamentous tissues of lumbar spine on load sharing. *Bio-medical materials and engineering*, 2005. 15(3): p. 145-158.
31. Haher, T., et al., Biomechanics of the spine in sports. *Clinics in sports medicine*, 1993. 12(3): p. 449-464.
32. Palepu, V., Biomechanical effects of initial occupant seated posture during rear end impact injury. 2013, University of Toledo.
33. Adams, M. and P. Dolan, Recent advances in lumbar spinal mechanics and their clinical significance. *Clinical Biomechanics*, 1995. 10(1): p. 3-19.

34. Hamill, J. and K.M. Knutzen, *Biomechanical basis of human movement*. 2006: Lippincott Williams & Wilkins.
35. WHITE III, A.A. and M.M. Panjabi, The basic kinematics of the human spine: A review of past and current knowledge. *Spine*, 1978. 3(1): p. 12-20.
36. Swartz, E.E., R. Floyd, and M. Cendoma, Cervical spine functional anatomy and the biomechanics of injury due to compressive loading. *Journal of athletic training*, 2005. 40(3): p. 155.
37. Ashton-miller, J.A. and A.B. Schultz, *Biomechanics of the human spine and trunk*. Exercise and sport sciences reviews, 1988. 16(1): p. 169-204.
38. Nachemson, A., Lumbar intradiscal pressure: experimental studies on post-mortem material. *Acta Orthopaedica Scandinavica*, 1960. 31(sup43): p. 1-104.
39. Frobin, W., et al., Precision measurement of disc height, vertebral height and sagittal plane displacement from lateral radiographic views of the lumbar spine. *Clinical Biomechanics*, 1997. 12: p. S1-S63.
40. Saunders, R., S.L. Kraus, and A. Woerman, *Evaluation, treatment and prevention of musculoskeletal disorders*. Vol. 1. 1993: Saunders Group.
41. Agarwal, A., *Mitigating biomechanical complications of growth rods in juvenile idiopathic scoliosis*. 2015.
42. Vasseur, P., G. Saunders, and C. Steinback, Anatomy and function of the ligaments of the lower cervical spine in the dog. *American journal of veterinary research*, 1981. 42(6): p. 1002-1006.
43. Yahia, L. and S. Garzon, Structure on the capsular ligaments of the facet joints. *Annals of Anatomy-Anatomischer Anzeiger*, 1993. 175(2): p. 185-188.
44. Yoganandan, N., et al., Anatomic study of the morphology of human cervical facet joint. *Spine*, 2003. 28(20): p. 2317-2323.
45. Varlotta, G.P., et al., The lumbar facet joint: a review of current knowledge: part 1: anatomy, biomechanics, and grading. *Skeletal radiology*, 2011. 40(1): p. 13-23.
46. Jaumard, N.V., W.C. Welch, and B.A. Winkelstein, Spinal facet joint biomechanics and mechanotransduction in normal, injury and degenerative conditions. *Journal of biomechanical engineering*, 2011. 133(7): p. 071010.
47. Kalichman, L. and D.J. Hunter. Lumbar facet joint osteoarthritis: a review. in *Seminars in arthritis and rheumatism*. 2007. Elsevier.

48. Adams, M. and W. Hutton, The mechanical function of the lumbar apophyseal joints. *Spine*, 1983. 8(3): p. 327-330.
49. Ahmed, A.M., N.A. Duncan, and D.L. Burke, The effect of facet geometry on the axial torque-rotation response of lumbar motion segments. *Spine*, 1990. 15(5): p. 391-401.
50. Yang, K.H. and A. King, Mechanism of facet load transmission as a hypothesis for low-back pain. *Spine*, 1984. 9(6): p. 557-565.
51. Adams, M. and W. Hutton, The effect of posture on the role of the apophysial joints in resisting intervertebral compressive forces. *Bone & Joint Journal*, 1980. 62(3): p. 358-362.
52. Berry, J.L., et al., A morphometric study of human lumbar and selected thoracic vertebrae. *Spine*, 1987. 12(4): p. 362-367.
53. Pal, G., R. Routal, and S. Saggi, The orientation of the articular facets of the zygapophyseal joints at the cervical and upper thoracic region. *Journal of anatomy*, 2001. 198(4): p. 431-441.
54. Pal, G. and R. Routal, Mechanism of change in the orientation of the articular process of the zygapophyseal joint at the thoracolumbar junction. *Journal of anatomy*, 1999. 195(2): p. 199-209.
55. Panjabi, M.M., et al., Mechanical properties of the human cervical spine as shown by three-dimensional load-displacement curves. *Spine*, 2001. 26(24): p. 2692-2700.
56. Kozanek, M., et al., Range of motion and orientation of the lumbar facet joints in vivo. *Spine*, 2009. 34(19): p. E689-E696.
57. Ahn, H.S. and D.J. DiAngelo, Biomechanical testing simulation of a cadaver spine specimen: development and evaluation study. *Spine*, 2007. 32(11): p. E330-E336.
58. Abumi, K., et al., Biomechanical evaluation of lumbar spinal stability after graded facetectomies. *Spine*, 1990. 15(11): p. 1142-1147.
59. Tender, G.C., et al., Unilateral progressive alterations in the lumbar spine: a biomechanical study. *Journal of Neurosurgery: Spine*, 2005. 2(3): p. 298-302.
60. Nolte, L.P., M. Panjabi, and T. Oxland, Biomechanical properties of lumbar spinal ligaments. *Clinical implant materials, advances in biomaterials*, 1990. 9: p. 663-668.

61. Panjabi, M., L. Jorneus, and G. Greenstein, Physical properties of lumbar spine ligaments. *Trans Orthop Res Soc*, 1984. 9: p. 112.
62. Neumann, P., et al., Mechanical properties of the human lumbar anterior longitudinal ligament. *Journal of biomechanics*, 1992. 25(10): p. 1185-1194.
63. Gould, J.A., *Orthopaedic and sports physical therapy*. 1990: CV Mosby.
64. Pintar, F.A., et al., Biomechanical properties of human lumbar spine ligaments. *Journal of biomechanics*, 1992. 25(11): p. 1351-1356.
65. Forell, V. and G. Allen, *Biomechanical Implications of Lumbar Spinal Ligament Transection A Finite Element Study*. 2012.
66. Heuer, F., et al., Stepwise reduction of functional spinal structures increase range of motion and change lordosis angle. *Journal of biomechanics*, 2007. 40(2): p. 271-280.
67. Bogduk, N., *Clinical anatomy of the lumbar spine and sacrum*. 2005: Elsevier Health Sciences.
68. Moore, K.L., A.F. Dalley, and A.M. Agur, *Clinically oriented anatomy*. 2013: Lippincott Williams & Wilkins.
69. Yahia, L.-h., et al., Ultrastructure of the Human Interspinous Ligament and Ligamentum Flavum A Preliminary Study. *Spine*, 1990. 15(4): p. 262-268.
70. Dickman, C.A., D.J. Rosenthal, and N.I. Perin, *Thoracoscopic spine surgery*. 1999: Thieme.
71. Bannister, L.H., *Gray's anatomy*. 1999: Churchill Livingstone.
72. Heylings, D., Supraspinous and interspinous ligaments of the human lumbar spine. *Journal of anatomy*, 1978. 125(Pt 1): p. 127.
73. Gudavalli, M.R. and J.J. Triano, An analytical model of lumbar motion segment in flexion. *Journal of manipulative and physiological therapeutics*, 1999. 22(4): p. 201-208.
74. Hindle, R., M. Percy, and A. Cross, Mechanical function of the human lumbar interspinous and supraspinous ligaments. *Journal of biomedical engineering*, 1990. 12(4): p. 340-344.

75. Zander, T., A. Rohlmann, and G. Bergmann, Influence of ligament stiffness on the mechanical behavior of a functional spinal unit. *Journal of biomechanics*, 2004. 37(7): p. 1107-1111.
76. Butt, A.M., et al., A comprehensive review of the sub-axial ligaments of the vertebral column: part I anatomy and function. *Child's Nervous System*, 2015. 31(7): p. 1037-1059.
77. Adams, M., W. Hutton, and J. Stott, The resistance to flexion of the lumbar intervertebral joint. *Spine*, 1980. 5(3): p. 245-253.
78. Vergroesen, P.-P., et al., Mechanics and biology in intervertebral disc degeneration: a vicious circle. *Osteoarthritis and Cartilage*, 2015. 23(7): p. 1057-1070.
79. Jongeneelen, C., F. Baaijens, and J. Huyghe, Biomechanics in the intervertebral disc A literature review. *BMTE*, 2006. 618: p. 24.
80. Shapiro, I.M. and M.V. Risbud, *The intervertebral disc : molecular and structural studies of the disc in health and disease*. 2013, Wien: Springer.
81. Adams, M.A. and P.J. Roughley, What is intervertebral disc degeneration, and what causes it? *Spine*, 2006. 31(18): p. 2151-2161.
82. Naidich, T.P., M. Castillo, and S. Cha, *Imaging of the spine*. 2011: Elsevier Health Sciences.
83. Perey, O., Fracture of the vertebral end-plate in the lumbar spine: an experimental biomechanical investigation. *Acta Orthopaedica Scandinavica*, 1957. 28(sup25): p. 1-101.
84. Broberg, K.B., On the mechanical behaviour of intervertebral discs. *Spine*, 1983. 8(2): p. 151-165.
85. Goel, V. and Y. Kim, Effects of injury on the spinal motion segment mechanics in the axial compression mode. *Clinical Biomechanics*, 1989. 4(3): p. 161-167.
86. Inoue, H. and T. Takeda, Three-dimensional observation of collagen framework of lumbar intervertebral discs. *Acta Orthopaedica Scandinavica*, 1975. 46(6): p. 949-956.
87. Cassidy, J., A. Hiltner, and E. Baer, Hierarchical structure of the intervertebral disc. *Connective tissue research*, 1989. 23(1): p. 75-88.

88. D STEPHEN, H. and D.W. Hukins, Relation between the structure of the annulus fibrosus and the function and failure of the intervertebral disc. *Spine*, 1980. 5(2): p. 106-116.
89. Vernon-Roberts, B., The pathology and interrelation of intervertebral disc lesions, osteoarthritis of the apophyseal joints, lumbar spondylosis and low back pain. *The lumbar spine and back pain*. 2nd ed. Tunbridge Wells etc: Pitman Medical, 1980, 1980: p. 83-1.
90. Souter, W.A. and T.K. Taylor, Sulphated acid mucopolysaccharide metabolism in the rabbit intervertebral disc. *Bone & Joint Journal*, 1970. 52(2): p. 371-384.
91. van der Linden, E., L.J. Kroft, and P.S. Dijkstra, Treatment of vertebral tumor with posterior wall defect using image-guided radiofrequency ablation combined with vertebroplasty: preliminary results in 12 patients. *Journal of Vascular and Interventional Radiology*, 2007. 18(6): p. 741-747.
92. Schulte, K., C.R. Clark, and V.K. Goel, Kinematics of the cervical spine following discectomy and stabilization. *Spine*, 1989. 14(10): p. 1116-1121.
93. Marcia, S. and L. Saba, *Radiofrequency Treatments on the Spine*. 2017, Springer.
94. Setton, L.A., Anisotropic and inhomogeneous tensile behavior of the human annulus fibrosus: experimental measurement and material model predictions. *Journal of biomechanical engineering*, 2001. 123(3): p. 256-263.
95. Holzapfel, G.A., et al., Single lamellar mechanics of the human lumbar annulus fibrosus. *Biomechanics and modeling in mechanobiology*, 2005. 3(3): p. 125-140.
96. Shan, Z., et al., Correlation between biomechanical properties of the annulus fibrosus and magnetic resonance imaging (MRI) findings. *European Spine Journal*, 2015. 24(9): p. 1909-1916.
97. Skaggs, D., et al., Regional variation in tensile properties and biochemical composition of the human lumbar annulus fibrosus. *Spine*, 1994. 19(12): p. 1310-1319.
98. Ebara, S., et al., Tensile properties of nondegenerate human lumbar annulus fibrosus. *Spine*, 1996. 21(4): p. 452-461.
99. Iatridis, J.C., et al., Is the nucleus pulposus a solid or a fluid? Mechanical behaviors of the nucleus pulposus of the human intervertebral disc. *Spine*, 1996. 21(10): p. 1174-1184.

100. Pooni, J., et al., Comparison of the structure of human intervertebral discs in the cervical, thoracic and lumbar regions of the spine. *Surgical and radiologic anatomy*, 1986. 8(3): p. 175-182.
101. Antoniou, J., et al., The human lumbar intervertebral disc: evidence for changes in the biosynthesis and denaturation of the extracellular matrix with growth, maturation, ageing, and degeneration. *Journal of Clinical Investigation*, 1996. 98(4): p. 996.
102. Dickson, I., et al., Variations in the protein components of human intervertebral disk with age. *Nature*, 1967. 215(5096): p. 52-53.
103. Keyes, D.C. and E.L. Compere, The normal and pathological physiology of the nucleus pulposus of the intervertebral disc: an anatomical, clinical, and experimental study. *JBJS*, 1932. 14(4): p. 897-938.
104. McNally, D., M. Adams, and A. Goodship, Development and validation of a new transducer for intradiscal pressure measurement. *Journal of biomedical engineering*, 1992. 14(6): p. 495-498.
105. Newell, N., et al., Biomechanics of the human intervertebral disc: a review of testing techniques and results. *Journal of the mechanical behavior of biomedical materials*, 2017.
106. Koeller, W., et al., Biomechanical properties of human intervertebral discs subjected to axial dynamic compression—influence of age and degeneration. *Journal of Biomechanics*, 1986. 19(10): p. 807-816.
107. Wognum, S., J.M. Huyghe, and F.P. Baaijens, Influence of osmotic pressure changes on the opening of existing cracks in 2 intervertebral disc models. *Spine*, 2006. 31(16): p. 1783-1788.
108. Roberts, S., et al., Does the thickness of the vertebral subchondral bone reflect the composition of the intervertebral disc? *European Spine Journal*, 1997. 6(6): p. 385-389.
109. Moon, S.M., et al., Evaluation of intervertebral disc cartilaginous endplate structure using magnetic resonance imaging. *European Spine Journal*, 2013. 22(8): p. 1820-1828.
110. Kalb, S., et al., Genetics of the degenerated intervertebral disc. *World neurosurgery*, 2012. 77(3): p. 491-501.

111. Benneker, L.M., et al., Correlation of radiographic and MRI parameters to morphological and biochemical assessment of intervertebral disc degeneration. *European Spine Journal*, 2005. 14(1): p. 27-35.
112. Urban, J. and J. McMullin, Swelling pressure of the lumbar intervertebral discs: influence of age, spinal level, composition, and degeneration. *Spine*, 1988. 13(2): p. 179-187.
113. Frobin, W., et al., Height of lumbar discs measured from radiographs compared with degeneration and height classified from MR images. *European radiology*, 2001. 11(2): p. 263-269.
114. Inoue, N. and A.A.E. Orías, Biomechanics of intervertebral disk degeneration. *Orthopedic Clinics of North America*, 2011. 42(4): p. 487-499.
115. Adams, M., D. McNally, and P. Dolan, Stress Distributions Inside Intervertebral Discs. *The Journal of Bone and Joint Surgery-british Volume*, 1997. 79(3S): p. 283.
116. Nachemson, A., The effect of forward leaning on lumbar intradiscal pressure. *Acta Orthopaedica Scandinavica*, 1965. 35(1-4): p. 314-328.
117. Wilke, H.-J., et al., Validity and interobserver agreement of a new radiographic grading system for intervertebral disc degeneration: Part I. Lumbar spine. *European Spine Journal*, 2006. 15(6): p. 720-730.
118. Mimura, M., et al., Disc degeneration affects the multidirectional flexibility of the lumbar spine. *Spine*, 1994. 19(12): p. 1371-1380.
119. Kettler, A. and H.-J. Wilke, Review of existing grading systems for cervical or lumbar disc and facet joint degeneration. *European Spine Journal*, 2006. 15(6): p. 705-718.
120. Kettler, A., et al., Do early stages of lumbar intervertebral disc degeneration really cause instability? Evaluation of an in vitro database. *European Spine Journal*, 2011. 20(4): p. 578-584.
121. Fujiwara, A., et al., The relationship between disc degeneration, facet joint osteoarthritis, and stability of the degenerative lumbar spine. *Clinical Spine Surgery*, 2000. 13(5): p. 444-450.
122. Tanaka, N., et al., The relationship between disc degeneration and flexibility of the lumbar spine. *The spine journal*, 2001. 1(1): p. 47-56.

123. Krismer, M., et al., Motion in lumbar functional spine units during side bending and axial rotation moments depending on the degree of degeneration. *Spine*, 2000. 25(16): p. 2020-2027.
124. Rohlmann, A., et al., Analysis of the influence of disc degeneration on the mechanical behaviour of a lumbar motion segment using the finite element method. *Journal of biomechanics*, 2006. 39(13): p. 2484-2490.
125. Schmidt, H., et al., The risk of disc prolapses with complex loading in different degrees of disc degeneration—a finite element analysis. *Clinical Biomechanics*, 2007. 22(9): p. 988-998.
126. Park, W.M., Y.H. Kim, and S. Lee, Effect of intervertebral disc degeneration on biomechanical behaviors of a lumbar motion segment under physiological loading conditions. *Journal of Mechanical Science and Technology*, 2013. 27(2): p. 483.
127. Savage, J.W. and A.A. Patel, Fixed sagittal plane imbalance. *Global spine journal*, 2014. 4(04): p. 287-296.
128. Halim, A., D. Kiester, and Y.-P. Lee. Smith-Petersen and pedicle subtraction osteotomies. in *Seminars in Spine Surgery*. 2017. Elsevier.
129. Schwab, F., et al., Adult spinal deformity—postoperative standing imbalance: how much can you tolerate? An overview of key parameters in assessing alignment and planning corrective surgery. *Spine*, 2010. 35(25): p. 2224-2231.
130. Schwab, F., et al., Gravity line analysis in adult volunteers: age-related correlation with spinal parameters, pelvic parameters, and foot position. *Spine*, 2006. 31(25): p. E959-E967.
131. Van Royen, B., et al., Accuracy of the sagittal vertical axis in a standing lateral radiograph as a measurement of balance in spinal deformities. *European Spine Journal*, 1998. 7(5): p. 408-412.
132. Van Royen, B., A. De Gast, and T. Smit, Deformity planning for sagittal plane corrective osteotomies of the spine in ankylosing spondylitis. *European Spine Journal*, 2000. 9(6): p. 492-498.
133. Mehta, V.A., et al., Implications of spinopelvic alignment for the spine surgeon. *Neurosurgery*, 2011. 76(suppl\_1): p. S42-S56.
134. Roussouly, P. and C. Nnadi, Sagittal plane deformity: an overview of interpretation and management. *European spine journal*, 2010. 19(11): p. 1824-1836.

135. Lafage, V., et al., Pelvic tilt and truncal inclination: two key radiographic parameters in the setting of adults with spinal deformity. *Spine*, 2009. 34(17): p. E599-E606.
136. Bridwell, K.H., L.G. Lenke, and S.J. Lewis, Treatment of spinal stenosis and fixed sagittal imbalance. *Clinical orthopaedics and related research*, 2001. 384: p. 35-44.
137. Silva, F.E. and L.G. Lenke, Adult degenerative scoliosis: evaluation and management. *Neurosurgical focus*, 2010. 28(3): p. E1.
138. Bridwell, K.H., Decision making regarding Smith-Petersen vs. pedicle subtraction osteotomy vs. vertebral column resection for spinal deformity. *Spine*, 2006. 31(19S): p. S171-S178.
139. Smith-Petersen, M., C.B. Larson, and O.E. Aufranc, Osteotomy of the spine for correction of flexion deformity in rheumatoid arthritis. *JBJS*, 1945. 27(1): p. 1-11.
140. Dorward, I.G. and L.G. Lenke, Osteotomies in the posterior-only treatment of complex adult spinal deformity: a comparative review. *Neurosurgical focus*, 2010. 28(3): p. E4.
141. La Marca, F. and H. Brumblay, Smith–Petersen Osteotomy in Thoracolumbar Deformity Surgery. *Neurosurgery*, 2008. 63(3): p. A163-A170.
142. Singh, M.K., et al., Pedicle Subtraction Osteotomy, in *Spinal Osteotomy*. 2015, Springer. p. 89-109.
143. Sansur, C.A., et al., Surgical management of global sagittal deformity in ankylosing spondylitis. 2008.
144. Cho, K.-J., et al., Comparison of Smith-Petersen versus pedicle subtraction osteotomy for the correction of fixed sagittal imbalance. *Spine*, 2005. 30(18): p. 2030-2037.
145. Kim, Y.J., et al., Results of lumbar pedicle subtraction osteotomies for fixed sagittal imbalance: a minimum 5-year follow-up study. *Spine*, 2007. 32(20): p. 2189-2197.
146. Gupta, M.C., et al., Spinal osteotomies for rigid deformities. *Neurosurgery Clinics of North America*, 2013. 24(2): p. 203-211.
147. Bridwell, K.H., et al., Pedicle subtraction osteotomy for the treatment of fixed sagittal imbalance. *J Bone Joint Surg Am*, 2004(suppl 1): p. 44-49.
148. Mummaneni, P.V., et al., Pedicle subtraction osteotomy. *Neurosurgery*, 2008. 63(suppl\_3): p. A171-A176.

149. Roussouly, P., et al., Classification of the normal variation in the sagittal alignment of the human lumbar spine and pelvis in the standing position. *Spine*, 2005. 30(3): p. 346-353.
150. Roussouly, P. and J.L. Pinheiro-Franco, Biomechanical analysis of the spino-pelvic organization and adaptation in pathology. *European Spine Journal*, 2011. 20(5): p. 609.
151. Cogniet, A., et al., Clinical and radiological outcomes of lumbar posterior subtraction osteotomies are correlated to pelvic incidence and FBI index. *European Spine Journal*, 2016. 25(8): p. 2657-2667.
152. Salvi, G., et al., Biomechanical analysis of Ponte and pedicle subtraction osteotomies for the surgical correction of kyphotic deformities. *European Spine Journal*, 2016. 25(8): p. 2452-2460.
153. Enercan, M., et al., Osteotomies/spinal column resections in adult deformity. *European Spine Journal*, 2013. 22(2): p. 254-264.
154. Domanic, U., et al., Surgical correction of kyphosis Posterior total wedge resection osteotomy in 32 patients. *Acta orthopaedica Scandinavica*, 2004. 75(4): p. 449-455.
155. Ozturk, C., et al., Short-term X-ray results of posterior vertebral column resection in severe congenital kyphosis, scoliosis, and kyphoscoliosis. *Spine*, 2012. 37(12): p. 1054-1057.
156. Suk, S.-I., et al., Posterior vertebral column resection for severe spinal deformities. *Spine*, 2002. 27(21): p. 2374-2382.
157. Suk, S.-I., et al., Posterior vertebral column resection in fixed lumbosacral deformity. *Spine*, 2005. 30(23): p. E703-E710.
158. Suk, S.-I., et al., Posterior vertebral column resection for severe rigid scoliosis. *Spine*, 2005. 30(14): p. 1682-1687.
159. Park, P., et al., Comparison of two minimally invasive surgery strategies to treat adult spinal deformity. *Journal of Neurosurgery: Spine*, 2015. 22(4): p. 374-380.
160. Wang, M.Y. and G. Bordon, Mini-open pedicle subtraction osteotomy as a treatment for severe adult spinal deformities: case series with initial clinical and radiographic outcomes. *Journal of Neurosurgery: Spine*, 2016. 24(5): p. 769-776.
161. Smith, J.S., et al., Prospective multicenter assessment of perioperative and minimum 2-year postoperative complication rates associated with adult spinal deformity surgery. *Journal of Neurosurgery: Spine*, 2016. 25(1): p. 1-14.

162. Kim, K.-T., et al., Outcome of pedicle subtraction osteotomies for fixed sagittal imbalance of multiple etiologies: a retrospective review of 140 patients. *Spine*, 2012. 37(19): p. 1667-1675.
163. Upadhyaya, C.D., S. Berven, and P.V. Mummaneni, Spondylolisthesis following a pedicle subtraction osteotomy: Case report. *Neurosurgical focus*, 2010. 28(3): p. E16.
164. Yang, B.P., et al., Clinical and radiographic outcomes of thoracic and lumbar pedicle subtraction osteotomy for fixed sagittal imbalance. *Journal of Neurosurgery: Spine*, 2006. 5(1): p. 9-17.
165. Han, S., et al., Rod stiffness as a risk factor of proximal junctional kyphosis after adult spinal deformity surgery: comparative study between cobalt chrome multiple-rod constructs and titanium alloy two-rod constructs. *The Spine Journal*, 2017.
166. Tang, J.A., et al., Effect of Severity of Rod Contour on Posterior Rod Failure in the Setting of Lumbar Pedicle Subtraction Osteotomy (PSO) A Biomechanical Study. *Neurosurgery*, 2012. 72(2): p. 276-283.
167. Hallager, D.W., et al., Use of supplemental short pre-contoured accessory rods and cobalt chrome alloy posterior rods reduces primary rod strain and range of motion across the pedicle subtraction osteotomy level: an in vitro biomechanical study. *Spine*, 2016. 41(7): p. E388-E395.
168. Shirazi-Adl, A., A.M. Ahmed, and S.C. Shrivastava, Mechanical response of a lumbar motion segment in axial torque alone and combined with compression. *Spine*, 1986. 11(9): p. 914-927.
169. Goffin, J.M., P. Pankaj, and A.H. Simpson, A computational study on the effect of fracture intrusion distance in three-and four-part trochanteric fractures treated with Gamma nail and sliding hip screw. *Journal of Orthopaedic Research*, 2014. 32(1): p. 39-45.
170. Kiapour, A., Investigation into lumbar spine biomechanics of 360 motion preservation systems. 2010: The University of Toledo.
171. Frankel, B., et al., Percutaneous modular head-to-head cross connector. 2015, Google Patents.
172. Patwardhan, A.G., et al., Effect of compressive follower preload on the flexion–extension response of the human lumbar spine. *Journal of Orthopaedic Research*, 2003. 21(3): p. 540-546.

173. Cho, S.K., et al., Major complications in revision adult deformity surgery: risk factors and clinical outcomes with 2-to 7-year follow-up. *Spine*, 2012. 37(6): p. 489-500.
174. Scheer, J.K., et al., Biomechanical analysis of revision strategies for rod fracture in pedicle subtraction osteotomy. *Neurosurgery*, 2011. 69(1): p. 164-172.
175. Burr, D., A.G. Robling, and C.H. Turner, Effects of biomechanical stress on bones in animals. *Bone*, 2002. 30(5): p. 781-786.
176. Gardner, T.N., et al., Dynamic interfragmentary motion in fractures during routine patient activity. *Clinical orthopaedics and related research*, 1997. 336: p. 216-225.
177. Jagodzinski, M. and C. Krettek, Effect of mechanical stability on fracture healing—an update. *Injury*, 2007. 38(1): p. S3-S10.
178. Khan, S.N., M.P. Bostrom, and J.M. Lane, Bone growth factors. *Orthopedic Clinics*, 2000. 31(3): p. 375-387.
179. Skerry, T.M., et al., Early strain-related changes in enzyme activity in osteocytes following bone loading in vivo. *Journal of Bone and Mineral Research*, 1989. 4(5): p. 783-788.
180. Wolff, I., J.(1892) *Das Gesetz der Transformation der Knochen*. Hirschwald: Stuttgart: Schattauer, Berlin.
181. Figueiredo, U., P. Watkins, and A. Goodship, The effects of micromotion in distraction osteogenesis. *Trans Orthop Res Soc*, 1993. 39: p. 130.
182. Klein-Nulend, J., et al., Sensitivity of osteocytes to biomechanical stress in vitro. *The FASEB Journal*, 1995. 9(5): p. 441-445.
183. Lynn, G., et al., Mechanical stability of thoracolumbar pedicle screw fixation: the effect of crosslinks. *Spine*, 1997. 22(14): p. 1568-1572.
184. Kuklo, T.R., et al., Biomechanical contribution of transverse connectors to segmental stability following long segment instrumentation with thoracic pedicle screws. *Spine*, 2008. 33(15): p. E482-E487.
185. Lim, T.-H., et al., Biomechanics of transfixation in pedicle screw instrumentation. *Spine*, 1996. 21(19): p. 2224-2229.
186. Yamaguchi, K.T., et al., Are rib versus spine anchors protective against breakage of growing rods? *Spine deformity*, 2014. 2(6): p. 489-492.

## 8 Appendix

This appendix includes the FEA results for the PSO construct instrumented with interbody spacers integrated with bone grafting above and below the PSO level. The bone grafts were assigned iliac cancellous bone material properties ( $E=70$ ,  $\nu=0.2$ ) and were bonded to the interbody spacers and intervertebral disc endplates using tie constraints.

The results of the instrumented T10-S1 global ROM for different loading directions before and after adding interbody spacers plus bone grafts were shown in Figure .

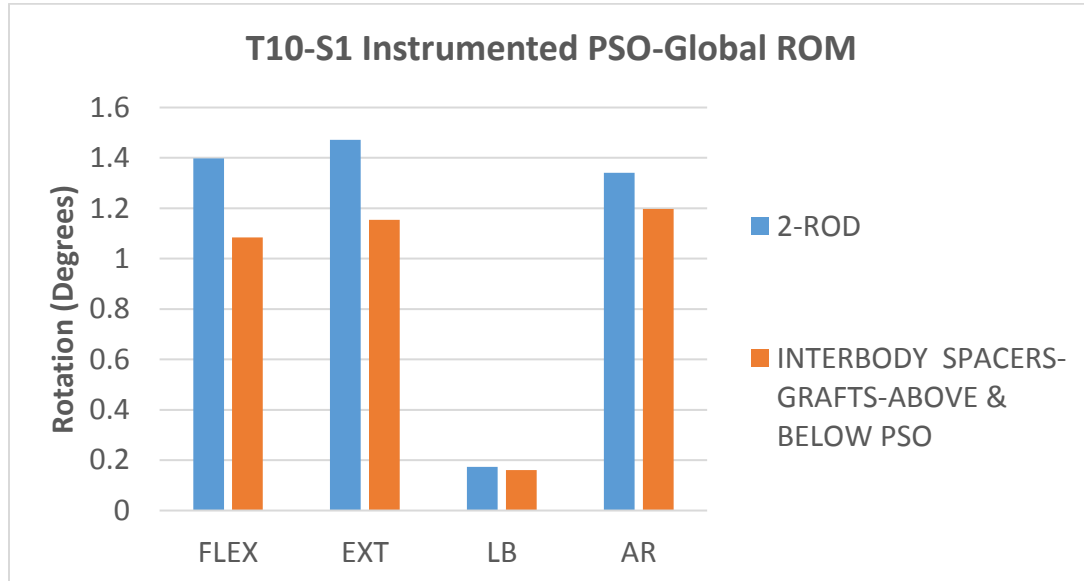


Figure A-1 Comparison of the instrumented T10-S1 global ROM for different loading cases before and after adding interbody spacers plus bone grafts at above and below the PSO level.

Table A.1 shows the values and locations of the maximum von Mises stress on the rods in different loading directions after adding the interbody spacers and bone grafts at the PSO adjacent levels.

In addition, by adding interbody spacers plus bone grafts to the 2-rod construct adjacent to the PSO level, the magnitude of the force acting on the fractured surface was 336.4N.

Table A.1 Maximum von Mises stress values and locations recorded on the rods in different motions after adding interbody spacers and bone grafts at the adjacent levels to the PSO.

| <b>INTERBODY SPACERS-GRAFTS ABOVE &amp; BELOW PSO</b> |                    |          |
|---|--------------------|----------|
|   | Stress Value (MPa) | location |
| <b>FLEX</b>   | 229                | L4-L5    |
| <b>EXT</b>  | 102                | L4-L5    |
| <b>LB</b>   | 202                | L4-L5    |
| <b>AR</b>   | 229                | L4-L5    |